

Universität  
Rostock



Tradio et Innovatio

LEIBNIZ INSTITUTE  
OF  
ATMOSPHERIC  
PHYSICS



Doctoral Thesis in agreement with

Universität Rostock

Mathematisch-Naturwissenschaftliche Fakultät  
Institute: Leibniz-Institut für Atmosphärenphysik

---

## Long-term trends and solar cycle response of Noctilucent Clouds

---

a cumulative dissertation by

Ashique VELLALASSERY

June 2024

*Supervisor:*

Prof. Dr. Franz-Josef Lübken



Dieses Werk ist lizenziert unter einer  
Creative Commons Namensnennung 4.0 International Lizenz.

ii

## **Gutachter:**

- Prof. Dr. Franz Josef Lübken  
Leibniz Institute of Atmospheric Physics at the University of Rostock,  
Kühlungsborn, Germany
- Prof. Dr. Jörg Gumbel  
Meteorologiska institutionen (MISU), Department of Meteorology, Stockholm  
University, Sweden

**Jahr der Einreichung:** 2024

**Jahr der Verteidigung:** 2024

# Abstract

Noctilucent clouds (NLCs) consist of ice particles and are the highest clouds in the Earth's atmosphere, occurring at 80-85 km above the Earth's surface in the extremely cold ( $\sim 130\text{K}$ ) summer mesopause region at mid and high latitudes. The formation of NLCs requires extremely cold background temperatures and the presence of water vapour ( $\text{H}_2\text{O}$ ). Due to their high sensitivity to temperature and water vapour concentration, NLCs have been proposed as important tracers for background atmospheric conditions in the summer mesopause region. The 11-year solar cycle significantly influences temperature and water vapor in the upper mesosphere. Since water vapor and temperature play a major role in determining the chemistry and dynamics of the mesosphere, a detailed understanding of the underlying mechanisms is essential for studying solar-induced changes and assessing long-term climate trends in the upper mesosphere. In this thesis, the influence and effects of the 11-year solar cycle on NLCs, background water vapor, and temperatures are investigated using an atmospheric background model Leibniz Institute for the Middle Atmosphere (LIMA) and a microphysical model Mesospheric Ice Microphysics And tranSport (MIMAS). One of the main findings is that, in the presence of NLCs, the solar cycle response of water vapor strongly depends on altitude. It is found that  $\text{H}_2\text{O}$  concentration correlates positively with temperature changes due to the solar cycle at altitudes above about 83 km, where NLCs form. The photolysis effect leads to an anti-correlation of  $\text{H}_2\text{O}$  concentration and solar Lyman-alpha ( $\text{Ly}\alpha$ ) radiation, which gets even more pronounced at altitudes below 83 km where NLC ice particles sublimate. The effects of increasing greenhouse gases on the long-term trends in the response of noctilucent clouds (NLCs) and the background atmosphere to the 11-year solar cycle, which spans 170 years (from 1849 to 2019) and covers 15 solar cycles, are investigated. The results show that the background temperature and  $\text{H}_2\text{O}$  exhibit an apparent response to the solar cycle that increases after 1960 due to increased greenhouse gas concentrations. The solar cycle impact on NLC properties, including maximum brightness ( $\beta_{\text{max}}$ ) and ice water content (IWC), increases with time, primarily due to the increased water vapor content resulting from the increased methane concentration. The continuing increase in methane emissions is expected to significantly enhance the brightness of NLCs and their ice water content in the future. Our study investigates the absorption of solar radiation by future enhancements in NLCs by performing model simulations for the period from 1950 to 2100 with increasing methane concentration according to future climate scenarios. The results illustrate that, at  $69 \pm 3^\circ\text{N}$ , UV absorption by NLCs at  $\lambda = 126 \text{ nm}$  is predicted to increase from  $\sim 3\%$  to  $\sim 7\%$  by 2100. Absorption of the visible spectrum (532 nm) is expected to increase from 0.0030% in 1950 to 0.020% in 2100, with local values of up to 0.35%. It is estimated that future average absorptions in some regions will be of the same order of magnitude as the variations caused by the solar cycle. Similar trends are observed at  $79 \pm 3^\circ\text{N}$ , while they are lower at  $58 \pm 3^\circ\text{N}$ . The ice mass in the NLCs is expected to increase from 677 to 1871 tonnes between 1950 and 2100.



# Zusammenfassung

Leuchtende nachtwolken (Noctilucent Clouds, NLCs) bestehen aus Eispartikeln und sind die höchsten Wolken in der Erdatmosphäre. Sie entstehen in 80-85 km Höhe über der Erdoberfläche in der extrem kalten Sommermesopausenregion in mittleren und hohen Breiten. Die Bildung von NLCs erfordert extrem kalte Hintergrundtemperaturen ( $\sim 130\text{K}$ ) und das Vorhandensein von Wasserdampf ( $\text{H}_2\text{O}$ ). Aufgrund ihrer hohen Empfindlichkeit gegenüber Temperatur und Wasserdampfkonzentration wurden NLCs als wichtige Tracer in der Sommermesopausenregion vorgeschlagen. Der 11-jährige Sonnenzyklus beeinflusst Temperatur und Wasserdampf in der oberen Mesosphäre erheblich. Da Wasserdampf und Temperatur eine wichtige Rolle bei der Bestimmung der Chemie und Dynamik der Mesosphäre spielen, ist ein detailliertes Verständnis der zugrundeliegenden Mechanismen von wesentlicher Bedeutung für die Untersuchung solarer Veränderungen und die Bewertung langfristiger Klimatrends in der oberen Mesosphäre. In dieser Arbeit werden der Einfluss und die Auswirkungen des 11-jährigen Sonnenzyklus auf NLCs und Hintergrundwasserdampf und -temperaturen mit Hilfe eines atmosphärischen Hintergrundmodells (Leibniz-Institut für Mittlere Atmosphäre (LIMA)) und eines mikrophysikalischen Modells (Mesospheric Ice Microphysics And transport (MIMAS)) untersucht. Eine der wichtigsten Erkenntnisse ist, dass die Reaktion des Wasserdampfes auf den Sonnenzyklus während der NLCs stark von der Höhe abhängt. Es zeigt sich, dass die  $\text{H}_2\text{O}$ -Konzentration in Höhen oberhalb von etwa 82 km, wo sich NLCs bilden, positiv mit den Temperaturänderungen aufgrund des Sonnenzyklus korreliert. Der Photolyse-Effekt führt zu einer Anti-Korrelation zwischen der  $\text{H}_2\text{O}$ -Konzentration und der solaren Lyman-Alpha-Strahlung ( $\text{Ly}\alpha$ ), die in Höhen unter 83 km, wo NLC-Eispartikel sublimieren, noch ausgeprägter ist. Wir haben auch die Auswirkungen zunehmender Treibhausgase auf die langfristigen Trends in der Reaktion der NLCs und der Hintergrundatmosphäre auf den 11-jährigen Sonnenzyklus untersucht, der sich über 170 Jahre (1849 bis 2019) erstreckt und somit 15 Sonnenzyklen abdeckt. Die Ergebnisse zeigen, dass die Hintergrundtemperatur und  $\text{H}_2\text{O}$  während des gesamten Untersuchungszeitraums eine offensichtliche Reaktion auf den Sonnenzyklus zeigen, die sich nach 1960 aufgrund der erhöhten Treibhausgasemissionen verstärkt. Die Auswirkungen des Sonnenzyklus auf die NLC-Eigenschaften, einschließlich der maximalen Helligkeit ( $\beta_{\text{max}}$ ) und des Eiswassergehalts (IWC), nehmen mit der Zeit zu, was in erster Linie auf den erhöhten Wasserdampfgehalt infolge der gestiegenen Methankonzentration zurückzuführen ist. Es wird erwartet, dass der anhaltende Anstieg der Methanemissionen die Helligkeit der NLCs und ihren Eiswassergehalt in Zukunft deutlich erhöhen wird. In dieser Studie wurde die Absorption der Sonnenstrahlung durch zukünftige Verbesserungen in NLCs untersucht, indem Modellsimulationen für den Zeitraum von 1950 bis 2100 mit steigender Methankonzentration gemäß zukünftiger Klimaszenarien (IPCC RCP 8.5) durchgeführt wurden. Die Ergebnisse zeigen, dass bei  $69\pm 3^\circ\text{N}$  die UV-Absorption durch NLCs bei  $\lambda = 126\text{ nm}$  von  $\sim 3\%$  to  $\sim 7\%$

ansteigen wird, was bis 2100 lokal 30% erreichen könnte. Die Absorption des sichtbaren Spektrums (532 nm) wird voraussichtlich von 0,0030% im Jahr 1950 auf 0,020% im Jahr 2100 ansteigen, mit lokalen Werten von bis zu 0,35%. Es wird geschätzt, dass die durchschnittliche Absorption in einigen Regionen in der Größenordnung der Schwankungen des Sonnenzyklus liegen wird. Ähnliche Trends sind bei  $79 \pm 3^\circ\text{N}$  zu beobachten, während sie bei  $58 \pm 3^\circ\text{N}$  geringer sind. Die Eismasse in den NLC wird zwischen 1950 und 2100 voraussichtlich von 677 auf 1871 Tonnen ansteigen.

# Contents

<b>Abstract</b>	<b>iii</b>
<b>Zusammenfassung</b>	<b>v</b>
<b>1 Introduction</b>	<b>1</b>
1.1 The Earth's atmosphere . . . . .	1
1.2 Motivation . . . . .	2
1.3 Objectives and outline of the thesis . . . . .	4
<b>2 Ice particle transport model MIMAS</b>	<b>7</b>
2.1 MIMAS overview and input parameters . . . . .	7
2.1.1 Background atmosphere model LIMA . . . . .	8
2.1.2 Water vapour source and solar activity . . . . .	9
2.2 Microphysical processes . . . . .	9
2.2.1 Dust particles . . . . .	10
2.2.2 Water vapour in the summer MLT region . . . . .	11
2.2.3 Particle nucleation, growth and transport . . . . .	13
2.3 Model output and numerical experiments . . . . .	15
<b>3 Trends in NLCs and background atmosphere</b>	<b>19</b>
3.1 Long-term trends in temperature and water vapour . . . . .	19
3.2 Long-term trends in noctilucent clouds . . . . .	22
3.3 Solar cycle response in noctilucent clouds . . . . .	23
<b>4 Solar cycle response of water vapour and noctilucent clouds</b>	<b>25</b>
<b>5 Long-term trends in noctilucent clouds response to solar cycle variations</b>	<b>31</b>
<b>6 Absorption of solar radiation by noctilucent clouds in a changing climate</b>	<b>37</b>
<b>7 Conclusion and outlook</b>	<b>41</b>
7.1 Thesis summary . . . . .	41
7.2 Directions for future research . . . . .	42
<b>Bibliography</b>	<b>45</b>
<b>A Vellalassery et al., 2023</b>	<b>55</b>
<b>B Vellalassery et al., 2024</b>	<b>69</b>
<b>C Lübken et al., 2024</b>	<b>87</b>
<b>Contribution to the Manuscripts</b>	<b>95</b>

<b>Curriculum Vitæ</b>	<b>97</b>
<b>Acknowledgements</b>	<b>99</b>
<b>Declaration of Authorship</b>	<b>101</b>

# List of Figures

1.1	Thermal structure of the Earth's atmosphere (adapted from Baumgarten (2001)) . . . . .	1
1.2	NLCs seen from the beach of Kühlungsborn on 12 July 2023, 23:37 . . . . .	4
2.1	Sketch of the LIMA (green) and MIMAS (blue) models. Figure taken from Vellalassery et al. (2023), Fig. 1. . . . .	7
2.2	Schematic representation of the formation, growth and sedimentation of NLC and the redistribution of water vapour and dust particles, adapted from Kiliani (2014). . . . .	10
2.3	Schematic representation of meteoric dust in MIMAS, adapted from Kiliani (2014). . . . .	11
2.4	Time series of CO <sub>2</sub> and CH <sub>4</sub> concentrations used in the model runs (1849-2019). Figure taken from Vellalassery et al. (2024), Fig. 1. . . . .	17
2.5	Time series of CH <sub>4</sub> concentrations used in the model runs including future CH <sub>4</sub> projections taken from IPCC AR4 (red). Figure taken from Lübken et al. (2024), Fig. 1. . . . .	17
3.1	Time series of (b) temperature at a fixed geometric height (83 km) as a dotted line and at constant pressure level ( $5.962 \times 10^{-3}$ hPa: mean pressure of NLC maximum brightness height) as a solid line; (c) mixing ratios of gas phase water vapour at $p_{\text{mean}}$ (assuming that ice formation had not occurred) for Runs A and B. Note that H <sub>2</sub> O values for Runs A and C are identical. In panels (b) and (c), linear fits for Run A are shown for the periods before ( $m_1$ ) and after ( $m_2$ ) 1960, respectively. The slopes are listed in the inserted legend. Figure taken from Lübken et al. (2018), Fig. 1. . . . .	21
4.1	Time series of solar Ly $\alpha$ , CO <sub>2</sub> , and CH <sub>4</sub> for 1992–2018. The corresponding Ly $\alpha$ , CO <sub>2</sub> , and CH <sub>4</sub> values for the solar cycle maximum and minimum years used for this study are marked. The CO <sub>2</sub> and CH <sub>4</sub> values for run A are represented by dots, and for run E, they are represented by crosses. The study period is divided into period 1 as early (1992–2005) and period 2 as late (2005–2018). Figure taken from Vellalassery et al. (2023), Fig. 2. . . . .	26
4.2	Time series of anomalies of the mean ice water content (IWC) in July at 68°N from model and satellite data, based on Hervig et al. (2019). The anomalies for each data set are calculated as a deviation from their long-term mean. To reduce the year-to-year variability, the time series of SBUV and HALOE are smoothed using a moving average method with a window size of 3. The modulation of the Ly $\alpha$ solar cycle is shown in the bottom panel. Figure taken from Vellalassery et al. (2023), Fig. 3. . . . .	27

4.3	The H <sub>2</sub> O and temperature profile difference between solar maximum (2002) and minimum (1997) for July mean. The blue and yellow lines represent NLC and non-NLC conditions. CO <sub>2</sub> and CH <sub>4</sub> values are constant in all cases, corresponding to 1997. (a) Run F: only temperature change effects on H <sub>2</sub> O. (b) Run G: only photolysis change effect on H <sub>2</sub> O. (c) Run E: temperature change and photolysis change effects on H <sub>2</sub> O. Figure taken from Vellalassery et al. (2023), Fig. 5. . . . .	28
4.4	Time series of Ly $\alpha$ and H <sub>2</sub> O anomalies as monthly averages for July at 68°N for the altitude range of 80–85 km from MIMAS run A and satellites (HALOE and the composite data from MLS and SOFIE). Satellite observations are according to Hervig et al. (2019). The H <sub>2</sub> O–Ly $\alpha$ correlation is calculated for the early and late periods (see inset). Figure taken from Vellalassery et al. (2023), Fig. 8. . . . .	29
4.5	The H <sub>2</sub> O response to the absolute Ly $\alpha$ variations of the solar cycle in July at 68°N in the years between solar minimum and maximum is shown in geometric heights for both the early period (1997-2002) and the late period (2008-2014). The shaded area represents the altitude range used to calculate an average response to the solar cycle. Panels (a) and (b) show the results of two MIMAS model runs: (a) run E with constant CO <sub>2</sub> and CH <sub>4</sub> , and (b) run A with varying CO <sub>2</sub> and CH <sub>4</sub> . Figure taken from Vellalassery et al. (2023), Fig. 9. . . . .	30
5.1	Time series of water vapour concentration as a function of geometric altitude, zonally (69°N) and monthly (July) averaged for (a) Run A without NLC, (b) Run C without NLC, (c) Run A with NLC, and (d) Run C with NLC. Figure taken from Vellalassery et al. (2024), Fig. 3. . . . .	32
5.2	(a) Time series of NLC altitudes (averaged for July and zonally at 69°N) from 1849 to 2019. The results from three runs (A, B, and C) are shown in the figure (see insert). The lower panel shows the time series of the solar Ly $\alpha$ flux (unit: 10 <sup>11</sup> $\gamma$ cm <sup>-2</sup> s <sup>-2</sup> ) averaged for July. (b) Response of NLC altitude to the unit change in solar Ly $\alpha$ during solar cycles between 1855 to 2019 (For example, solar cycle 10 corresponds to 1855-1867, while solar cycle 24 represents 2008-2019). The three runs, A, B, and C, are shown (see insert), showing linear regression fits. The error bars represent the standard error of the mean for the respective solar cycle years. Figure taken from Vellalassery et al. (2024), Fig. 6. . . . .	34
5.3	NLC properties response to a unit change in solar Ly $\alpha$ at 69°N during solar cycles between 1855 and 2019. Results are shown for three runs: A, B, and C (see insert). Error bars indicate the standard error of the mean during respective solar cycle years. The figures are shown for (a) Maximum brightness, (b) IWC, and (c) NLC occurrence rate, with a threshold value of $\beta_{\text{lim}} = 0.05$ applied. Figure taken from Vellalassery et al. (2024), Fig. 7. . . . .	35
6.1	Extinction coefficients as a function of wavelength for (mono-dispers) particle radii as given in the insert (in nm, various colours). The vertical lines mark wavelengths where we have calculated extinctions by the NLC layer. Figure taken from Lübken et al. (2024), Fig. 2. . . . .	38

- 6.2 The relative occurrence frequency of attenuations at  $69 \pm 3^\circ\text{N}$  from various years (see inlet) for a wavelength of  $\lambda = 200 \text{ nm}$  (dots). The values for  $\lambda = 126 \text{ nm}$  (black, crosses, 2080 only) demonstrate that attenuations are increasing rapidly for decreasing wavelengths. The inlet also lists the mean attenuations ( $\langle \dots \rangle$ ) in %. Figure taken from Lübken et al. (2024), Fig. 3. . . . . 39
- 6.3 For each selected year, the mean extinction coefficients (left axis) and attenuations (right axis) are shown at  $69 \pm 3^\circ\text{N}$ . First, we average the extinction coefficients from all columns (only where NLC are present) at a given time-step. Then, we take the extinction coefficients from all time steps and determine the mean (dots), standard deviation (bars), and maximum and minimum values (dashed lines). Furthermore, the maximum extinction coefficient from all columns (before averaging) is shown (red line, "grand maximum"). Figure taken from Lübken et al. (2024), Fig.4. . . . . 40



# List of Tables

2.1 MIMAS simulations carried out under different background conditions. The horizontal arrow stands for constant values for the respective year, and the vertical arrow stands for varying parameters. The effect of solar Ly $\alpha$ variations on H <sub>2</sub> O is shown for each run in the last column . . . . .	16
---	----



# List of Abbreviations

<b>NLCs</b>	Noctilucent Clouds
<b>PMCs</b>	Polar Mesospheric Clouds
<b>MIMAS</b>	Mesospheric Ice Microphysics And tranSport mode
<b>LIMA</b>	Leibniz Institute Middle Atmosphere model
<b>IAP</b>	Institute of Atmospheric Physics
<b>ALOMAR</b>	Arctic Lidar Observatory for Middle Atmosphere Research
<b>MLT</b>	Mesosphere and Lower Thermosphere
<b>NOAA</b>	National Oceanic and Atmospheric Administration
<b>CIRES</b>	Cooperative Institute for Research in Environmental Sciences
<b>SBUV</b>	Solar Backscatter Ultraviolet
<b>WMO</b>	World Meteorological Organisation
<b>LASP</b>	Laboratory for Atmospheric and Space Physics
<b>LISIRD</b>	LASP Interactive Solar Irradiance Rata Data Centre
<b>IR</b>	Near-Infrared
<b>CARMA</b>	Community Aerosol and Radiation Model for Atmospheres
<b>CN</b>	Condensation Nuclei
<b>UV</b>	UltraViolet
<b>GW</b>	Gravity Wave
<b>LIDAR</b>	Light Detection And Ranging
<b>ppmv</b>	parts per million by volume
<b>SOFIE</b>	Solar Occultation For Ice Experiment
<b>AIM</b>	Aeronomy of Ice in the Mesosphere
<b>NASA</b>	National Aeronautics and Space Administration
<b>UARS</b>	Upper Atmosphere Research Satellite
<b>IWC</b>	Ice Water Content
<b>IPCC</b>	Intergovernmental Panel for Climate Change
<b>AR4</b>	Fourth Assessment Report
<b>AR5</b>	Fifth Assessment Report
<b>RCP</b>	Representative Concentration Pathway
<b>GHG</b>	Greenhouse Gas
<b>SSU</b>	Stratospheric Sounding Units
<b>WACCM</b>	Whole Atmosphere Community Climate Model
<b>HALOE</b>	Halogen Occultation Experiment
<b>CIPS</b>	Cloud Imaging and Particle Size
<b>PMSE</b>	Polar Mesospheric Summer Echo
<b>RMR</b>	Rayleigh-Mie-Raman



## Chapter 1

# Introduction

### 1.1 The Earth's atmosphere

The Earth's atmosphere is a complex and dynamic system of gases that surrounds the planet, playing an important role in regulating temperature and climate. It is composed of many different gases, the most abundant of which are nitrogen (78%) and oxygen (21%), along with other common gases such as argon (0.94%), carbon dioxide (0.04%) and traces of different elements. The atmosphere also contains varying amounts of water vapour (H<sub>2</sub>O) and many small solid or liquid particles known as aerosols. These aerosols can originate from outer space, occur naturally or be caused by humans and play an important role in various atmospheric processes. Ascending from the Earth's surface makes the atmosphere less dense, and air pressure decreases. Although there is no well-defined upper boundary to the atmosphere, the region around 100-120 km above the Earth's surface is generally considered the boundary between the atmosphere and space.

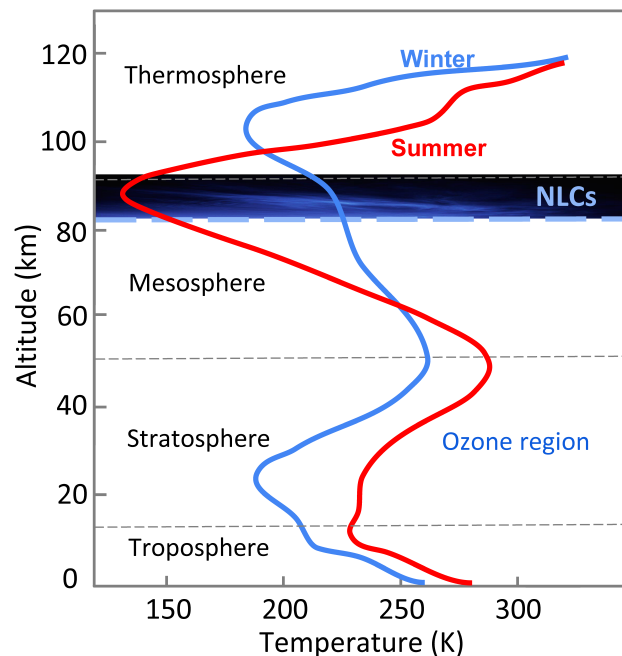


FIGURE 1.1: Thermal structure of the Earth's atmosphere (adapted from Baumgarten (2001))

The atmosphere is divided into distinct layers based on temperature gradient with varying altitude (see Figure 1.1). From the surface upwards, these layers are the troposphere, stratosphere, mesosphere, and thermosphere, separated by so-called "pauses" where the temperature gradients change, as shown in Figure 1.1. These layers influence the Earth's climate and determine weather patterns and environmental conditions. A comprehensive understanding of the individual layers is therefore essential for improving our understanding of the complex workings of our atmosphere.

The troposphere is the lowest layer of the Earth's atmosphere, in which the temperature decreases with altitude and extends up to an average height of 8-16 kilometres. Weather phenomena, such as wind, rain, and storms, occur in this layer. Its upper boundary is known as the tropopause.

Above the troposphere lies the stratosphere, which extends from around 12 to 50 kilometres. The ozone layer is located in the stratosphere between 15 and 30 kilometres above the Earth and protects us from the Sun's harmful ultraviolet (UV) radiation. This layer's most common chemical process is the oxygen-ozone cycle, also known as the Chapman cycle, in which the Sun's UV radiation is converted into heat. Due to the absorption of UV radiation, the temperature increases with altitude and reaches up to 270 K at the stratopause.

As we ascend further, we reach the mesosphere, which extends from 50 to 90 km. In this layer, the temperature decreases with altitude and reaches minimum at its upper boundary, the mesopause. This region is the coldest place on Earth and the layer where meteors burn up as they enter the Earth's atmosphere. In the polar mesosphere, gravity waves (GW) play an essential role in circulation patterns and cause temperatures to be colder in summer than in winter. During summer, temperatures in the polar mesosphere may reach as low as 130 K, allowing the formation of ice particle clouds known as noctilucent clouds (NLCs), which is the main focus of this thesis.

The thermosphere extends from the mesopause to the edge of space (500-1000 km). The ionosphere is the lowest part of the thermosphere, where the electron density peaks at around 250 km. In the thermosphere, temperatures rise dramatically due to the absorption of solar radiation and can reach up to 2000 K during the day.

## 1.2 Motivation

Global greenhouse gas (GHG) emissions have been rising for decades, mainly due to anthropogenic activities such as burning fossil fuels to generate energy, deforestation, and industrial processes. In the current climate debate, the increase of anthropogenic GHGs and their effect on global climate change has been widely investigated for atmospheric layers close to the Earth's surface. The combined air and sea surface temperatures averaged over the globe over 30 years, showing an increase of 0.2 K/decade (Intergovernmental Panel on Climate Change Fourth Assessment Report (IPCC) Fifth Assessment Report (AR5)). However, in the atmosphere above the troposphere, the temperature trend reverses, and an increase in CO<sub>2</sub> leads to the cooling of the middle atmosphere, which is induced by enhanced infrared emission to space (Roble and Dickinson, 1989; Garcia et al., 2007; Berger and Lübken, 2011; Lübken et al., 2013; Marsh et al., 2013). Studies have shown that the global temperature change in the mesosphere is particularly large compared to the layers below.

This has led to the idea that the changes in mesosphere could be an early warning system for climate change (Thomas, 1996).

The mesosphere and lower thermosphere (MLT) region, which acts as an interface between the Earth's atmosphere and space, is characterized by unique dynamics and physical phenomena. MLT is one of the least understood regions of Earth's atmosphere because it is particularly difficult to study this region continuously, as it is too low for satellites and too high for most in situ measurement methods, such as weather balloons. Scientists have nicknamed this region the 'ignorosphere' for these limitations in making observations. The mesosphere is crucial for studying climate-related issues. Understanding its thermal and dynamic structure improves our knowledge of atmospheric processes and coupling mechanisms between the different atmospheric layers.

A notable feature of the MLT region is the different temperature profiles in summer and winter (see Figure 1.1). In summer, this region is generally relatively colder than in winter due to the increased gravity waves (GW) activity. In the summer mesopause region, mean temperatures as low as  $\sim 130$  K are reached (e.g., Lübken, 1999) with local deviations of up to  $\pm 15$  K due to gravity waves (see, for example, Philbrick et al., 1984; Rapp et al., 2002). These extremely low temperatures lead to the formation of ice particle clouds in the polar summer mesosphere, the so-called noctilucent clouds (NLCs), which are the main topic of this thesis.

What are noctilucent clouds?

Noctilucent clouds (NLCs), also known as polar mesospheric clouds (PMCs), form at altitudes of 80-86 km in both polar regions, poleward of  $\sim 55^\circ$ , and only in summer. NLCs are made up of ice particles with a size of 40-80 nm, much smaller than the particles of tropospheric clouds (usually 10  $\mu\text{m}$  and larger). Their formation is strongly dependent on temperature and water vapour availability. NLCs were first observed in northern Europe in 1885, following the remarkable volcanic eruption of Krakatoa between Java and Sumatra two years earlier (Leslie, 1885 ; Backhouse, 1885; Jesse, 1885). NLCs can only be observed during nautical twilight. At the same time, the Sun still illuminates the atmosphere at 80 kilometres and above, but not the ground or the lower atmosphere. Since NLCs are located at very high altitudes (80-86 km), they can reflect the sunlight after an observer has entered the Earth's shadow. During the day, NLCs may be present but are not visible to the naked eye as they are obscured by Rayleigh scattering in the lower atmosphere. The typical appearance of NLCs observed over Kühlungsborn beach is shown in Figure 1.2.

Unlike typical clouds in Earth's troposphere, which contains 75% of the atmospheric mass and 99% of the water vapour, Noctilucent Clouds (NLCs) form in the upper mesosphere. In this region, water vapour exists in extremely low concentrations, namely just a few parts per million by volume (ppmv) (e.g., Seele and Hartogh, 1999). Although the amount of water vapour at this altitude is extremely low, the extremely low temperatures (110–150 K) can lead to supersaturation of the water vapour (Rapp and Thomas, 2006). This creates areas of potential ice formation that do not occur at lower latitudes due to the relatively higher temperatures.



FIGURE 1.2: NLCs seen from the beach of Kühlungsborn on 12 July 2023, 23:37

### Why do we study NLCs?

NLCs have been the subject of scientific interest for many years. As mentioned above, temperature and water vapour measurements in the MLT are difficult to perform. Therefore, indirect indications for the thermal structure and changes are important. Since ice particles are very sensitive to temperature and water vapour, NLC properties such as occurrence rate, brightness, and altitude can be used as indicators for temperature trends and/or water vapour concentrations (Lübken et al., 2009) and are often referred to as ‘The Miner’s Canary of Global Change’ (Thomas, 1996). Consequently, it has been argued that even small long-term changes in the mesospheric water vapour content and/or changes in the mesospheric temperature profile due to anthropogenic emissions of methane (which is a source for mesospheric water vapour) and carbon dioxide (which is the dominant infrared cooling agent in the upper mesosphere) should lead to prominent long-term changes of the observed properties of NLCs, like their occurrence rate and their brightness (Thomas et al., 1989; Rapp and Thomas, 2006).

Therefore, NLCs are utilised as tracers for thermal and dynamic changes in the Earth’s mesopause region, and studying their properties and evolution provides us with insight into the climate changes occurring in the upper atmosphere (Thomas, 2003; Lübken et al., 2018).

### 1.3 Objectives and outline of the thesis

The 11-year solar cycle is one of the factors that influence the mesospheric temperature and water vapour and thus the formation and properties of NLCs (e.g. Thomas, 1996; DeLand et al., 2006; Shettle et al., 2009; Lübken et al., 2009). Investigating the relationship between the solar cycle and the properties of NLCs is one of the keys to studying the effects of the solar cycle on the upper mesosphere. The main objective of this work is to investigate the response of both NLCs and the background atmosphere to variations in the 11-year solar cycle with increasing and constant GHG concentrations. A Lagrangian ice particle transport model called the Mesospheric Ice Microphysics and Transport Model (MIMAS) and atmospheric dynamics model Leibniz Institute Middle Atmosphere (LIMA) are the primary tools

used in this study to understand the relationship between the solar cycle and NLCs in detail. The MIMAS model has the advantage of considering the temporal and spatial variability of the potential ice formation region. Combined with observations, the modelling can contribute to a better understanding of the solar cycle response of NLCs and the mesopause region. The main objectives of this work are following:

- How does the formation of NLCs affect the H<sub>2</sub>O profile and their solar cycle response at mesopause altitudes?
- How does water vapour at NLC altitudes respond to the temperature and photolysis variations caused by the solar cycle?
- What are the long-term trends in the vertical distribution of NLC properties? How do solar cycle modulations influence them?
- Which NLC properties are influenced by the 11-year solar cycle, and how strongly are they influenced?
- What impacts does a long-term increase in greenhouse gases have on the solar cycle response of NLC properties?
- How significant will the absorption of solar radiation by NLCs be in a future climate scenario with increasing CH<sub>4</sub>?

This thesis mainly consists of the results of three publications, which are attached in the appendix. Chapter 2 explains the modelling framework and the different model simulations used in this study. Chapter 3 discusses the long-term trends in NLCs and the background atmosphere based on previous studies. Chapter 4 summarises the study Vellalassery et al. (2023) that examines the underlying mechanism behind the solar cycle response of water vapour under NLC conditions and an increasing greenhouse gas (GHG) scenario. Chapter 5 summarises the study Vellalassery et al. (2024) on the long-term trends in NLCs and their response to the solar cycle using LIMA/MIMAS long-term simulations for 1849-2021. Chapter 6 summarises the recent study Lübken et al. (2024), which investigates the extinction of solar radiation by future NLCs and their significance. The final chapter discusses the conclusions of this work and the outlook for future studies.



## Chapter 2

# Ice particle transport model MIMAS

This chapter introduces the Lagrangian ice particles transport model MIMAS (Mesospheric Ice Microphysics And Transport Model) and gives an overview of its structure. First, the input parameters used in the MIMAS model are described. Then, the microphysical processes incorporated in MIMAS are explained. The primary approach is to calculate the background atmosphere using the Leibniz Institute Middle Atmosphere Model (LIMA). These calculated atmospheric dynamics, temperature, density, and pressure are then input in MIMAS for NLC calculations. This integration makes it possible to analyse the spatial and temporal variability of NLCs (see Figure 3.1).

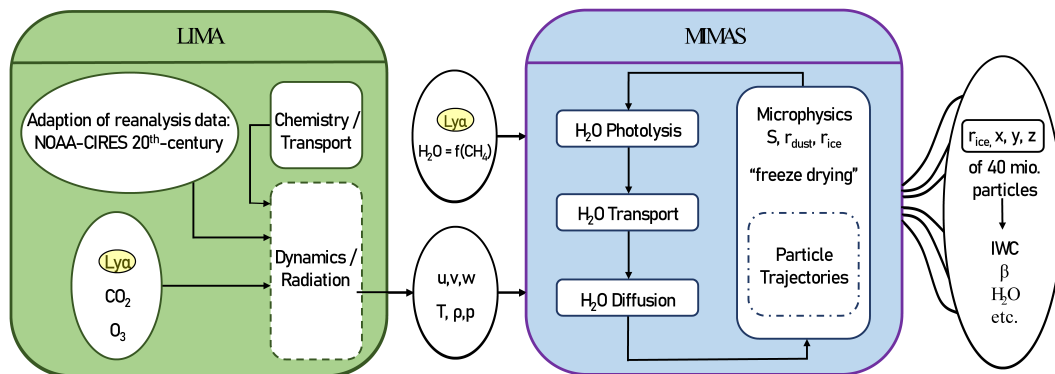


FIGURE 2.1: Sketch of the LIMA (green) and MIMAS (blue) models. Figure taken from Vellalassery et al. (2023), Fig. 1.

### 2.1 MIMAS overview and input parameters

The MIMAS model was developed at the Leibniz Institute of Atmospheric Physics (IAP) specifically to model ice particles in the MLT region (Berger and Lübken, 2015). MIMAS calculates the NLC parameters starting from May 10 through August 31, from mid to high latitudes (37-90°N) with a horizontal grid resolution of 1 degree of latitude and 3 degrees of longitude and a vertical resolution of 100 m from 77.8 to 94.1 km. To perform ice calculations, MIMAS requires time-dependent 3D input parameters such as zonal, meridional, and vertical winds ( $u$ ,  $v$ ,  $w$ ), as well

as ambient temperature ( $T$ ), air density ( $\rho$ ), and air pressure ( $p$ ) from LIMA (see Figure 2.1). Additionally, MIMAS includes an initial water vapour distribution ( $\text{H}_2\text{O}$ ) and solar Lyman alpha ( $\text{Ly}\alpha$ ) flux as a proxy for solar activity.

### 2.1.1 Background atmosphere model LIMA

LIMA is a non-linear, global 3D Eulerian grid point model that extends from the ground to the lower thermosphere (0 - 150 km) with a vertical resolution of 1.15 km. It aims to describe the thermal structure of the polar mesopause region. It considers the most important atmospheric processes, such as radiation, chemistry, and transport, and is well described in several publications (e.g. Berger, 2008; Lübken et al., 2013). The model uses a triangular horizontal grid structure with 41,804 grid points in each horizontal plane ( $\Delta x \approx \Delta y \approx 110$  km). The LIMA model in this study is nudged up to an altitude of 45 km to reanalysis data from NOAA CIRES (National Oceanic and Atmospheric Administration Cooperative Institute for Research in Environmental Sciences, 20CR; Compo et al. (2011)). Up to an altitude of 35 km the nudging coefficient is constant, then the nudging coefficient decreases linearly to zero up to an altitude of 45 km; above this limit altitude the model can run freely (Lübken et al., 2013). Including reanalysis data sets provides a forcing in the lower atmospheric layers and affects LIMA up to the middle atmosphere. The model simulations aim to obtain a homogeneous data set with a high temporal and spatial resolution, which is suitable for calculating climatologies in LIMA.

The other inputs for the LIMA model include trace gas concentrations for ozone and carbon dioxide, which influence temperature trends (e.g. Lübken et al., 2013). The temporal and latitudinal variations in the stratosphere and lower mesosphere for ozone are taken from the latest World Meteorological Organisation (WMO) report for the period 1961-1978 (Douglass and Fioletov, 2011) and the Solar Backscatter Ultraviolet (SBUV) satellite instrument for 1979-2021 (Lübken et al., 2013). Before 1961, stratospheric ozone was kept constant (according to 1961). The model's carbon dioxide ( $\text{CO}_2$ ) concentration is based on a monthly average time series from 1961 to 2019 measured at Mauna Loa (19°N, 155°W). Before 1961, historical  $\text{CO}_2$  data from Antarctic ice cores were used (Etheridge et al., 1998). In LIMA, the influence of small-scale internal gravity waves is considered by a non-linear spectral gravity wave parameterisation (Yiğit and Medvedev, 2013). In addition, LIMA uses daily  $\text{Ly}\alpha$  data from the Laboratory for Atmospheric and Space Physics (LASP) Interactive Solar Irradiance Data Centre (LISIRD) as a representative measure of solar activity from 1961 to 2021 (Machol et al., 2019). Before 1961, the monthly sunspot numbers were used to approximate the  $\text{Ly}\alpha$  values.

The main chemical and radiation processes included or parameterised in the model are as follows: Solar heating by oxygen and ozone absorption (Strobel, 1978), photolytic absorption of  $\text{Ly}\alpha$  by  $\text{O}_2$  according to Chabrillat and Kockarts (1998), chemical heat from exothermic chemical reactions (Mlynczak and Solomon, 1993), near-infrared (IR) carbon dioxide heating described by Ogibalov and Fomichev (2003). Cooling rates are parametrised in different altitude regions depending on the gas:  $\text{H}_2\text{O}$  from 30 to 100 km (Zhu and Newell, 1994), ozone from 30 to 80 km according to Fomichev and Shved (1988), carbon dioxide above 75 km (Fomichev et al., 1998), and atomic oxygen and  $\text{NO}_x$  in the lower thermosphere (Kockarts, 1980). Further details on the LIMA model can be found in Berger (2008).

LIMA mainly provides mesospheric dynamics and temperatures associated with many measurements over a multi-year period. The main strength of these dynamical fields is the seasonal and multi-year variabilities. For this reason, LIMA is mainly used for trend analyses for mesospheric temperatures and noctilucent clouds (Lübken et al., 2009; Lübken and Berger, 2011; Lübken et al., 2013b).

### 2.1.2 Water vapour source and solar activity

MIMAS uses initial water vapour profiles that are constant at each pressure level at the beginning. The water vapour profile was taken from the model simulations of Körner and Sonnemann (2001), corresponding to an average of over 10 days (Berger and Zahn, 2002). This profile is also used for simulations with the Community Aerosol and Radiation Model for Atmospheres (CARMA) ice model, whereby Wilms (2016) has described, among other things, that the water vapour profile fits well with ground-based observations (Seele and Hartogh, 1999) and satellite observations (Hervig et al., 2009). Below the lower boundary of MIMAS, two processes determine the mixing ratio of H<sub>2</sub>O in the stratosphere: (i) transport of H<sub>2</sub>O from the troposphere and (ii) oxidation of methane (CH<sub>4</sub>). The oxidation of each CH<sub>4</sub> molecule produces two H<sub>2</sub>O molecules. Methane is almost completely converted to H<sub>2</sub>O in the mesosphere by photochemical processes (Lübken et al., 2018). Transport of H<sub>2</sub>O from the troposphere has not changed on centennial time scales, whereas variations in more recent decades are likely (Hegglin et al., 2014). MIMAS assumes that the transport of H<sub>2</sub>O from the troposphere is constant. Therefore, the increase in H<sub>2</sub>O is primarily due to (ii), i.e. the increase in CH<sub>4</sub> concentration (Lübken et al., 2018). For more details on this parametrization of H<sub>2</sub>O from methane, see Lübken et al. (2018). This mesospheric water vapour is transported by dynamic fields calculated by LIMA, distributed by turbulent diffusion and reduced by photodissociation through the solar Ly $\alpha$  radiation.

LIMA and MIMAS use daily solar Ly $\alpha$  fluxes from the LISIRD as a proxy for solar activity from 1961 to 2019 (Machol et al., 2019). Before 1961, the monthly sunspot numbers were used to estimate the Ly $\alpha$  values. Ly $\alpha$  variations in LIMA are one of the causes of atmospheric temperature variations, while Ly $\alpha$  variations in MIMAS cause the photolysis of H<sub>2</sub>O (see Figure 2.1). In LIMA, fluctuations of other bands, namely the Chappius, the Huggins, the Hartley, and the Schumann-Runge continua, are considered. The variations of these bands are parameterised using the Ly $\alpha$  values according to Lean et al. (1997). More details of LIMA and their parameterisation schemes are well described in publications (e.g. Berger, 2008; Lübken et al., 2013).

## 2.2 Microphysical processes

This section describes the microphysical processes of NLCs and how they are implemented in the MIMAS model. The individual modules of the model include the formation of ice particles and the redistribution of water vapour and dust particles, which serve as possible condensation nuclei (CN) for ice formation. They settle due to gravity and consume the available water vapour on their way through the atmosphere. During this movement, the particles are transported further by mean winds (vertical and horizontal) and small-scale movements, i.e. waves and turbulence. Once the particles have reached a size of more than 30 nm, they scatter light so efficiently that they can eventually be observed with optical instruments on the ground or in space (Rapp and Thomas, 2006).

The main components essential for the microphysical processes included in MIMAS are described in the following sections. A more detailed description of the microphysical processes involved in noctilucent clouds and their implementation in MIMAS is well discussed in publications (Berger and Zahn, 2002; Zahn and Berger, 2003; Rapp and Thomas, 2006).

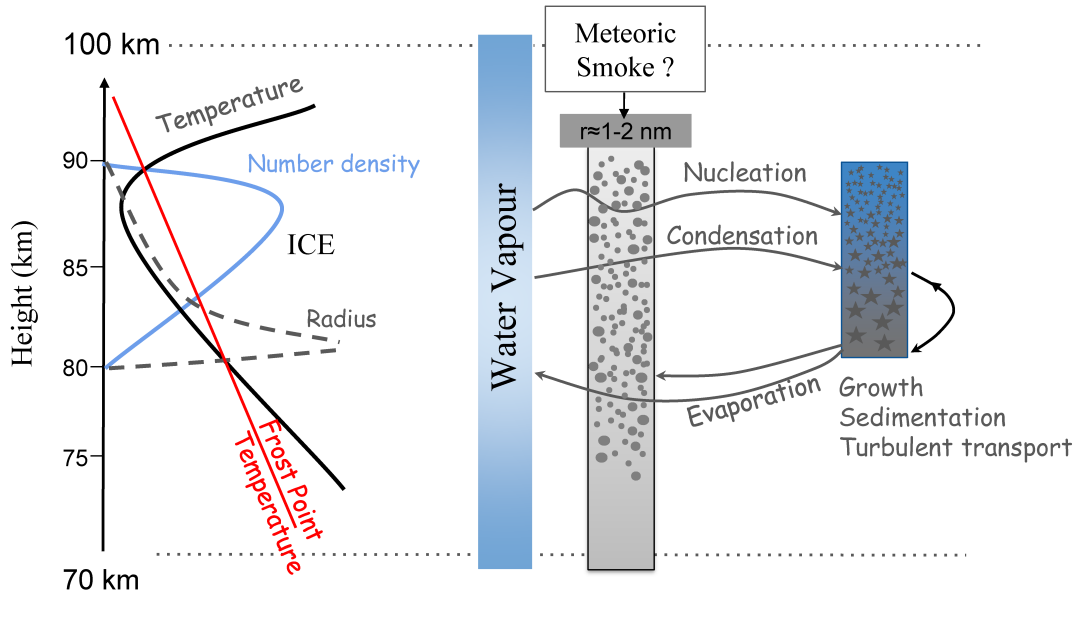


FIGURE 2.2: Schematic representation of the formation, growth and sedimentation of NLC and the redistribution of water vapour and dust particles, adapted from Kiliani (2014).

### 2.2.1 Dust particles

The availability of dust particles, which can act as condensation nuclei (CN), significantly influences the formation of ice particles. Aerosols from the troposphere and stratosphere are generally not transported into the mesosphere (Rapp and Thomas, 2006), so all CNs at these altitudes are generated locally. Rosinski and Snow (1961) were the first to suggest that when extraterrestrial meteoroids enter the Earth's atmosphere, a significant portion of them vapourise at 80-100 km altitude. The trail of ablated material from these impacts could condense into tiny particles, which can act as condensation nuclei for ice formation. The computer resources limit the number of particles in a Lagrangian model: In MIMAS, 40 million dust particles are available for microphysical processes, and they act as potential nuclei for ice particles in a supersaturated cold atmosphere. Each particle is a proxy for  $7.4 \times 10^{18}$  real particles distributed over the model grid volume. The number density in MIMAS is calculated by scaling the number of model particles by this factor ( $7.4 \times 10^{18}$ ) and dividing by the grid volume.

Hunten et al. (1980) investigated the properties of these "meteoritic smoke particles" in detail and modelled their formation, including the processes of coagulation, sedimentation and turbulent diffusion. The size distribution of the dust particles in MIMAS is based on Hunten et al. (1980). At the beginning of a MIMAS simulation, 40 million model CN sizes between 1.2 and 3.7 nm are assigned and discretised

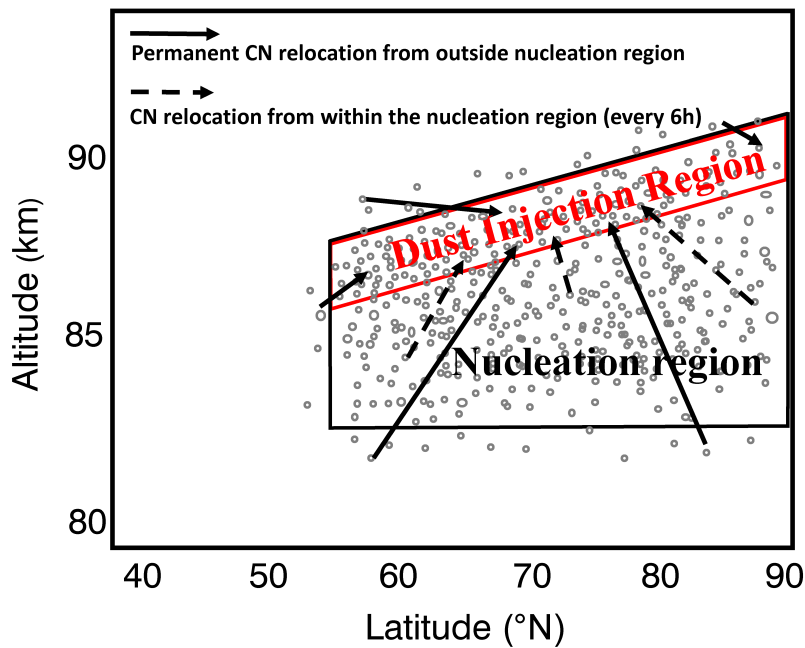


FIGURE 2.3: Schematic representation of meteoric dust in MIMAS, adapted from Kiliani (2014)

into five bins with a width of 0.5 nm each. The distribution of the dust particles among the individual classes is exponential and is as follows: 86.5 % (1.2-1.7 nm), 11.7 % (1.7-2.2 nm), 1.7 % (2.2-2.7 nm), 0.2 % (2.7-3.2 nm) and 0.02 % (3.2-3.7 nm). All particles are randomly distributed at 55°-90°N and within a narrow altitude range of 1 km around the mesopause (dust injection region). The dust initialisation assumes a uniform distribution along latitudes, so the number of dust particles per grid volume is the same. During the model simulation, all condensation nuclei are transported with the wind field and sediment at a speed that depends on their size and the background conditions, such as air density and temperature.

Due to the 3D transport, some dust particles reach the boundary of the model domain. In this case, the dust particles are relocated randomly within the initial dust injection region (see Figure 2.3). Two processes stabilise the dust particle distribution shown in Figure 2.3. CNs transported equatorward of the 55° latitude circle and located below 83 km or more than 1 km above the mesopause are considered outside the potential ice nucleation region. These particles are then randomly relocated to a new position >55° and within 1 km of the mesopause (the dust injection region). This ensures a quasi-stable state where dust particles remain permanently available for ice nucleation throughout the season.

## 2.2.2 Water vapour in the summer MLT region

Modelling water vapour formation in MIMAS requires a detailed description of the chemical and dynamic processes. Due to this complexity, a parameterisation of water vapour formation is used in MIMAS. In the model, water vapour is transported by the dynamic fields, spread by turbulent diffusion, and reduced by photodissociation due to solar UV radiation (Fig. 3.1). The transport follows Walcek's advection algorithm (Walcek and Aleksic, 1998; Walcek, 2000). This algorithm

adapts the initial climatology over 10 days to real tidal variations, starting the simulation 10 days before the first ice formation. Furthermore, the redistribution of water vapour through interaction with ice particles is taken into account using the advection algorithm (Berger and Zahn, 2002)

To simulate the flow of a chemical constituent such as water vapour on wind fields, the tracer concentration must be transported within the model grid. For a passive chemical tracer moving with velocity  $u$  in one dimension, this means solving the continuity equation

$$\frac{\partial c}{\partial t} = -\frac{\partial(u \cdot c)}{\partial x} \quad (2.1)$$

where  $c$  is the concentration of the tracer or constituent. In addition to the advection with wind, the water vapour in MIMAS is continuously mixed by turbulent eddy diffusion described by Fick's second law

$$\frac{\partial c}{\partial t} = K \cdot \frac{\partial^2 c}{\partial x^2} \quad (2.2)$$

where  $K$  is the diffusion coefficient. In multiple dimensions, the general form of the equation is  $\frac{\partial c}{\partial t} = K \cdot \nabla^2 c$ . Turbulent diffusion is isotropic, and its horizontal component is significantly smaller than the vertical component due to the significant differences in the model scales (approx. 100 km to 100 m). Therefore, only the vertical diffusion ( $K_{zz}$ ) is explicitly implemented in MIMAS. The diffusion coefficient  $K_{zz}$  was derived from rocket experiments with ionisation measuring devices over Andøya in northern Norway for summer conditions (Lübken, 1997) and is time-independent (Berger and Zahn, 2002). MIMAS uses  $K_{zz}$  values that are reduced to 25% of the values in Lübken (1997) to account for the turbulence intermittency (Kiliani, 2014). Despite the reduced  $K_{zz}$  values at the base of the NLC, diffusion is still essential to compensate for the freeze-drying effect in which NLCs consume water vapour in their region of formation. A potential latitude and time dependence of  $K_{zz}$  is not considered, as this is currently unknown and requires a comprehensive understanding of the process of gravity wave breaking that causes mesospheric turbulence.

Water vapour at NLC altitudes is largely exposed to sunlight, which contains much more short-wave UV radiation than in the troposphere. At wavelengths shorter than about 200 nm, UV radiation can dissociate water molecules into a hydroxyl radicals (OH) and atomic hydrogen in a process known as photodissociation. These hydroxyl radicals can then participate in various atmospheric chemical reactions, affecting the composition and chemistry of the atmosphere. Photodissociation of water vapour is an important process in atmospheric chemistry, particularly in the upper atmosphere where solar UV radiation is more intense. Most solar UV radiation is absorbed by oxygen in the thermosphere, but the Ly $\alpha$  radiation is intense, less attenuated, and penetrates into the mesosphere. Ly $\alpha$  radiation is the primary cause of H<sub>2</sub>O photolysis and varies by a factor of two between solar minimum and maximum (Woods et al., 2000). Since NLCs are very sensitive to water vapour concentration, the variations in H<sub>2</sub>O photolysis during a solar cycle significantly affect the properties of NLCs (Lübken et al., 2009). The reduction of water vapour is expressed in the model by the photodissociation rate of water vapour through the solar Ly $\alpha$  flux (see Berger and Zahn, 2002). The solar cycle also affects NLCs through

indirect mechanisms: Increased UV absorption by molecular oxygen increases temperatures in the mesosphere and thus influences the formation of NLCs.

The growth of NLC leads to dehydration at higher altitudes (83-89 km), as ice particles form by consuming background H<sub>2</sub>O, while the sublimation of these ice particles leads to hydration at lower altitudes (about 78-83 km) (Lübken et al., 2009; Hervig et al., 2003). This phenomenon is known as the "freeze-drying" effect.

### 2.2.3 Particle nucleation, growth and transport

A region supersaturated with water vapour is required for water vapour to nucleate around meteor smoke particles, which are the building blocks of NLCs. The degree of saturation of air with water vapour is calculated as  $S = \frac{p_{\text{H}_2\text{O}}}{P_{\text{ice}}}$ , where  $p_{\text{H}_2\text{O}}$  is the H<sub>2</sub>O partial pressure ( $c_{\text{H}_2\text{O}} \cdot P_{\text{atm}}$ ) (where  $c_{\text{H}_2\text{O}}$  is the water vapour mixing ratio), and  $P_{\text{ice}}$  is the saturation vapour pressure over a flat ice surface. An environment with a value  $S > 1$  is supersaturated, which means that ice particles can grow under these conditions, while  $S < 1$  is subsaturated and leads to sublimation of the ice particles.

Ice particles may form in the mesosphere through heterogeneous nucleation around meteoric dust and homogeneous nucleation (Murray and Jensen, 2010). Homogeneous nucleation requires extremely high supersaturation ( $S > 1000$ ). Sugiyama (1994) suggested nucleation by ion recombination as an additional process, but Gumbel et al. (2003) noted that, although it could occur under certain circumstances, it probably does not play a significant role in nucleation. Heterogeneous nucleation, highlighted by Gadsden (1982) and Turco et al. (1982), is considered the most important process in forming NLC. Hence, this is the only nucleation mechanism integrated into MIMAS (Berger and Zahn, 2002).

To calculate the degree of saturation ( $S$ ), we need a formula for the saturation vapour pressure over a plane ice surface ( $p_{\text{ice}}$ ). At mesosphere temperatures,  $p_{\text{ice}}$  is hardly known, as only a few direct measurements are available. The saturation vapour pressure over a flat ice surface ( $p_{\text{ice}}$ ) is calculated in MIMAS using the formula according to Murphy and Koop (2005):

$$p_{\text{ice}} = e^{9.550426 - \frac{5723.265}{T_p} + 3.53068 \log T_p - 0.00728332 T_p} \quad (2.3)$$

where  $T_p$  is the temperature of the ice particles, which is higher than the temperature of the ambient air because the ice particles are heated by the absorption of solar or terrestrial infrared light (Eidhammer and Havnes, 2001). The following relationship expresses the temperature difference between the ice particle and the environment:

$$\Delta T = T_p - T \propto \frac{r}{a \cdot n_{\text{air}}} \quad (2.4)$$

where  $r$  is the particle radius, and  $n_{\text{air}}$  is the number density of air (Rapp and Thomas, 2006). The accommodation coefficient ( $a$ ) describes the efficiency of thermal energy transfer from the ice particle to the ambient air and is between 0 and 1 (Rapp and Thomas, 2006). It is currently a little-known parameter and has yet to be proven experimentally or theoretically. In MIMAS, a value of  $a = 0.5$  is assumed for

the accommodation coefficient (Kiliani, 2014), and, thus, a moderate energy transfer from the ice particle to the air molecule.

A degree of saturation ( $S$ ) of 1 is insufficient for a meteor dust particle to form a layer of ice (i.e. heterogeneous nucleation). Because the surface tension of small particles, causing an increase in pressure within the particle (Laplace pressure), accelerates the droplet's evaporation, and this dependence of the saturation pressure on the particle radius is known as the Kelvin effect:

$$p_{\text{sat}}(r) = p_{\text{ice}} \cdot \exp\left(\frac{2m_{\text{H}_2\text{O}} \cdot \sigma}{k_B \cdot T_p \cdot \rho \cdot r}\right) \quad (2.5)$$

where  $m_{\text{H}_2\text{O}} = 2.99 \times 10^{-26}$  kg is the molecular mass of water,  $\rho = 932$  kg/m<sup>3</sup> the density of ice,  $k_B = 1.3085 \times 10^{-23}$  JK<sup>-1</sup> is the Boltzmann constant, and  $\sigma$  is the surface tension of the interface between ice and water vapour (Tolman, 1949). For nanometer-size spherical ice particles,  $\sigma$  is

$$\sigma = \frac{\sigma_\infty}{1 + \frac{2\delta}{r}} \quad (2.6)$$

where  $\delta = 1.5 \times 10^{-10}$  m is an empirical factor (Turco et al., 1982) and  $\sigma_\infty$  is the surface tension over a flat ice surface according to Hale and Plummer (1974). This surface tension is defined as follows:

$$\sigma_\infty = 0.141 - 1.5 \times 10^{-4} \cdot T \quad (2.7)$$

when the degree of saturation  $S = \frac{p_{\text{H}_2\text{O}}}{p_{\text{ice}}}$  becomes greater than  $\frac{p_{\text{sat}}(r)}{p_{\text{ice}}}$ , a condensation nucleus of radius  $r$  transforms into an ice particle. MIMAS does not consider condensation nuclei with a radius of less than 1.2 nm due to the very low probability of ice formation and to avoid unnecessary calculations.

The growth rate of ice particles in the mesosphere is provided by Hesstvedt (1961):

$$\frac{dr}{dt} = \frac{\alpha}{\rho} \sqrt{\frac{m_{\text{H}_2\text{O}}}{2\pi \cdot k_B \cdot T_p}} \cdot p_{\text{sat}}(r) \cdot (S(r) - 1) = \frac{\alpha}{\rho} \sqrt{\frac{m_{\text{H}_2\text{O}}}{2\pi \cdot k_B \cdot T_p}} \cdot (p_{\text{H}_2\text{O}} - p_{\text{sat}}(r)) \quad (2.8)$$

A condensation coefficient of  $\alpha = 0.83$  (Gadsden and Schröder, 1989) explains how probable a water molecule will stick to an ice crystal when they collide. If  $p_{\text{sat}}(r)$  exceeds  $p_{\text{H}_2\text{O}}$ , the rate becomes negative, which means that the particle starts to sublimate.

Ice/dust particle motion in MIMAS is a combination of advection, sedimentation and turbulent diffusion. Only advection applies for horizontal motion, and sedimentation and eddy diffusion are important for vertical motion. The sedimentation velocity depends on the radius of the ice particle and the density and temperature of the surrounding air. Sedimentation velocity ( $w_s$ ) for the dust and ice particles is derived from Reid (1975):

$$w_s = -\frac{g \cdot \rho \cdot r_n}{2n_{\text{atm}}} \sqrt{\frac{\pi}{2m_{\text{atm}} \cdot k_B \cdot T}} \quad (2.9)$$

where  $g$  is the acceleration due to gravity for the mesosphere is given as  $9.55 \text{ m/s}^2$  (Berger and Zahn, 2002), and  $\rho = 932 \text{ kg/m}^3$  is the density of ice.  $m_{\text{atm}} = 4.845 \times 10^{-26} \text{ kg}$  is the molecular mass of air, and  $n_{\text{atm}}$  is the number density of air molecules per  $\text{m}^3$ . Note that the equations provided for nucleation, growth, and sedimentation of particles are based on the assumption that the particles are spherical. (Kiliani, 2014). Ice shapes such as plates or needles can influence the sedimentation velocity, the growth rate, the Kelvin effect and brightness (e.g. Kiliani, 2014; Baumgarten, 2001; Turco et al., 1982). There are currently only a few studies on non-spherical particles in the mesosphere (Kiliani, 2014). Furthermore, the physical mechanism behind the non-spherical growth is currently unknown and could be due to the ice crystal structure or the charge of the ice particles (Wilms, 2016). Due to these uncertainties and a significantly higher computational effort for the microphysics and light scattering by non-spherical particles, the calculations in MIMAS are performed by assuming spherical particles.

Ice and dust particles are also affected by eddy diffusion. Like for water vapour (section 2.2.3), only vertical diffusion is considered in MIMAS because the horizontal component has a minor effect on NLC. Mixing scales in the upper mesosphere typically range from 10 to 100 meters, while turbulent velocities peak at several meters per second at altitudes of 90 kilometres (Lübken, 1997). The transport processes of ice and dust particles implemented in MIMAS are well described in publications (Berger and Zahn, 2002; Zahn and Berger, 2003).

## 2.3 Model output and numerical experiments

The main output of the model is the trajectories of 40 million dust and ice particles (see Figure 2.1). In addition, the model calculates various properties of the ice particles, including brightness, number density, radius, ice water content (IWC), extinction coefficient for different wavelengths, etc. Various model simulations are carried out to achieve the objectives discussed in Section 1.3.

As discussed earlier, NLCs are significantly influenced by the solar cycle as it affects water vapour and background temperature. When NLCs are present, the solar cycle influences the water vapour concentration in the upper mesosphere in two ways: directly through photolysis and indirectly through temperature changes. These temperature changes impact NLC formation, thereby influencing freeze-drying and affecting  $\text{H}_2\text{O}$  levels at the time and location of NLC formation.  $\text{Ly}\alpha$  variations in LIMA cause atmospheric temperature variations, while  $\text{Ly}\alpha$  variations in MIMAS cause photolysis of  $\text{H}_2\text{O}$ . Therefore, it is possible to study the effects of the solar cycle on  $\text{H}_2\text{O}$  due to temperature changes and photolysis separately by performing model simulations with constant and varying  $\text{Ly}\alpha$  in MIMAS and LIMA. Four model runs were conducted for this study, as described in Table 2.1. For runs E, F, and G, LIMA and MIMAS model simulations with constant  $\text{CO}_2$  and  $\text{CH}_4$  were performed to filter out the effects of GHGs on temperature and water vapour variations. Further details on these model runs are discussed in Section 4 (summary of Vellalassery et al. (2023), see Appendix A).

Model run	LIMA		MIMAS		Water vapour solar cycle response affected by
	CO <sub>2</sub>	Ly $\alpha$ T effect	CH <sub>4</sub>	Ly $\alpha$ photolysis effect	
A	↑	↑	↑	↑	-Temperature change(Ly $\alpha$ +CO <sub>2</sub> ) -Photo dissociation -varying CH <sub>4</sub> (H <sub>2</sub> O source)
E	↔ 1997	↑	↔ 1997	↑	-Temperature change -Photo dissociation
F	↔ 1997	↑	↔ 1997	↔ 1997	- Temperature change
G	↔ 1997	↔ 1997	↔ 1997	↑	- Photo dissociation

TABLE 2.1: MIMAS simulations carried out under different background conditions. The horizontal arrow stands for constant values for the respective year, and the vertical arrow stands for varying parameters. The effect of solar Ly $\alpha$  variations on H<sub>2</sub>O is shown for each run in the last column

To investigate the impact of increasing GHG emissions on the response of NLCs and the background atmosphere to the solar cycle, MIMAS model simulations were performed for years from 1849 to 2021 (covering 15 complete solar cycles) for three different scenarios based on constant and varying GHGs. Three model runs are carried out for this study, namely run A, B, and C. In run A, both CO<sub>2</sub> and CH<sub>4</sub> (H<sub>2</sub>O) increase. In run B, only the CO<sub>2</sub> concentration increases, while the CH<sub>4</sub> concentration remains constant. In run C, the CH<sub>4</sub> concentration increases while the CO<sub>2</sub> concentration remains constant.

In this thesis, the following symbols refer to these model scenarios: CO<sub>2</sub> ↑, CH<sub>4</sub> ↑ for Run A; CO<sub>2</sub> ↑, CH<sub>4</sub> ↔ for Run B; and CO<sub>2</sub> ↔, CH<sub>4</sub> ↑ for Run C. This work mainly concentrates on the core of the NLC season, the month of July, and on three latitude bands, namely  $58 \pm 3^\circ\text{N}$ ,  $69 \pm 3^\circ\text{N}$ , and  $78 \pm 3^\circ\text{N}$ , which are labelled as 'middle', 'high', and 'arctic' latitudes.

The increase in NLC brightness caused by the rise in greenhouse gases (GHGs) will presumably absorb more solar radiation in the future. To study this, we consider run C, i.e., only the increase in methane (which is the primary factor that causes increasing brightness and IWC in NLCs), with temperatures and dynamics remaining constant. The future methane development in this simulation is based on the (IPCC Fourth Assessment Report (AR4)). More specifically, based on the Representative Concentration Pathway 8.5 (RCP 8.5) scenario described in Riahi et al. (2011). This scenario was chosen because it represents the maximum increase in methane; nevertheless, last year's increase shows that RCP 8.5 is closer to reality than other IPCC future scenarios.

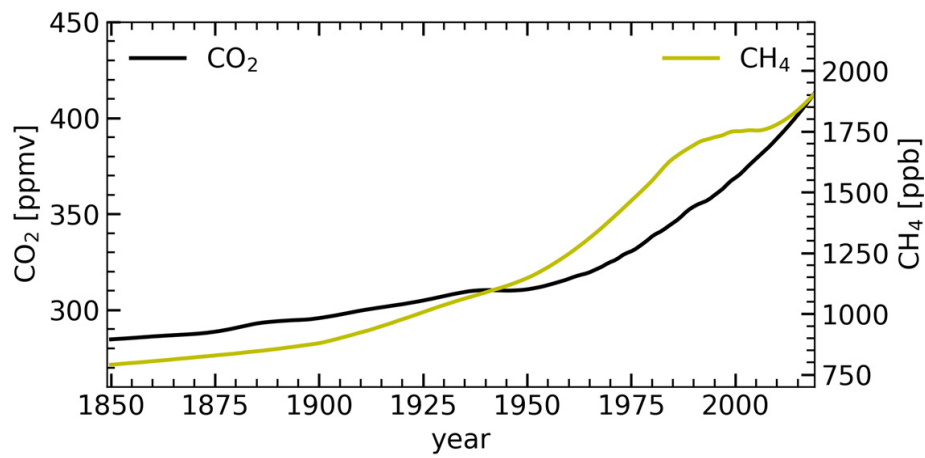


FIGURE 2.4: Time series of CO<sub>2</sub> and CH<sub>4</sub> concentrations used in the model runs (1849-2019). Figure taken from Vellalassery et al. (2024), Fig. 1.

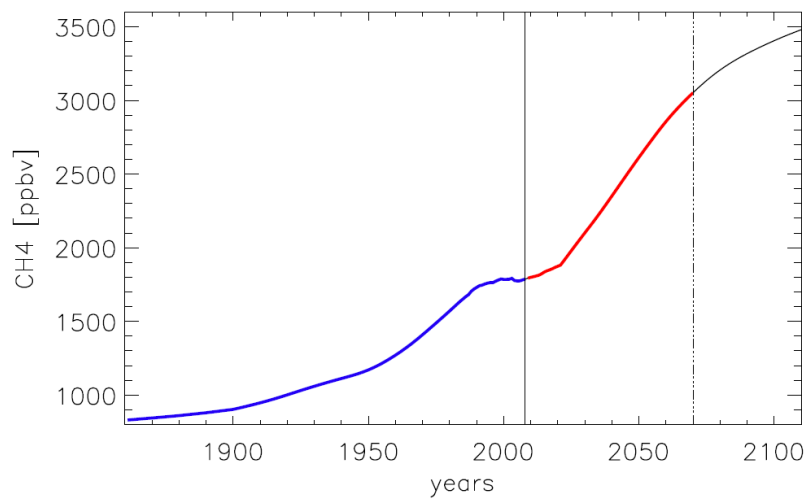


FIGURE 2.5: Time series of CH<sub>4</sub> concentrations used in the model runs including future CH<sub>4</sub> projections taken from IPCC AR4 (red). Figure taken from Lübken et al. (2024), Fig. 1.



## Chapter 3

# Trends in NLCs and background atmosphere

This chapter briefly discusses the trends in the background atmosphere and NLCs based on previous model studies using LIMA/MIMAS and different observations, including satellites and ground-based measurements. Long-term trends in temperature and background water vapour at NLC altitudes are briefly discussed in Section 3.1. Long-term trends in NLCs and the impact of increasing CO<sub>2</sub> and CH<sub>4</sub> emissions are discussed in Section 3.2. The influence of the 11-year solar cycle on NLCs, based on various observations and models, is presented in Section 3.3.

### 3.1 Long-term trends in temperature and water vapour

Mesospheric temperature trends have been increasingly studied in recent years due to significant evidence of larger trends than the troposphere and stratosphere (Berger and Lübken, 2011; Lübken et al., 2013). Very little is known about temperature trends in the summer mesopause region, and no significant progress has been made, especially in the high-latitude summer mesosphere (Lübken et al., 2018). Roble and Dickinson (1989) suggest that increasing GHGs cool the middle atmosphere due to increased infrared emissions into space. Following their study, improved modelling has helped to investigate the main factors driving these trends, in particular the increase in GHGs (e.g. Akmaev et al., 2006; Schmidt et al., 2006; Garcia et al., 2007). Several recent reviews have summarised the observations and theoretical understanding of these trends (e.g. Beig, 2011, Laštovička, 2013, Lübken et al., 2011, and Lübken et al., 2013).

Satellite observations of stratospheric temperature began in 1970 with stratospheric sounding units (SSU), which provide the global decadal data set for trend analyses in the upper stratosphere (Randel et al., 2009). For the mesosphere, however, there are no direct satellite temperature observations on a multi-decadal time scale (Berger and Lübken, 2011). Also, the uncertainties in mesospheric temperature are larger, and there are discrepancies between observations and modelling (Beig et al., 2003). The measurements based on the reflection height of radio waves performed since 1959 at 82 km altitude are the longest available data sets in the mesopause based on active soundings. It shows a decrease of 1.5 km in the reflection height in the last 50 years (Bremer and Berger, 2002; Bremer and Peters, 2008). Many studies based on model simulations show that increasing GHGs cause a cooling in the middle atmosphere (e.g., Akmaev et al., 2006; Schmidt et al., 2006; Garcia et al., 2007). Akmaev et al. (2006) investigated these effects from 1980-2000. In the

summer hemisphere, they find a maximum trend of about -2 K/decade in the mesosphere. This is generally consistent with model results, especially since the trends in 1980-2000 are somewhat larger compared to the entire period considered in LIMA (see Figure 5 in Lübken et al., 2013).

Berger and Lübken (2011) investigated the temperature trends in the mesosphere at mid-latitudes in summer using LIMA simulations for 1961-2009. They have compared the simulated temperature trends with observations, such as satellite measurements, radio wave reflection height measurements, and lidar observations. The study found an excellent agreement between temperature trends from LIMA and observations. It shows that the temperature trend in the mesosphere is  $\sim 10$  times larger (2-3 K/decade) and opposite (cooling trend) compared to global mean temperature trends at Earth's surface (+0.2 K/decade). The temperature trends comparison between an earlier version of LIMA with the global circulation model WACCM (Whole Atmosphere Community Climate Model) for a shorter period also shows good agreement (Garcia et al., 2007; Lübken et al., 2013). The height profiles of long-term temperature trends calculated by LIMA are consistent with lidar measurements at the Observatory of Haute-Provence in southern France (44°N) in summer (compare Figure 10a in Keckhut et al. (2011) to Figure 1b in Berger and Lübken (2011)). It is important to note that the temperature trends at geometric heights are generally larger and drastically different from those at constant pressure levels.

Lübken et al. (2018) analysed the temperature trends from LIMA for a fixed geometric height and mean pressure level (see Figure 3.1) for 138 years from 1871 to 2008. This mean pressure ( $p_{\text{mean}} = 5.962 \times 10^{-10}$  hPa) is given by the mean value of all 138 mean pressure levels of the maximum NLC backscatter (brightness). The temperature has decreased by 7 K since 1871 at a fixed geometric altitude of 83 km, but not significantly at a fixed pressure level. This is because increased CO<sub>2</sub> leads to cooling in the stratosphere and lower mesosphere (Roble and Dickinson, 1989; Garcia et al., 2007; Berger and Lübken, 2011; Lübken et al., 2013; Marsh et al., 2013). At NLC altitudes, this cooling leads to a decrease in the altitude of constant pressure level, referred to as the shrinking effect (Lübken et al., 2009). Due to the negative temperature gradient at NLC altitudes, this shift causes apparent cooling at geometric altitudes. The temperature decrease in fixed geometric height (83 km) was about -1.7 K from 1871 to 1960 and became -5 K from 1960 to 2008 due to an accelerated increase in CO<sub>2</sub> emissions after 1960. Generally, trends at geometric heights larger than at constant pressure levels are explained by atmospheric shrinking (Berger and Lübken, 2011; Lübken et al., 2021). Temperatures at fixed pressure levels near the NLC layer remain almost constant across all latitudes, indicating minimal temperature changes at NLC altitudes, while significant cooling occurs at the lower mesosphere (Berger and Lübken, 2015). Reviewing previous studies shows that about 66% of the cooling observed in the model at NLC altitudes (about 83 km) is due to atmospheric shrinking, while the remaining percentage is caused by direct radiative cooling associated with the increase in CO<sub>2</sub> levels (as shown in a comparison between Figure 11 in Lübken et al. (2013) and Figure 14 in Berger and Lübken (2015)).

Water vapour is one of the key minor constituents in the middle atmosphere, and it is the primary source of chemically active hydrogen radicals, influencing the chemistry of all other chemically active minor constituents (Brasseur and Solomon, 2005; Hartogh et al., 2010). Water vapour trends at high latitudes have indicated that there has been an overall increase in water vapour concentrations in the mesosphere

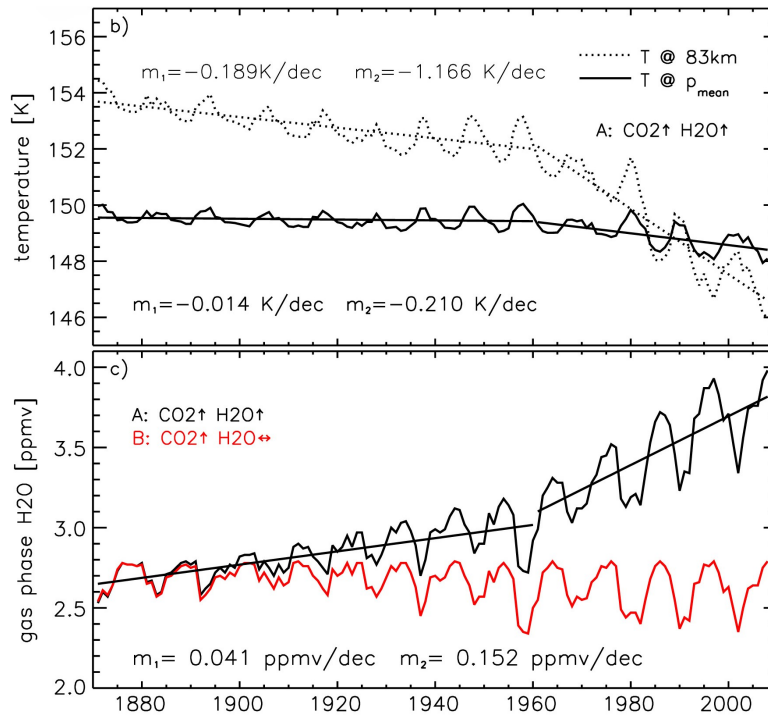


FIGURE 3.1: Time series of (b) temperature at a fixed geometric height (83 km) as a dotted line and at constant pressure level ( $5.962 \times 10^{-3}$  hPa: mean pressure of NLC maximum brightness height) as a solid line; (c) mixing ratios of gas phase water vapour at  $p_{\text{mean}}$  (assuming that ice formation had not occurred) for Runs A and B. Note that H<sub>2</sub>O values for Runs A and C are identical. In panels (b) and (c), linear fits for Run A are shown for the periods before ( $m_1$ ) and after ( $m_2$ ) 1960, respectively. The slopes are listed in the inserted legend. Figure taken from Lübken et al. (2018), Fig. 1.

and upper stratosphere over time (Hartogh et al., 2010). As mentioned earlier, observations of water vapour at mesospheric heights are relatively limited compared to lower layers of the atmosphere. However, combined observations and improved modelling capabilities are helping to improve our understanding of water vapour trends in this critical atmospheric region.

Using model simulations, Grygalashvily and Sonnemann (2006) investigated the impact of increasing methane concentration (mainly oxidised to water vapour in the middle atmosphere) on the water vapour distribution at higher latitudes. They found an expected increase in water vapour in the middle atmosphere, but with a certain time lag of some years, due to the long transport time of all components through the middle atmosphere and the long chemical lifetime of methane. These factors have been incorporated into MIMAS to model water vapour concentrations using a parametrisation discussed by Lübken et al. (2018) (see section 2.1.2).

Considering the effects of increasing methane, the mixing ratio of water vapour has increased by around 0.15 ppmv/decade since 1960 (Lübken et al., 2018, see Figure 3.1). The total increase is about 40% since 1871 (approximately 1 ppmv), which is entirely caused by increased methane oxidising to H<sub>2</sub>O. Few observation-based studies on water vapour trends in the summer mesopause region at middle latitudes are available (e.g., Hervig et al., 2016a; Remsberg et al., 2018). Observations from the Solar Occultation For Ice Experiment (SOFIE) on board NASA's Aeronomy of Ice

in the Mesosphere (AIM) satellite (Figure 6d in Hervig et al., 2016b) show that the H<sub>2</sub>O mixing ratio has been around 4 ppmv in recent years, which is consistent with MIMAS, as shown in 3.1c. The latest study by Remsberg et al. (2018) shows a water vapour trend of approximately 5% per decade at 52.5°N and 80 km, corresponding to ~0.175 ppmv/decade, which is consistent with the trends calculated in MIMAS (~0.15 ppmv/decade) shown in Figure 3.1c.

## 3.2 Long-term trends in noctilucent clouds

NLCs were first observed in 1885, two years after the major volcanic eruption of Krakatoa (e.g. Backhouse, 1885), which injected huge amounts of H<sub>2</sub>O, dust and large quantities of minor constituents into the atmosphere. The sudden appearance of NLCs in 1885 seems to be related to the eruption of Krakatoa (Schröder, 1999). An analysis of NLC data from the Arctic Lidar Observatory for Middle Atmosphere Research (ALOMAR) shows noticeable trends since 1998. The study shows increased occurrence and brightness of NLCs during the observation period (Fiedler et al., 2016). NLCs are proposed as an indicator of atmospheric change in the mesopause region (Thomas, 1996) primarily because they are supposed to respond to increasing methane and carbon dioxide. As mentioned, one methane molecule undergoing oxidation in the stratosphere and stratopause produces two H<sub>2</sub>O molecules.

Berger and Lübken (2015) used the MIMAS ice model to investigate the trends of NLCs in response to long-term changes in mesospheric temperatures and water vapour in the northern high latitudes for the summer period 1961-2013. The model simulations show increased occurrence, brightness and ice water content (IWC) of NLCs. The trends in the overall seasonal mean IWC are different at different latitudes. While no significant trend is observed in the mid-latitudes (50°N-55°N), highly substantial trends of 6.5-6.7 g km<sup>-2</sup>/decade are observed in the latitude band of 74°N-82°N in the period from 1961 to 2013. The validation of the model with the SBUV satellite observations constituting the longest systematic NLC data set available (1979 to present) shows good agreement with a threshold in ice water content (IWC > 40 g km<sup>-2</sup>) within the band from 74°-82°N latitude. Both model and SBUV data showed an increase in ice water content in the 74°-82°N latitude band with significant IWC trends of  $2.8 \pm 2.1$  g km<sup>-2</sup>/decade and  $2.4 \pm 2.0$  g km<sup>-2</sup>/decade, respectively (Berger and Lübken, 2015). The study proves that the microphysical ice model MIMAS is a valuable tool for analysing long-term changes in various NLC parameters such as ice water content (IWC), frequency of occurrence, brightness and altitude (Berger and Lübken, 2015). The Solar Occultation for Ice Experiment (SOFIE) instrument on the Aeronomy of Ice in the Mesosphere (AIM) satellite has been observing the mesosphere since 2007 to provide a basis for understanding PMC variability (Russell et al., 2009). The SOFIE/AIM instrument measured a mean value of IWC about 59 g km<sup>-2</sup> at mid-latitudes in July 2015, using a threshold value of IWC > 40 g km<sup>-2</sup> (see Figure 3 in Hervig et al., 2016b). This perfectly agrees with the IWC values from MIMAS, namely IWC = 58-59 g km<sup>-2</sup> (Figure 3c in Lübken et al., 2018), using the same threshold.

Lübken et al. (2018) investigated the long-term development of noctilucent clouds and the influence of increasing greenhouse gases such as CH<sub>4</sub> and CO<sub>2</sub> using the MIMAS simulations for 1871-2008. Three different MIMAS simulations were performed based on different greenhouse gas conditions, providing model runs: (A) CO<sub>2</sub> increasing, CH<sub>4</sub> increasing (CO<sub>2</sub> ↑, H<sub>2</sub>O ↑); (B) CO<sub>2</sub> increasing, CH<sub>4</sub> constant

(CO<sub>2</sub> ↑, CH<sub>4</sub> ↔); and (C) CO<sub>2</sub> constant and CH<sub>4</sub> increasing (CO<sub>2</sub> ↔, H<sub>2</sub>O ↑). The study shows that increasing H<sub>2</sub>O caused by increasing CH<sub>4</sub> is mainly responsible for the increase in NLC brightness and IWC, while CO<sub>2</sub> increase alone mainly caused the downward shift of NLC layers in geometric height, which is attributed to atmospheric shrinking. The rate of decrease in NLC heights is consistent with the long-term observations of radio wave reflection heights since 1959 (see Figure 2a in Berger and Lübken, 2011).

### 3.3 Solar cycle response in noctilucent clouds

The 11-year solar cycle affects the upper atmospheric temperature and water vapour concentration, consequently affecting NLCs (see the 11-year cycle in temperature and H<sub>2</sub>O in Figure 3.1). Numerous studies have been conducted on the relationship between the 11-year solar cycle and the properties of NLC (e.g., DeLand et al., 2003; Hervig et al., 2016b; Hervig and Siskind, 2006; Hervig et al., 2019; Siskind et al., 2013). NLCs are predicted to decrease during solar maximum due to increased heating and photolysis of H<sub>2</sub>O (Garcia, 1989). Thomas et al. (1991) used observations from the Nimbus-7 SBUV instrument to demonstrate a solar activity dependence in NLC frequency. The 23 years of SBUV data confirm the inverse relationship between the frequency of NLC occurrence and solar activity, which was previously only observed in the NLC time series. The variations in temperature, water vapour, and NLCs due to solar cycle activity were confirmed by Upper Atmosphere Research Satellite (UARS) observations during solar cycle 22 (Hervig and Siskind, 2006). Previous studies using SBUV data have shown an increase in the frequency of the occurrence of NLCs in an anti-correlation with solar activity (Shettle et al., 2009). Studies on the NLC trend using the MIMAS model also predict a strong response to the solar cycle in NLCs, T and H<sub>2</sub>O after 1979 (e.g. Berger and Lübken, 2015; Lübken et al., 2009; Lübken et al., 2018). However, some recent studies (Fiedler et al., 2011; DeLand and Thomas, 2015; Hervig et al., 2016b; and Siskind et al. (2013)) reported that the response of NLCs to the solar cycle has been absent since 2002. A recent study based on satellite observations (Hervig et al., 2019) found that NLCs showed a clear anti-correlation with the solar cycle before 2002 and that this response has been absent in recent years. The study suggests that the main reason for this absence is the suppression of H<sub>2</sub>O's response to the solar cycle after 2005. The analysis of the H<sub>2</sub>O time series in Hervig et al. (2019) was conducted by averaging the H<sub>2</sub>O concentration between 80-85 km, where the water vapour concentration is largely influenced by the microphysical processes of noctilucent clouds (NLCs), including the freeze-drying effect. Due to the coarse vertical resolution of satellite observations (between 1.5 km and 3 km), there is an increased risk of bias, especially when averaging the H<sub>2</sub>O concentration at NLC altitudes. Therefore, they recommended further verification of these results by using microphysical ice models with high vertical resolution.

As mentioned in the objectives of this thesis, we utilised our LIMA/MIMAS model simulations to mainly investigate the solar cycle response in the NLCs and the background atmosphere on centennial timescales. The next three chapters are the summary of research articles, which answer the questions raised in the objectives of this thesis. In the following chapter, we discuss the underlying mechanism behind the H<sub>2</sub>O solar cycle response at NLC altitudes with a particular focus on the recent 2 solar cycles (solar cycles 23 and 24) to investigate the missing response of H<sub>2</sub>O discussed in Hervig et al. (2019).



## Chapter 4

# Solar cycle response of water vapour and noctilucent clouds

Summary of:

Ashique Vellalassery et al. (2023). “Greenhouse gas effects on the solar cycle response of water vapour and noctilucent clouds”. In: *Annales Geophysicae* 41.2, pp. 289–300. ISSN: 14320576. DOI: 10.5194/angeo-41-289-2023

Water vapour (H<sub>2</sub>O) is a critical minor component in the mesosphere, serving as the main source of chemically active hydrogen radicals. These radicals play a major role in the chemical dynamics of other minor chemical components (Brasseur and Solomon, 2005; Hartogh et al., 2010). Understanding the effects of the solar cycle on H<sub>2</sub>O is even more complicated at NLC altitudes due to the interaction between NLCs and background H<sub>2</sub>O. In Vellalassery et al. (2023), the responses of water vapour and NLCs to the solar cycle are investigated using the MIMAS model. The solar cycle influences the H<sub>2</sub>O concentration in the upper mesosphere in two main ways: through photolysis and, at the time and place of NLC formation, indirectly through temperature changes. LIMA and MIMAS use daily Ly $\alpha$  flux data obtained from the Laboratory for Atmospheric and Space Physics (LASP) Interactive Solar Irradiance Data Centre (LISIRD) to represent solar activity from 1961 to 2021, as described in the study by Machol et al. (2019). Changes in the Ly $\alpha$  input (and other spectral bands) in LIMA lead to variations in atmospheric temperature. On the other hand, fluctuations in the Ly $\alpha$  input in MIMAS lead to changes in the photolysis of H<sub>2</sub>O (see Figure 2.1). This allows for studying the effects of temperature changes and photolysis on H<sub>2</sub>O separately. This separation is achieved by performing model simulations with constant and varying Ly $\alpha$  inputs in MIMAS and LIMA ( see Table 2.1).

The main aim of this study is to answer the following questions: (1) how does the formation of NLCs and increasing greenhouse gases influence the H<sub>2</sub>O profile and its response to the solar cycle? (2) How do the temperature and photolysis changes induced by the solar cycle affect H<sub>2</sub>O and NLCs? (3) Why is the response of water vapour to the solar cycle nearly absent in the satellite observations reported by Hervig et al. (2019) after 2005?

This study focused mainly on two recent solar cycles from 1992 to 2018 on the core NLC period, i.e., July at latitude  $68 \pm 3^\circ\text{N}$ . Figure 4.1 illustrates the time series of Ly $\alpha$ , CO<sub>2</sub>, and CH<sub>4</sub> from 1992–2018. It shows that the intensity of Ly $\alpha$  radiation has

decreased in the later period compared to the earlier period. At the same time, the concentrations of greenhouse gases (GHGs) have increased in the later period. The amplitude of the  $\text{Ly}\alpha$  variation is weaker during the late period ( $1.14 \times 10^{11}$  [phot.  $\text{cm}^{-2} \text{s}^{-1}$ ] per solar cycle) than during the early period ( $1.85 \times 10^{11}$  [phot.  $\text{cm}^{-2} \text{s}^{-1}$ ] per solar cycle). This means that the intensity of  $\text{Ly}\alpha$  during the late solar maximum is reduced by 40% compared to the early cycle.

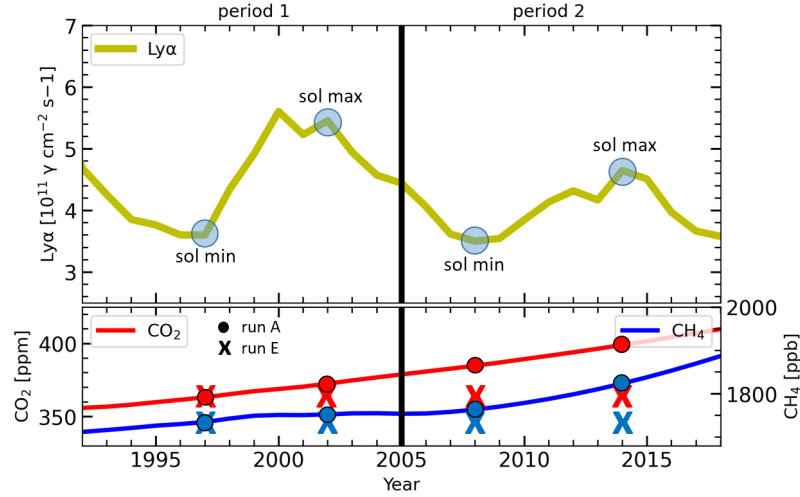


FIGURE 4.1: Time series of solar  $\text{Ly}\alpha$ ,  $\text{CO}_2$ , and  $\text{CH}_4$  for 1992–2018. The corresponding  $\text{Ly}\alpha$ ,  $\text{CO}_2$ , and  $\text{CH}_4$  values for the solar cycle maximum and minimum years used for this study are marked. The  $\text{CO}_2$  and  $\text{CH}_4$  values for run A are represented by dots, and for run E, they are represented by crosses. The study period is divided into period 1 as early (1992–2005) and period 2 as late (2005–2018). Figure taken from Vellalassery et al. (2023), Fig. 2.

First, the agreement of the model with the satellite observations is evaluated by comparing the anomaly of ice water content (IWC) derived from the model with the satellite data (see Figure 4.2). The IWC anomalies are calculated using the following method:

$$\text{IWC}_{\text{anom}} = 100\% \cdot \frac{\overline{\text{IWC}}_{\text{july}} - \overline{\text{IWC}}_{1981-2018}}{\overline{\text{IWC}}_{1981-2018}} \quad (4.1)$$

$\overline{\text{IWC}}_{\text{july}}$  represents monthly zonal averages at  $68^\circ\text{N}$ , and  $\overline{\text{IWC}}_{1981-2018}$  are the averages of  $\overline{\text{IWC}}_{\text{july}}$  over the years 1981–2018. The satellite observations of IWC anomalies come from the Solar Backscatter Ultraviolet (SBUV), Halogen Occultation Experiment (HALOE), Cloud Imaging and Particle Size (CIPS), and Solar Occultation For Ice Experiment (SOFIE) instruments. We refer to Hervig et al. (2019) for more details on the satellite datasets.

In Figure 4.2, an anti-correlation exists between the MIMAS IWC anomalies and the  $\text{Ly}\alpha$  flux throughout the period (1981–2018), with a weaker response observed in the later years which can be attributed to reduced solar maximum intensity during the later solar cycle. Among satellite observations, SBUV measurements also show an anti-correlation with the  $\text{Ly}\alpha$  flux until 2005, after which the response weakens, consistent with MIMAS. The solar cycle-induced IWC anomaly observed in HALOE

also agrees well with the MIMAS IWC anomaly. However, the IWC anomalies observed in CIPS and SOFIE after 2005 do not show a clear response to the solar cycle. In addition, the year-to-year IWC variation in CIPS and SOFIE is larger than the modulation observed during a solar cycle. Previous studies (Lübken et al., 2009; Berger and Lübken, 2015; Lübken et al., 2018; Lübken et al., 2021) have shown a robust agreement between the NLC parameters derived from MIMAS simulations and the parameters obtained from satellite observations.

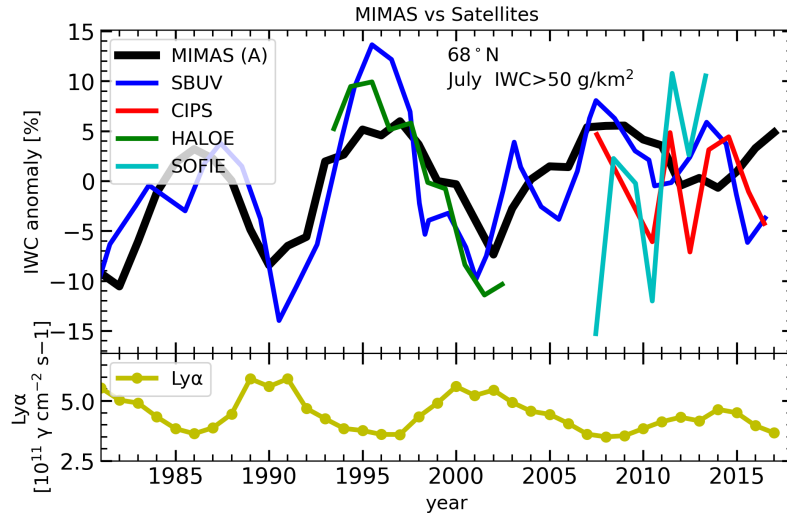


FIGURE 4.2: Time series of anomalies of the mean ice water content (IWC) in July at  $68^\circ\text{N}$  from model and satellite data, based on Hervig et al. (2019). The anomalies for each data set are calculated as a deviation from their long-term mean. To reduce the year-to-year variability, the time series of SBUV and HALOE are smoothed using a moving average method with a window size of 3. The modulation of the  $\text{Ly}\alpha$  solar cycle is shown in the bottom panel. Figure taken from Vellalassery et al. (2023), Fig. 3.

Additional model simulations were performed to determine the separate effects of solar cycle-induced temperature and photolysis variations on water vapour, namely runs E, F, and G, as described in Section 2.3 (see Table 2.1). In run F, the  $\text{H}_2\text{O}$  concentration is only affected by the temperature change caused by the solar cycle. In run G, only the photolysis variations of the solar cycle affect the  $\text{H}_2\text{O}$  concentration, and in run E, both effects are present. All these simulations are performed with constant greenhouse gas concentrations ( $\text{CO}_2$  and  $\text{CH}_4$ ) to mitigate their influence on the temperature and  $\text{H}_2\text{O}$  profiles.

Run F (Figure 4.3a) shows a positive temperature difference (red line) between solar maximum and minimum, which indicates that the temperature during the solar maximum is higher than during the solar minimum over the entire altitude range (79–97 km). The temperature difference is between 0.5 and 1.7 K, with the peak occurring at 95 km. During the solar maximum, the increased solar radiation leads to increased absorption in the mesosphere and lower thermosphere (MLT) by molecular oxygen and water vapour, which increases the temperature of the surrounding atmosphere. As altitude decreases, the temperature differences become smaller, as the intensity of solar radiation decreases due to absorption by molecular oxygen and water vapour. The difference in the  $\text{H}_2\text{O}$  profiles is different for the model run with NLCs (blue line) and without NLCs (yellow line). Without NLCs, the difference

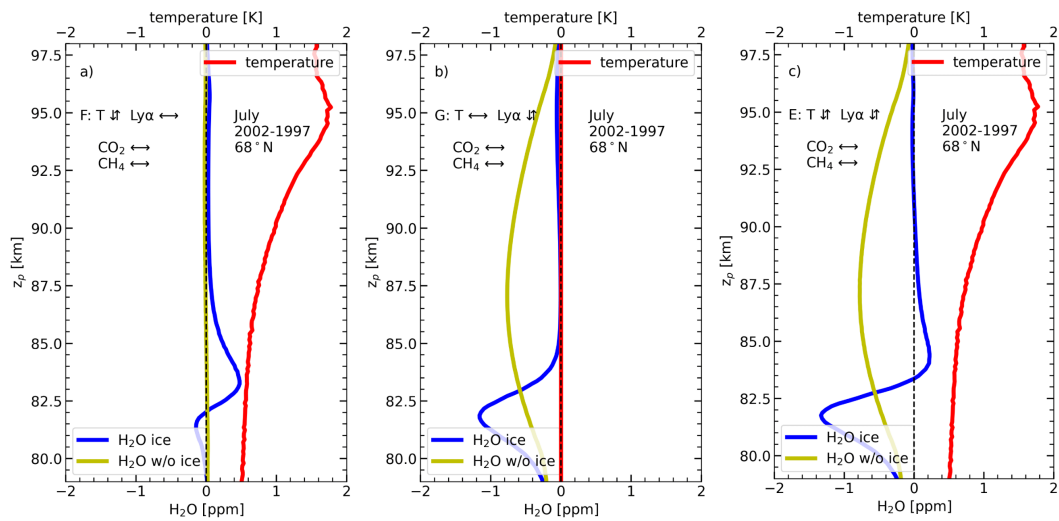


FIGURE 4.3: The  $\text{H}_2\text{O}$  and temperature profile difference between solar maximum (2002) and minimum (1997) for July mean. The blue and yellow lines represent NLC and non-NLC conditions.  $\text{CO}_2$  and  $\text{CH}_4$  values are constant in all cases, corresponding to 1997. (a) Run F: only temperature change effects on  $\text{H}_2\text{O}$ . (b) Run G: only photolysis change effect on  $\text{H}_2\text{O}$ . (c) Run E: temperature change and photolysis change effects on  $\text{H}_2\text{O}$ . Figure taken from Vellalassery et al. (2023), Fig. 5.

remains close to zero at all heights, which indicates that without NLCs, the temperature changes alone have very little or no effect on the  $\text{H}_2\text{O}$  profile. With NLCs, the difference in the  $\text{H}_2\text{O}$  profile is positive between 82–87 km altitudes and slightly negative between 79–82 km. This is because, during the solar maximum, the increased warming of the background atmosphere leads to a decrease in the rate of ice formation. When the ice formation rate decreases, the water vapour consumption from the background decreases. Consequently, more  $\text{H}_2\text{O}$  is retained in the background during solar maximum when compared to solar minimum. This leads to a slightly positive response at altitudes above 83 km, where NLCs form. Below this altitude, the slightly negative response is due to the reduced ice formation during the solar maximum. This leads to a reduced release of  $\text{H}_2\text{O}$  at the altitudes of ice sublimation.

In model run G (Figure 4.3b), we consider only the effect of solar-cycle-induced  $\text{Ly}\alpha$  variation on water vapour photolysis. The background temperature is held constant. Without NLCs (yellow line), the difference in the  $\text{H}_2\text{O}$  profile is negative at all altitudes, indicating a decrease in background  $\text{H}_2\text{O}$  during solar maximum due to increased photolysis. With NLCs (blue line), the difference in  $\text{H}_2\text{O}$  profile is essentially negative at ice sublimation altitudes (below  $\sim 83$  km) and negligible at higher altitudes (above  $\sim 83$  km). This is due to the redistribution of the  $\text{H}_2\text{O}$  during NLC formation (freeze-drying). During solar maximum, the amount of background  $\text{H}_2\text{O}$  available for ice formation is reduced due to increased photolysis. Previous studies (Zahn et al., 2004; Lübken et al., 2009) also suggested that freeze-drying significantly reduces the potential effects of  $\text{Ly}\alpha$  photolysis on  $\text{H}_2\text{O}$  above 82 km, where ice formation occurs. On the other hand, the effect increases at altitudes of 80–82 km, where ice particles sublimate.

Figure 4.3c shows a combination of both effects, namely the solar cycle-induced temperature change and the photolysis effects on H<sub>2</sub>O. Without NLCs (yellow line), the H<sub>2</sub>O profiles show a negative difference at all altitudes, indicating a decrease in the H<sub>2</sub>O profile during solar maximum across all altitudes, primarily due to photolysis. With NLCs (blue line), the combined influence of temperature and photolysis leads to a slightly positive response to water vapour in the ice formation region (83-89 km) and a negative response in the ice sublimation region (80-83 km). The slight positive response is attributed to temperature variations, while the negative response is mainly due to photolysis fluctuations during the solar cycle.

The results suggest that the water vapour response to the solar cycle is affected by freeze-drying under NLC conditions. At altitudes where NLCs form, it is possible to observe positive correlations between water vapour and Ly $\alpha$ . Without NLCs, H<sub>2</sub>O only shows a negative response to the solar cycle. As far as we know, this is the first finding of a positive correlation of water vapour to Ly $\alpha$  variations in the MLT region due to microphysical processes. For a long time, it has been generally assumed that water vapour at mesopause altitudes has only an inverse relationship to the solar cycle (e.g. Sonnemann and Grygalashvily, 2005, and references therein).

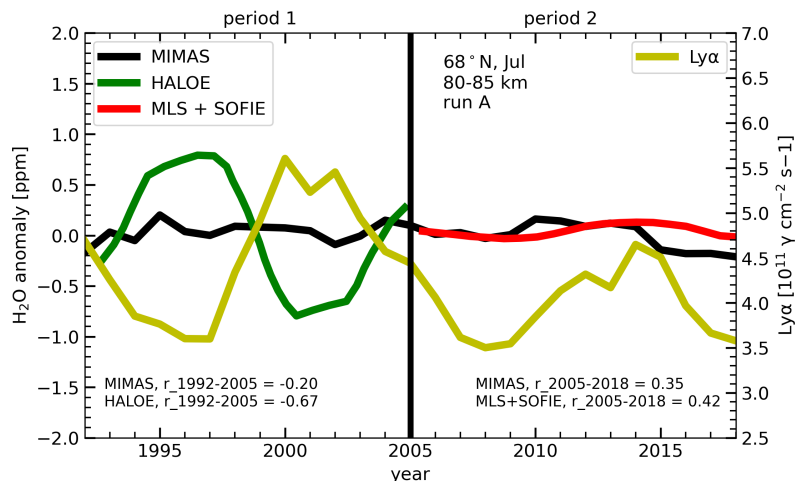


FIGURE 4.4: Time series of Ly $\alpha$  and H<sub>2</sub>O anomalies as monthly averages for July at 68°N for the altitude range of 80–85 km from MIMAS run A and satellites (HALOE and the composite data from MLS and SOFIE). Satellite observations are according to Hervig et al. (2019). The H<sub>2</sub>O–Ly $\alpha$  correlation is calculated for the early and late periods (see inset). Figure taken from Vellalassery et al. (2023), Fig. 8.

The response of H<sub>2</sub>O to the solar cycle, which has been missing since 2005 (Hervig et al., 2019), is investigated with MIMAS. We have investigated how well our model is in agreement with the satellite observations of water vapour that are discussed in Hervig et al. (2019). For the comparison, we applied the geometry of the satellite observations in the model, i.e. the response of H<sub>2</sub>O was averaged over an altitude range of 80-85 km, as shown in Figure 4.4. The satellite observations from HALOE showed a strong anti-correlation with the solar cycle in the early period. At the same time, the model exhibited a very small response in both the early and late periods. In the early period, MIMAS showed no clear inverse relationship between H<sub>2</sub>O and the solar cycle. However, there was a slightly positive correlation in the late period, consistent with the SOFIE and MLS satellite observations.

Figure 4.5 shows that the  $\text{H}_2\text{O}$  response to the solar cycle is not completely absent in the late period. In MIMAS, it becomes negligible when averaged over an altitude of 80-85 km. In the altitude range of 80-85 km (shaded area in Figure 4.4), the positive and negative reactions of  $\text{H}_2\text{O}$  are almost equal and symmetrical. Therefore, averaging these values over this height range reduces the overall response of the model, as the positive and negative responses cancel each other out. In summary, The apparent disappearance of the solar cycle modulation in the satellite observations is probably due to averaging over altitude ranges (80-85 km) where both a positive and a negative response occur. Unfortunately, we can only speculate about the disagreement between HALOE and MIMAS. However, what we saw from our model simulation is that the solar cycle response in the vertically averaged data can be increased if we change the altitude of averaging. This result suggests that a simple averaging of  $\text{H}_2\text{O}$  values at NLC altitudes, including positive and negative variations, cannot fully explain the relationship between  $\text{H}_2\text{O}$  concentrations and the solar cycle.

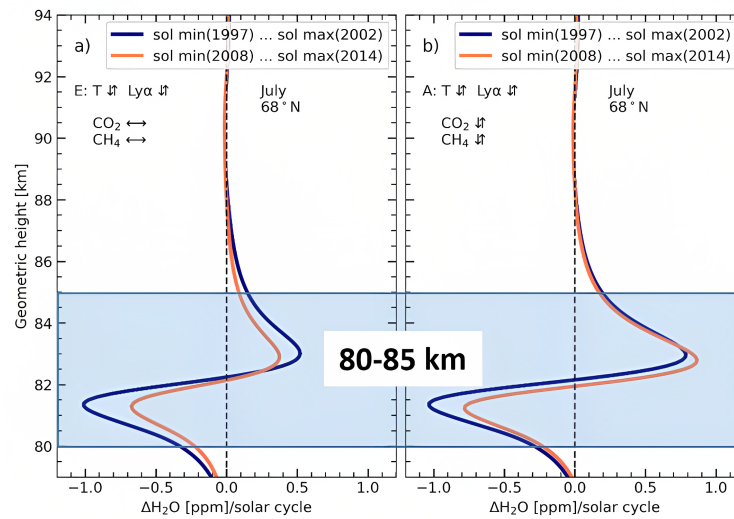


FIGURE 4.5: The  $\text{H}_2\text{O}$  response to the absolute  $\text{Ly}\alpha$  variations of the solar cycle in July at  $68^\circ\text{N}$  in the years between solar minimum and maximum is shown in geometric heights for both the early period (1997-2002) and the late period (2008-2014). The shaded area represents the altitude range used to calculate an average response to the solar cycle. Panels (a) and (b) show the results of two MIMAS model runs: (a) run E with constant  $\text{CO}_2$  and  $\text{CH}_4$ , and (b) run A with varying  $\text{CO}_2$  and  $\text{CH}_4$ . Figure taken from Vellalassery et al. (2023), Fig. 9.

The effects of increasing GHGs in the later period are analyzed by comparing the model simulations with increasing and constant greenhouse gases. In run with increasing GHGs (run A), water vapour response to  $\text{Ly}\alpha$  increased in the later period compared to the early period (see Figure 4.1b). This is due to increased  $\text{CO}_2$  and  $\text{CH}_4$ , which leads to a decrease in temperature and an increase in water vapour, intensifying microphysical processes and freeze-drying. However, relying solely on data from the last two solar cycles may not provide a complete understanding of the long-term consequences of rising greenhouse gases (GHGs). To gain a comprehensive insight into the impact of GHGs over time, it's essential to analyse long-term data sets. Therefore, we studied the long-term evolution of NLCs and their response to the solar cycle for a longer period (1849-2019) with and without increasing GHGs, which is discussed in the next chapter.

## Chapter 5

# Long-term trends in noctilucent clouds response to solar cycle variations

Summary of:

Ashique Vellalassery et al. (2024). "Long-Term Evolution in Noctilucent Clouds' Response to the Solar Cycle: A Model-Based Study". In: *Atmosphere* 15.1. ISSN: 20734433. DOI: 10.3390/atmos15010088

There are studies that have used the LIMA/MIMAS model to investigate long-term trends in NLCs and the effects of increases in greenhouse gases (CO<sub>2</sub> and CH<sub>4</sub>) from 1871 to 2008 (Lübken et al., 2018; Lübken et al., 2021). Those study's results revealed that the time series of some of the ice parameters fluctuates significantly with the solar cycle (see Figure 3 in Lübken et al., 2018). Given the aim of those studies to explore long-term trends in NLCs, the influence of solar cycle variations on NLCs was excluded by averaging over half a solar cycle (Lübken et al., 2021). The available observational data on NLC trends are still quite limited, and there is little knowledge about long-term trends and fluctuations in the background atmosphere at NLC altitudes (Thomas, 2003; Lübken et al., 2018; Berger and Zahn, 2002, Nedoluha et al., 2017). Model simulations are a valuable tool for better understanding the changes in NLC properties and the surrounding atmosphere (Hervig et al., 2015).

In this study (Vellalassery et al., 2024), long-term simulations of NLCs were carried out with the MIMAS model for the period from 1849 to 2019, with the aim to investigate the impact of 11-year solar cycle variations on NLC characteristics. Our analysis is based on model simulations previously used in studies by Lübken et al. (2018) and Lübken et al. (2021). Three model runs are carried out for this study, namely Run A, B and C. In run A, both CO<sub>2</sub> and CH<sub>4</sub> (H<sub>2</sub>O) increase. In run B, only the CO<sub>2</sub> concentration increases, while the CH<sub>4</sub> concentration remains constant. In run C, the CH<sub>4</sub> concentration increases while the CO<sub>2</sub> concentration remains constant (see section 2.3 for more details). Unfortunately, little is known about the long-term changes in dynamic and compositional properties of the summer mesopause region. As the consideration of long-term changes in dynamics is highly speculative, the model simulations are carried out using a specific dynamic scenario from a representative year 1976 for the entire period (1849 to 2019).

The main questions addressed in this paper are: (1) How do the background temperature and water vapour respond to the solar cycle, and what are the trends in their response? (2) What are the long-term trends in NLC properties, and how do solar cycle modulations affect them? (3) What effect does the long-term increase in greenhouse gases have on the response of NLC properties to the solar cycle?

We analysed the effects of increasing CO<sub>2</sub> and solar cycle fluctuations on the time series of vertical temperature profiles from 1849 to 2019. The temperature profiles have shifted downwards over time with increasing CO<sub>2</sub>. This is due to the atmospheric shrinking effect. Simultaneously, the influence of the solar cycle is identified in the time series of vertical temperature profiles with a clear 11-year pattern. During the solar maximum, increased solar irradiance in the MLT region results in increased absorption of solar radiation by molecular oxygen and water vapour, heating the background atmosphere. The temperature differences of 0.5 K - 2 K observed between the solar maximum and minimum at NLC altitudes depend on the intensity of the solar cycle and the altitude (see Fig. 5 in Vellalassery et al., 2023).

The time series of the water vapour profiles for MIMAS runs A and C with and without NLCs are shown in Figure 5.1. Without NLCs (see Figures 5.1a and 5.1b), the water vapour concentration increases progressively over time at all altitudes. This trend is due to the increased CH<sub>4</sub> content, which leads to an increased production of H<sub>2</sub>O molecules due to oxidation of CH<sub>4</sub>. In addition, the effects of the solar cycle can be seen in periodic maxima and minima in the time series of the H<sub>2</sub>O profiles, which recur every 11 years. During solar maximum, there is a decrease in the water vapour concentration at all altitudes, which is due to the increased photolysis due to the increased Ly $\alpha$  flux.

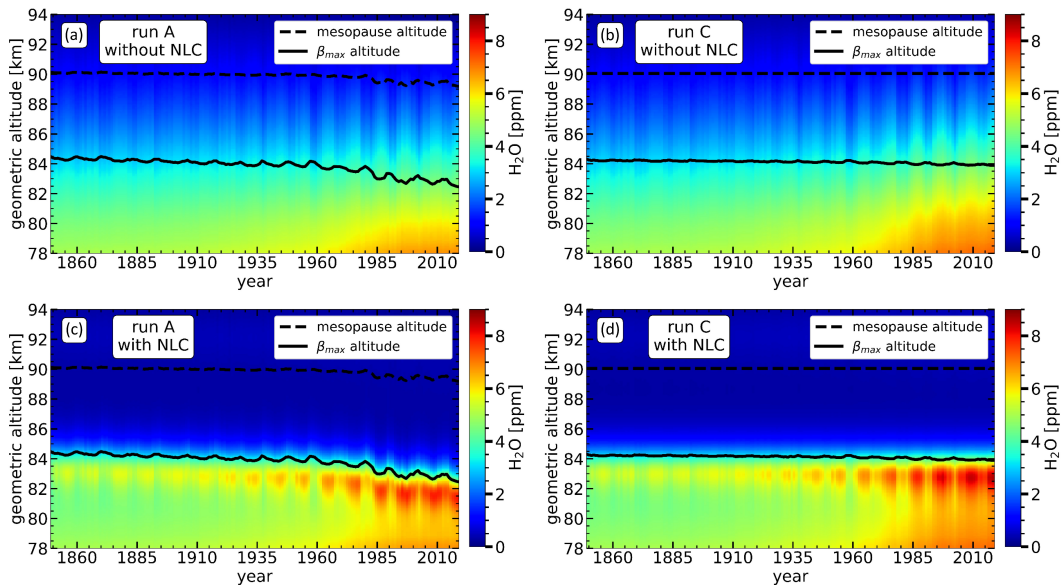


FIGURE 5.1: Time series of water vapour concentration as a function of geometric altitude, zonally (69°N) and monthly (July) averaged for (a) Run A without NLC, (b) Run C without NLC, (c) Run A with NLC, and (d) Run C with NLC. Figure taken from Vellalassery et al. (2024), Fig. 3.

Comparing the figures with and without NLC (Fig. 5.1, upper and lower panels), it is evident that the H<sub>2</sub>O profile with NLCs differs significantly from that without

NLCs. At altitudes where NLCs are formed ( $> \sim 83 - 85$  km), there is a reduction in  $\text{H}_2\text{O}$  concentration due to the consumption of  $\text{H}_2\text{O}$  during ice particle formation, commonly referred to as the "freeze-drying effect". Consequently, the highest  $\text{H}_2\text{O}$  concentrations occur at altitudes where NLC ice particles sublimate, approximately 1 km below the altitude corresponding to the maximum backscatter coefficient ( $\beta_{\text{max}}$ , NLC altitude) indicated by the solid black line. In addition, the  $\text{H}_2\text{O}$  profiles shown in Run A show a gradual downward shift in geometrical altitudes over time compared to Run C, attributed to atmospheric shrinking caused by increasing  $\text{CO}_2$  levels.

The study investigated the long-term trends in the vertical profiles of NLC properties under different atmospheric greenhouse gas conditions (runs A, B, and C). The study shows that regardless of the altitude where the highest concentration of ice particles occurs, the maximum brightness of NLC (represented by  $\beta_{\text{max}}$ ) aligns with the altitude where the largest particle radius is found. This occurs because the increase in the backscatter cross-section is roughly proportional to the radius to the power of six ( $r^6$ ). The long-term trends indicate an increase in the radius of ice particles and brightness of NLC, primarily attributed to rising  $\text{H}_2\text{O}$  levels. We noted the impact of the 11-year solar cycle on the vertical distribution of NLC properties. During the solar maximum, decreased water vapour due to increased photolysis and higher temperatures result in reduced ice formation. Consequently, smaller ice particles form, leading to lower brightness during the solar maximum compared to the years of solar minimum. This is observed across all altitudes, with the most significant effects occurring at the  $\beta_{\text{max}}$  altitude.

Next, we examined the trends in how various NLC properties respond to the 11-year solar cycle. Our analysis focused solely on the midpoint of the summer season, specifically July. Additionally, we implemented a threshold for NLC brightness ( $\beta_{\text{lim}} = 0.05$ ) to filter out non-NLC events while still capturing smaller NLC occurrences. The time series of NLC altitude, also known as the  $\beta_{\text{max}}$  altitude, is depicted in Figure 5.2a, while the lower panel of the same figure displays the time series of  $\text{Ly}\alpha$ . In runs A and B, the altitude of NLC decreases due to  $\text{CO}_2$ -induced atmospheric shrinking. Conversely, in run C, where only  $\text{H}_2\text{O}$  increases, the NLC altitude remains nearly constant (Lübken et al., 2018; Lübken et al., 2021).

To investigate trends in the variation of NLC height with the solar cycle, we computed the response of NLC height to a unit change in  $\text{Ly}\alpha$  for each solar cycle. This involved calculating the absolute difference in NLC height between the solar maximum and minimum and subsequently dividing it by the absolute  $\text{Ly}\alpha$  difference between the corresponding solar maximum and minimum. In Figure 5.2b, the time series illustrates the NLC altitude response for 15 solar cycles spanning from 1855 to 2019. Before the 19th solar cycle (1954-1964), the NLC altitude response exhibited a relatively gradual and slow increase. However, following the 19th solar cycle, there was a noticeable acceleration in the NLC altitude response. Post-1960, various properties of NLCs, including brightness, radius, and IWC, experienced enhancements due to the accelerated rise in greenhouse gas concentrations (Lübken et al., 2018; Lübken et al., 2021).

We also analyzed the trends of how the maximum NLC brightness ( $\beta_{\text{lim}}$ ), ice water content (IWC), and the occurrence of NLC respond to the solar cycle. Figure 5.3a shows the time series of the solar cycle response of maximum brightness for runs A, B, and C. The maximum brightness negatively correlates with the solar cycle variations, with its intensity gradually increasing over time in all runs. However,

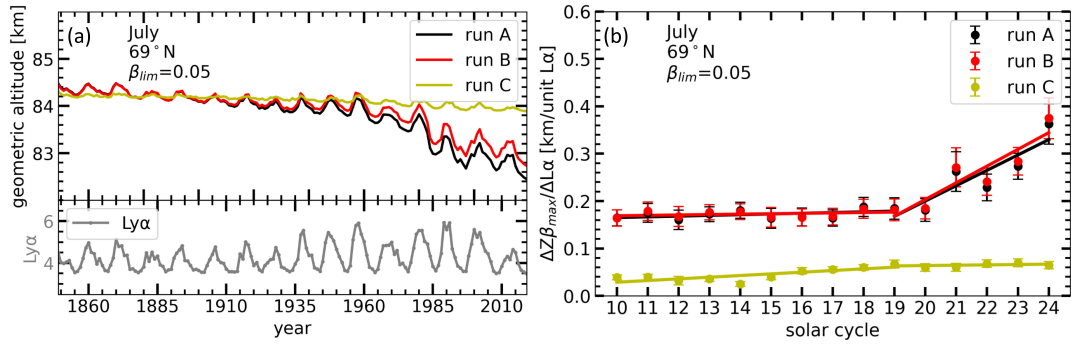


FIGURE 5.2: (a) Time series of NLC altitudes (averaged for July and zonally at  $69^\circ\text{N}$ ) from 1849 to 2019. The results from three runs (A, B, and C) are shown in the figure (see insert). The lower panel shows the time series of the solar  $\text{Ly}\alpha$  flux (unit:  $10^{11} \gamma \text{ cm}^{-2} \text{ s}^{-2}$ ) averaged for July. (b) Response of NLC altitude to the unit change in solar  $\text{Ly}\alpha$  during solar cycles between 1855 to 2019 (For example, solar cycle 10 corresponds to 1855-1867, while solar cycle 24 represents 2008-2019). The three runs, A, B, and C, are shown (see insert), showing linear regression fits. The error bars represent the standard error of the mean for the respective solar cycle years. Figure taken from Vellalassery et al. (2024), Fig. 6.

this increase is more pronounced in runs A and C than in run B. This suggests that the main factor contributing to the enhanced response of NLC brightness to the solar cycle is the increase in  $\text{H}_2\text{O}$ .

Figure 5.3b shows an increasing trend in the response of IWC to the solar cycle in all runs. The results suggest that the increased response of the IWC to the solar cycle is due to both temperature variations and increasing  $\text{H}_2\text{O}$ . However, the increased  $\text{H}_2\text{O}$  has a greater influence on the increased response of IWC than those of  $\text{CO}_2$  and temperature. Figure 5.3c presents the trends in the solar cycle response of the NLC occurrence rate. The occurrence rate of NLC is calculated as follows: For July in each year, the total number of latitude/longitude fields (referred to as "events",  $N_{\text{max}}$ ) is determined by latitude fields (6), longitude fields (120), and time windows of 6 hours each ( $31 \text{ days} \times 4 \text{ per day} = 124\text{-time steps}$ ), resulting in a total number of 89,280 events ( $N_{\text{max}}$ ). Whenever an ice layer occurs (applying a given threshold in NLC brightness ( $\beta_{\text{lim}} = 0.05$ )) in a given latitude/longitude bin and time segment in MIMAS, we call this an "NLC event". The NLC occurrence rate is calculated by dividing the number of NLC events by the total number of events ( $N_{\text{max}}$ ).

The occurrence rate of NLC showed a negative response to the solar cycle. Figure 5.3c shows that the response of the NLC occurrence to the solar cycle is more pronounced with temperature changes (runs A and B) than with a constant temperature (runs C). This suggests that the temperature variations associated with the solar cycle have a significant influence on the frequency of NLC occurrence. This is a consequence of the transition from NLC to non-NLC events (from supersaturation to subsaturation), primarily determined by temperature changes, while water vapour plays a secondary role (Berger and Zahn, 2002). After the 19th solar cycle, the NLC occurrence rate in runs A and C either remains constant or decreases slightly. This is due to the accelerated increase in carbon dioxide ( $\text{CO}_2$ ), which leads to a cooling of the upper mesosphere, and the increase in methane ( $\text{CH}_4$ ), which leads to increased water vapour concentrations. Consequently, more events shift to NLC events with

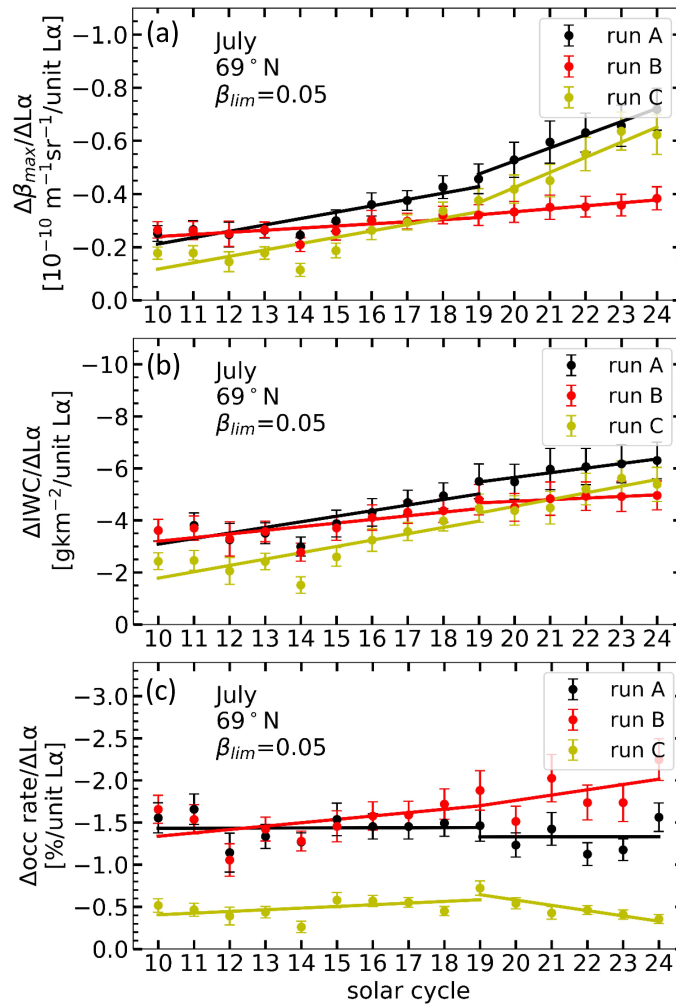


FIGURE 5.3: NLC properties response to a unit change in solar  $\text{Ly}\alpha$  at  $69^\circ\text{N}$  during solar cycles between 1855 and 2019. Results are shown for three runs: A, B, and C (see insert). Error bars indicate the standard error of the mean during respective solar cycle years. The figures are shown for (a) Maximum brightness, (b) IWC, and (c) NLC occurrence rate, with a threshold value of  $\beta_{\text{lim}} = 0.05$  applied. Figure taken from Vellalassery et al. (2024), Fig. 7.

high saturation ratios ( $S$ ). As a result, solar cycle-induced variations in  $\text{H}_2\text{O}$  and temperature have minimal impact on the transition of NLC events from supersaturation to subsaturation, as saturation ratios are already high ( $S \gg 1$ ). Therefore, the response of the NLC occurrence rate decreases from the 19th solar cycle onwards.

The response of NLC properties to the solar cycle varies with latitude. NLC height, maximum brightness, and ice water content showed stronger responses and similar trends at high and Arctic latitudes. The occurrence of NLC shows a smaller response to the solar cycle at high and Arctic latitudes but a stronger one at mid-latitudes. The water vapour saturation ratio ( $S$ ) is higher at high and Arctic latitudes, while it is lower at mid-latitudes due to warmer temperatures and lower water vapour concentrations. Therefore, temperature and water vapour fluctuations during the solar cycle have a stronger influence on the value of  $S$  and, consequently, on the occurrence of NLC at mid-latitudes than at high and Arctic latitudes.

We found that increases in greenhouse gas (GHG) concentrations are primarily responsible for the enhanced response of noctilucent clouds to the solar cycle. This illustrates the impact of increasing anthropogenic emissions on temperature and water vapour concentrations in the upper atmosphere. These results indicate that the effects of climate change are particularly more noticeable in the upper mesosphere, which can be directly observed from Earth through NLCs. With this increasing water vapour trend in the mesosphere due to the increasing CH<sub>4</sub>, there will be a further increase in NLCs in the future, which could lead to increasing absorption of solar radiation that can affect the upper mesosphere photochemistry. To investigate this, we have recently performed MIMAS simulations for the future (up to the year 2100), considering only the CH<sub>4</sub> increase, as the CH<sub>4</sub> increase (water vapour) is the main reason for the increasing optical parameters such as brightness and extinction. The next chapter examines the absorption of solar radiation due to future enhancements in NLCs.

## Chapter 6

# Absorption of solar radiation by noctilucent clouds in a changing climate

Summary of:

Franz Josef Lübken et al. (2024). "Absorption of Solar Radiation by Noctilucent Clouds in a Changing Climate". In: *Geophysical Research Letters* 51.8. ISSN: 0094-8276. DOI: 10.1029/2023GL107334

As mentioned in the previous chapter, increased methane (CH<sub>4</sub>) emissions presumably will increase water vapour concentration in the mesosphere. This leads to an enhancement in NLCs, which absorb more solar radiation in the future. Recently, Yu et al. (2023) published findings on the future development of NLC; however, they used a zero-dimensional model for NLC and no extinction was calculated. In this work, we studied the extinction of solar radiation by NLCs at various wavelengths in a future climate scenario with increasing methane. We used LIMA/MIMAS model runs for 1950-2100 with only methane increase. More details on the model and numerical experiments are discussed in Chapter 2 and in previous publications (Lübken et al., 2018; Lübken et al., 2021). For this study, we used the background conditions of a representative year for all years, i.e. the dynamic forcing of the upper mesosphere/lower thermosphere is constant for all years.

In MIMAS, the formation of ice particles is determined by analysing the evolution of 40 million dust/ice particles, resulting in a full-size distribution. This size distribution, representing the number of particles within a given bin, is then used to calculate the extinction coefficients. In some models, only the mean radius of the ice particles is available, so a theoretical size distribution has to be assumed. This leads to errors in the assumed distribution, which can lead to significant errors in calculating the extinction coefficients, as the optical properties vary approximately with  $r^6$  ( $r$  = radius). In previous studies (Lübken et al., 2018; Lübken et al., 2021), we have shown that the increase in optical parameters such as brightness and extinction is primarily due to increased H<sub>2</sub>O, while a decrease in temperature (due to increased carbon dioxide levels) has only a minimal effect.

The future increase in methane concentrations (Figure 2.5) is based on the IPCC AR4, focussing on the RCP 8.5 scenario described by Riahi et al. (2011). Due to computational limitations, we used the results of the MIMAS model from selected years between 1950 and 2100, focusing only on the NLC core season in July, as in

previous studies. We have compared the results of LIMA and MIMAS with ground-based and satellite-based observations and found excellent agreement (e.g. Schmidt et al., 2018; Lübken et al., 2018; Lübken et al., 2021; Vellalassery et al., 2023; and references therein). Schmidt et al. (2018) carried out a comprehensive comparison of lidar and satellite observations with LIMA/MIMAS data. Their results indicate a slight tendency to underestimate the radii of the model. We have therefore adjusted all radii in the model by a factor of 1.35.

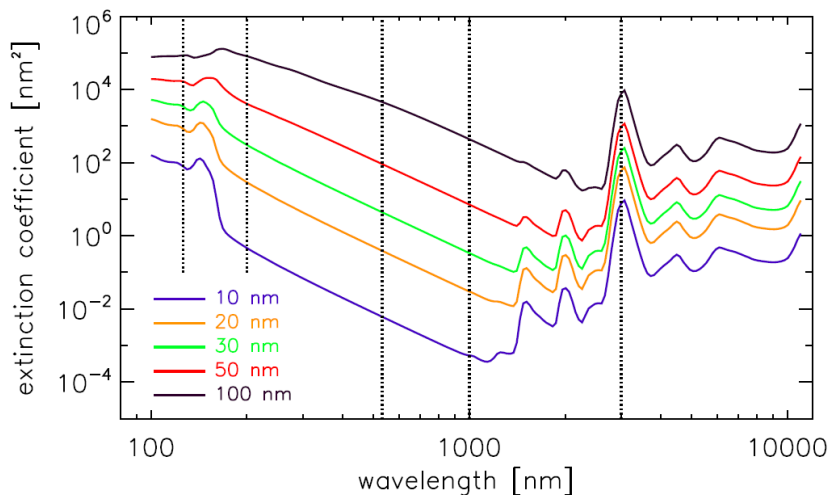


FIGURE 6.1: Extinction coefficients as a function of wavelength for (mono-dispers) particle radii as given in the insert (in nm, various colours). The vertical lines mark wavelengths where we have calculated extinctions by the NLC layer. Figure taken from Lübken et al. (2024), Fig. 2.

Figure 6.1 shows the extinction coefficients as a function of wavelength for monodisperse particles with specific radii. The extinction coefficient (“cross-section”)  $\sigma(r, \lambda)$  (units:  $\text{m}^2$ ) is a function of particle radius  $r$  and wavelength  $\lambda$ . The optical depth  $d\tau$  for a given wavelength  $\lambda$  traversing a layer at height  $z$  with a geometrical thickness  $dz$ :

$$d\tau(z, r, \lambda) = \sigma(r, \lambda) \cdot dz \cdot dN(z, r, dr)$$

where  $dN(z, r, dr)$  is the number density of particles at height  $z$  with radius between  $r$  and  $r + dr$ . The total optical depth  $\tau_\lambda$  is determined by integrating over all radii. The amount of solar light with wavelength  $\lambda$  passing the layer (relative to the incoming intensity) is  $\exp(-\tau)$ , and the relative attenuation is  $a = 100 \cdot (1 - e^{-\tau})$  (in %).

In MIMAS, the backscatter coefficients and optical depths are calculated for every box, that is, at all altitude layers, at all latitudes/longitudes, and at all time steps. The total optical depth is then determined by summing all these boxes. Figure 6.1 shows that the extinction coefficient varies as  $\lambda^{-4}$  for a given radius and approximately as  $r^6$  for a given wavelength over a significant range of the visible and infrared spectrum (approximately between 200 and 1000 nm). The absorption of solar radiation generally decreases with increasing wavelength. However, this behaviour does not apply for wavelengths above 1000-2000 nm and particle radii below around 200 nm.

The resonances with a major peak at  $\sim 3000$  nm are due to the vibrational excitation of OH.

We compared the frequency of occurrence of the maximum backscatter coefficients ( $\beta_{\max}$ ) of MIMAS with the observations of  $\beta_{\max}$  from the ALOMAR Rayleigh-Mie-Raman (RMR) lidar at  $69^\circ\text{N}$  (both for the month of July only) (Figure 3 in Lübken et al., 2024). The comparison showed that the relative distribution of the  $\beta_{\max}$  values from the observations agrees with those of the model. This agreement suggests that the distributions of particle size and number density in LIMA/MIMAS are realistic, which also applies to the extinction coefficients and attenuations.

We then analysed the frequency distribution of attenuations at  $69 \pm 3^\circ\text{N}$  for a wavelength of  $\lambda = 200$  nm. We only considered boxes in which the particle radii were greater than 0 nm to exclude mixtures with dust particles. We chose 200 nm because this allows easy extrapolation to longer wavelengths, and the extinction at this wavelength is comparable to the peak at 3000 nm (see Figure 6.1). The distributions in Figure 6.2 show a slow decline in the future years, which indicates that larger attenuations will occur more frequently in the future. We find that almost all columns contain ice. This is consistent with observations of polar mesosphere summer echoes (PMSE), which are almost always present in polar and Arctic latitudes in summer (Latteck et al., 2021). Figure 6.2 also shows the frequency distribution for  $\lambda = 126$  nm in 2080, again for  $69 \pm 3^\circ\text{N}$ . The distribution reaches much higher attenuations than  $\lambda = 200$  nm, showing that extinctions and attenuations increase rapidly with decreasing wavelength, as shown in Figure 6.1.

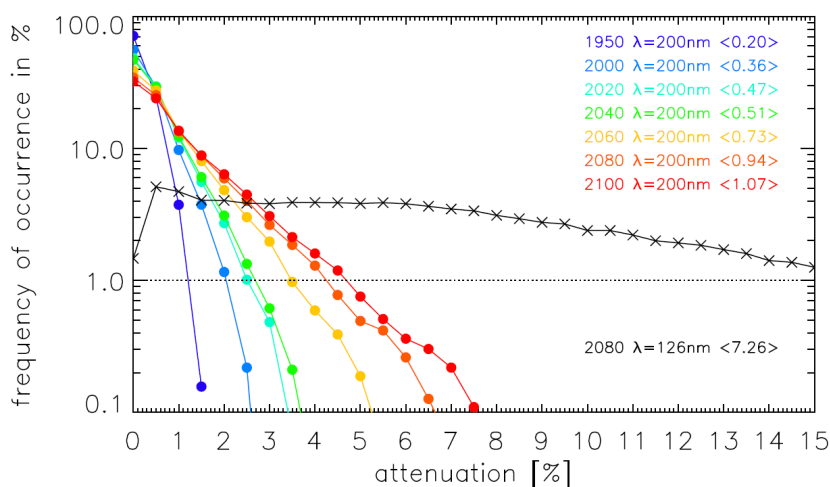


FIGURE 6.2: The relative occurrence frequency of attenuations at  $69 \pm 3^\circ\text{N}$  from various years (see inlet) for a wavelength of  $\lambda = 200$  nm (dots). The values for  $\lambda = 126$  nm (black, crosses, 2080 only) demonstrate that attenuations are increasing rapidly for decreasing wavelengths. The inlet also lists the mean attenuations ( $\langle \dots \rangle$ ) in %. Figure taken from Lübken et al. (2024), Fig. 3.

Next, we analysed the long-term trends in mean optical thickness and attenuation at  $\lambda = 126$  nm at  $69 \pm 3^\circ\text{N}$ . Figure 6.3 shows that the mean absorption at  $\lambda = 126$  nm increases from about 3% in 1950 to about 7% in 2100. The variability of the mean absorption is about a factor of two. In specific regions, the absorption can increase to 30% by 2100. For the visible spectrum at 532 nm (not shown), the mean attenuation increases from 0.0030% in 1950 to 0.020% in 2100, corresponding

to an almost seven-fold increase. Locally, the maximum values can reach 0.35% by the year 2100.

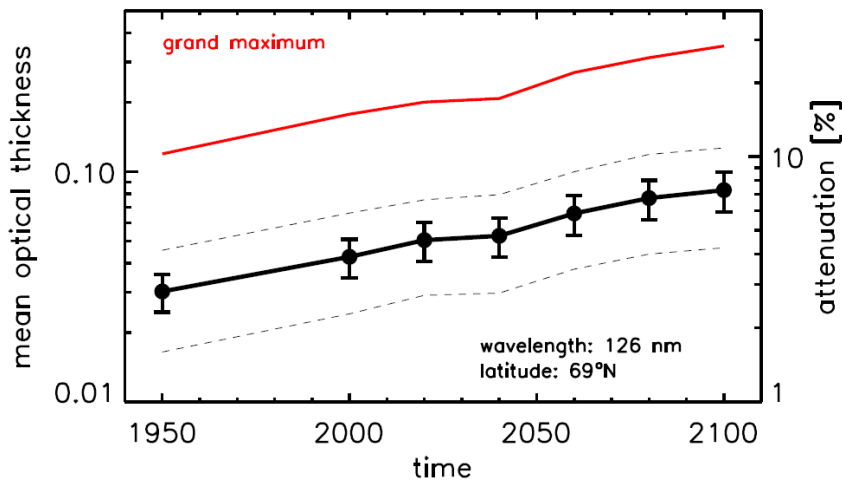


FIGURE 6.3: For each selected year, the mean extinction coefficients (left axis) and attenuations (right axis) are shown at  $69 \pm 3^\circ\text{N}$ . First, we average the extinction coefficients from all columns (only where NLC are present) at a given time-step. Then, we take the extinction coefficients from all time steps and determine the mean (dots), standard deviation (bars), and maximum and minimum values (dashed lines). Furthermore, the maximum extinction coefficient from all columns (before averaging) is shown (red line, “grand maximum”). Figure taken from Lübken et al. (2024), Fig.4.

We also analysed future extinction at different latitudes. We observed results consistent with those at  $69 \pm 3^\circ\text{N}$  and  $78 \pm 3^\circ\text{N}$ . However, at  $58 \pm 3^\circ\text{N}$ , the values are significantly lower. The analysis of the trends in total ice mass shows that the total amount of ice mass bound in NLC also increases with time, from 677 tons in 1950 to 1871 tons in 2100. The increase in ice mass strongly correlates with the concentration of methane (correlation coefficient: 0.98).

To assess the significance of the absorption of solar radiation by NLCs, we compare it with the variability caused by the solar cycle, which shows considerable variations across the wavelengths in both cases. For example, in the visible, the solar cycle variation is approximately 0.1% (see, for example, Figure 3 in Gray et al., 2010). Repeating the trend calculations shown in Figure 6.3 for  $\lambda = 532\text{ nm}$ , we found mean absorptions of 0.02% and maxima of  $\sim 0.35\%$  in the year 2100. This indicates that the maximum absorption by NLC in the visible can be significantly larger in some regions compared to the variations during a solar cycle. It is expected that the absorption of solar radiation by NLCs influences photochemistry in the mesosphere and stratosphere. Our model simulations with increasing methane suggest that the conditions for observing NLC will become more favourable in the future, with the frequency and brightness of NLC likely to increase significantly.

## Chapter 7

# Conclusion and outlook

### 7.1 Thesis summary

In this thesis, the response of NLCs and the background atmosphere to the solar cycle is analysed using the background atmosphere model LIMA and the microphysical ice transport model MIMAS. We also investigated the absorption of solar radiation by future enhancements in NLCs due to increasing water vapour concentrations caused by increased methane.

In Vellalassery et al. (2023), the responses of water vapour ( $\text{H}_2\text{O}$ ) and noctilucent clouds (NLCs) to the solar cycle are studied, focusing on recent solar cycles 23 and 24. Model simulations with and without microphysics were carried out to investigate the effects of NLC formation on the vertical  $\text{H}_2\text{O}$  profiles. The results revealed that the NLC formations cause a redistribution of the  $\text{H}_2\text{O}$  profiles. They consume  $\text{H}_2\text{O}$  from the background at ice-forming altitudes, leading to dehydration, and release it at ice-sublimating altitudes, leading to hydration, known as the freeze-drying effect. The variation in solar radiation affects the concentration of  $\text{H}_2\text{O}$  at NLC altitudes in two main ways: the impact of the temperature change and the effect of photolysis. Additional model simulations were performed under different background conditions to distinguish these two effects. It is found that the modulation of water vapour by the solar cycle temperature changes leads to a positive  $\text{H}_2\text{O}$  response at ice-forming altitudes and a negative response at ice-sublimating altitudes. On the other hand, the solar cycle photolysis effect causes only negative responses in the  $\text{H}_2\text{O}$  profile, with this effect dominating at altitudes where ice sublimation occurs. To the best of our knowledge, this is the first time that a positive correlation of water vapour with  $\text{Ly}\alpha$  fluctuations has been detected in the MLT region, and this is attributed to microphysical processes during NLC formation.

The time series of  $\text{H}_2\text{O}$  concentrations (averaged between an altitude of 80 and 85 km) in the satellite observations showed a lack of response in  $\text{H}_2\text{O}$  during the recent solar cycle 24 (Hervig et al., 2019). When the geometry of the satellite observations was used in the model, i.e. averaging the  $\text{H}_2\text{O}$  concentration between 80-85 km, a lack of response was found. This is because, at these altitudes,  $\text{H}_2\text{O}$  showed positive and negative (symmetric) responses that largely cancelled each other out when averaging.

In Vellalassery et al. (2024), the long-term trends in the response of NLC properties and the background atmosphere to the solar cycle are investigated for 1849-2019, which covers 15 complete solar cycles (solar cycle 10 to solar cycle 24). Background temperature and  $\text{H}_2\text{O}$  showed an apparent response to the solar cycle throughout the study period. This has intensified since 1960 due to increased greenhouse gas

emissions. This study analysed solar cycle responses in vertical distribution profiles of ice particle number, mean radius and NLC brightness. It becomes evident that the solar cycle influence is present at all altitudes and reaches its maximum at the height of maximum NLC brightness. The magnitude of the solar cycle affects ice particle radius, and the brightness increases with time, mainly due to the increase in H<sub>2</sub>O. At the same time, the profiles shift downwards in geometric altitudes due to atmospheric shrinking. The temperature fluctuation caused by the solar cycle is mainly responsible for the response of the NLC heights. The upward shift in NLC heights is due to the expansion of the atmosphere caused by the increased warming during the solar maximum. At different latitudes, the effects of the solar cycle on NLC properties are different. NLC height, maximum brightness and ice water content are more responsive at high and Arctic latitudes and show a similar trend. However, the occurrence of NLC is less affected at high and Arctic latitudes, while it is much more variable at mid-latitudes. This is because the water vapour saturation ratio of NLC events is higher at high and Arctic latitudes, while it is relatively low at mid-latitudes due to higher temperatures and lower water vapour concentrations. However, the occurrence of NLC is less affected at high and Arctic latitudes, while it varies much more at mid-latitudes. This is because the water vapour saturation ratio of NLC events is higher at high and Arctic latitudes, while it is relatively low at mid-latitudes due to higher temperatures and lower water vapour concentrations. As a result, temperature and water vapour fluctuations during the solar cycle have a larger influence on the occurrence of NLC at mid-latitudes than at high and Arctic latitudes.

In Lübken et al. (2024), the absorption of solar radiation by future enhancements of NLCs is analysed, with a particular focus on the increase in methane content, which is considered to be the leading cause of the increase in brightness and ice mass in NLCs and thus leads to greater absorption of solar radiation. The results indicate that UV absorption at  $\lambda = 126$  nm at a latitude of  $69 \pm 3^\circ\text{N}$  is expected to increase from  $\sim 3\%$  to  $\sim 7\%$ . In certain regions, absorption may increase to around 30% by the year 2100. In the visible range (532 nm), the average attenuation increases by a factor of  $\sim 7$  from 0.0030% (1950) to 0.020% (2100). In some regions, local absorption will reach up to 0.35% in 2100. This means that in certain areas, the maximum absorption by NLC in the visible range, as expected for 2100, is stronger than the variations over a solar cycle. These trends are similar at  $78 \pm 3^\circ\text{N}$  (compared to  $69 \pm 3^\circ\text{N}$ ) but are considerably smaller at  $58 \pm 3^\circ\text{N}$ . The total amount of ice mass bound in the NLC also increases with time, from 677 tonnes in 1950 to 1259 tonnes in 2050 and 1871 tonnes in 2100, respectively. This strongly correlates with methane concentration (correlation coefficient: 0.98), with each additional ppbv of methane increasing the ice mass by about 0.5 tonnes. Based on our previous studies of the effect of methane on NLC morphology, we can expect that the conditions for visible ground-based observers at mid-latitudes will become more favourable in the future, i.e. the frequency and brightness of NLC will increase significantly. In summary, the absorption of solar radiation by NLC is likely to impact photochemistry in the mesosphere and stratosphere.

## 7.2 Directions for future research

It is found that the increase in greenhouse gas concentrations is primarily responsible for the enhanced response of noctilucent clouds to the solar cycle, highlighting the impact of increasing anthropogenic emissions on the temperature and

water vapour concentration in the upper atmosphere. Given the continuing increase in greenhouse gas emissions, there will be more water vapour in the mesosphere and colder temperatures in the future, and consequently more NLCs. In Lübken et al. (2024), we analysed the impact of increasing methane on future NLCs up to the year 2100, focusing on the significance of NLC-solar radiation absorption by considering selected years. However, the effects of rising CO<sub>2</sub> on future NLCs have not been investigated. The combined effect of an increase in CO<sub>2</sub> and CH<sub>4</sub> on future NLCs could differ from an increase in CH<sub>4</sub> alone. For example, NLC altitudes (due to atmospheric shrinking) and maximum brightness could vary. One of the next steps to continue this work will be to investigate the separate impact of CO<sub>2</sub> and CH<sub>4</sub> increase on future NLCs based on different scenarios of increasing greenhouse gas emissions (IPCC RCP scenarios).

As Lübken et al. (2024) explain the absorption of solar radiation by NLCs in some local regions can be significantly larger than the variation throughout a solar cycle. This can have complex and wide-ranging effects on the photochemistry of the mesosphere and stratosphere, particularly affecting chemical reactions and distributions of minor chemical constituents with potential impacts on atmospheric composition and climate. In order to make more quantitative statements, more sophisticated modelling is required with interactively included chemistry in MIMAS, which will be another area for future research.

Given the important role of the solar cycle in the Earth's atmosphere, understanding how it affects the upper mesosphere is important for improving climate modelling. In the future, the results presented in this thesis can be used to improve the models. For example, the response of H<sub>2</sub>O under NLC conditions depends on the altitude. This information could be incorporated in future developments of atmospheric models, especially for the chemical component, as water vapour plays a crucial role in the chemistry of the upper mesosphere.

Climate change and the solar cycle will likely impact atmospheric circulation patterns in the mesosphere, possibly impacting background conditions and gravity waves (e.g. Butchart, 2014). Unfortunately, little is known about the long-term effects of these changes on summer mesopause dynamical, thermal, and compositional properties. We look forward to a new gravity wave-resolving model in the future to investigate the effects of changing dynamics due to changing greenhouse gases and solar cycle variations. In addition, turbulence and vertical winds have a significant influence on the freeze-drying effect, which in turn influences water vapour concentration and NLCs. Given the significant role that these factors play, one of the next steps will be to investigate the influence of turbulence and vertical winds on NLCs and water vapour distribution.



# Bibliography

- Akmaev, R.A., V.I. Fomichev, and X. Zhu (2006). "Impact of middle-atmospheric composition changes on greenhouse cooling in the upper atmosphere". In: *Journal of Atmospheric and Solar-Terrestrial Physics* 68.17, pp. 1879–1889. ISSN: 13646826. DOI: 10.1016/j.jastp.2006.03.008.
- Backhouse, TW (1885). "The luminous cirrus cloud of June and July". In: *Meteorol. Mag* 20, pp. 133–133.
- Beig, G. (2011). "Long-term trends in the temperature of the mesosphere/lower thermosphere region: 1. Anthropogenic influences". In: *Journal of Geophysical Research: Space Physics* 116.A2, n/a–n/a. ISSN: 01480227. DOI: 10.1029/2011JA016646.
- Beig, G., P. Keckhut, R. P. Lowe, Raymond G. Roble, Martin G. Mlynczak, J. Scheer, V. I. Fomichev, D. Offermann, W. J. R. French, M. G. Shepherd, A. I. Semenov, E. E. Remsberg, C. Y. She, Franz Josef Lübken, J. Bremer, B. R. Clemesha, J. Stegman, F. Sigernes, and S. Fadnavis (2003). "Review of mesospheric temperature trends". In: *Reviews of Geophysics* 41.4. ISSN: 8755-1209. DOI: 10.1029/2002RG000121.
- Berger, Uwe (2008). "Modeling of middle atmosphere dynamics with LIMA". In: *Journal of Atmospheric and Solar-Terrestrial Physics* 70.8-9, pp. 1170–1200. ISSN: 13646826. DOI: 10.1016/j.jastp.2008.02.004.
- Berger, Uwe and Franz Josef Lübken (2011). "Mesospheric temperature trends at mid-latitudes in summer". In: *Geophysical Research Letters* 38.22. ISSN: 00948276. DOI: 10.1029/2011GL049528.
- (2015). "Trends in mesospheric ice layers in the Northern Hemisphere during 1961-2013". In: *Journal of Geophysical Research* 120.21, pp. 277–11. ISSN: 21562202. DOI: 10.1002/2015JD023355.
- Berger, Uwe and Ulf von Zahn (Nov. 2002). "Icy particles in the summer mesopause region: Three-dimensional modeling of their environment and two-dimensional modeling of their transport". In: *Journal of Geophysical Research: Space Physics* 107.A11. ISSN: 0148-0227. DOI: 10.1029/2001JA000316. URL: <https://agupubs.onlinelibrary.wiley.com/doi/10.1029/2001JA000316>.
- Brasseur, Guy P. and Susan Solomon (2005). *Aeronomy of the Middle Atmosphere*. Vol. 32. Dordrecht: Springer Netherlands. ISBN: 978-1-4020-3284-4. DOI: 10.1007/1-4020-3824-0.
- Bremer, J. and Uwe Berger (2002). "Mesospheric temperature trends derived from ground-based LF phase-height observations at mid-latitudes: comparison with model simulations". In: *Journal of Atmospheric and Solar-Terrestrial Physics* 64.7, pp. 805–816. ISSN: 13646826. DOI: 10.1016/S1364-6826(02)00073-1.
- Bremer, J. and D. Peters (2008). "Influence of stratospheric ozone changes on long-term trends in the meso- and lower thermosphere". In: *Journal of Atmospheric and Solar-Terrestrial Physics* 70.11-12, pp. 1473–1481. ISSN: 13646826. DOI: 10.1016/j.jastp.2008.03.024.
- Butchart, Neal (2014). "The Brewer-Dobson circulation". In: *Reviews of geophysics* 52.2, pp. 157–184.

- Chabrilat, Simon and Gaston Kockarts (1998). "Correction to "Simple parameterization of the absorption of the solar Lyman-alpha line"". In: *Geophysical Research Letters* 25.1, pp. 79–79. ISSN: 0094-8276. DOI: 10.1029/97GL03569.
- Compo, G. P., J. S. Whitaker, P. D. Sardeshmukh, N. Matsui, R. J. Allan, X. Yin, B. E. Gleason, R. S. Vose, G. Rutledge, P. Bessemoulin, S. BroNnimann, M. Brunet, R. I. Crouthamel, A. N. Grant, P. Y. Groisman, P. D. Jones, M. C. Kruk, A. C. Kruger, G. J. Marshall, M. Maugeri, H. Y. Mok, O. Nordli, T. F. Ross, R. M. Trigo, X. L. Wang, S. D. Woodruff, and S. J. Worley (2011). *The Twentieth Century Reanalysis Project*. DOI: 10.1002/qj.776.
- DeLand, Matthew T., Eric P. Shettle, G.E. Thomas, and J J Olivero (2003). "Solar backscattered ultraviolet (SBUV) observations of polar mesospheric clouds (PMCs) over two solar cycles". In: *Journal of Geophysical Research: Atmospheres* 108.D8. ISSN: 0148-0227. DOI: 10.1029/2002JD002398.
- (2006). "A quarter-century of satellite polar mesospheric cloud observations". In: *Journal of Atmospheric and Solar-Terrestrial Physics* 68.1, pp. 9–29. ISSN: 1364-6826. DOI: 10.1016/J.JASTP.2005.08.003.
- DeLand, Matthew T. and G.E. Thomas (2015). "Updated PMC trends derived from SBUV data". In: *Journal of Geophysical Research: Atmospheres* 120.5, pp. 2140–2166. ISSN: 2169-897X. DOI: 10.1002/2014JD022253.
- Douglass and Fioletov (2011). *Stratospheric ozone and surface ultraviolet radiation, in Global Ozone Research and Monitoring Project Report*. Vol. 52. Geneva, Switzerland: World Meteorological Organization, pp. 76–76.
- Eidhammer, Trude and Ove Havnes (2001). "Size dependence of the mesospheric dust temperature And its influence on the noctilucent clouds and polar mesosphere summer echo phenomena". In: *Journal of Geophysical Research: Space Physics* 106.A11, pp. 24831–24841. ISSN: 0148-0227. DOI: 10.1029/2001JA900036.
- Etheridge, D. M., L. P. Steele, R. J. Francey, and R. L. Langenfelds (1998). "Atmospheric methane between 1000 A.D. and present: Evidence of anthropogenic emissions and climatic variability". In: *Journal of Geophysical Research: Atmospheres* 103.D13, pp. 15979–15993. ISSN: 0148-0227. DOI: 10.1029/98JD00923.
- Fiedler, Jens, Gerd Baumgarten, Uwe Berger, P. Hoffmann, N. Kaifler, and Franz Josef Lübken (2011). "NLC and the background atmosphere above ALOMAR". In: *Atmospheric Chemistry and Physics* 11.12, pp. 5701–5717. ISSN: 1680-7324. DOI: 10.5194/acp-11-5701-2011.
- Fiedler, Jens, Gerd Baumgarten, Uwe Berger, and Franz Josef Lübken (2016). "Long-term variations of noctilucent clouds at ALOMAR". In: *Journal of Atmospheric and Solar-Terrestrial Physics* 162, pp. 79–89. ISSN: 13646826. DOI: 10.1016/j.jastp.2016.08.006.
- Fomichev, V. I., J.-P. Blanchet, and D. S. Turner (1998). "Matrix parameterization of the 15  $\mu\text{m}$  CO <sub>2</sub> band cooling in the middle and upper atmosphere for variable CO <sub>2</sub> concentration". In: *Journal of Geophysical Research: Atmospheres* 103.D10, pp. 11505–11528. ISSN: 0148-0227. DOI: 10.1029/98JD00799.
- Fomichev, V.I. and G.M. Shved (1988). "Net radiative heating in the middle atmosphere". In: *Journal of Atmospheric and Terrestrial Physics* 50.8, pp. 671–688. ISSN: 00219169. DOI: 10.1016/0021-9169(88)90031-1.
- Gadsden, M. (1982). *NOCTILUCENT CLOUDS*. Tech. rep.
- Gadsden, M and Wilfried Schröder (1989). "Noctilucent Clouds". In: *Noctilucent Clouds*. Berlin, Heidelberg: Springer Berlin Heidelberg, pp. 1–12. DOI: 10.1007/978-3-642-48626-5\_{1}.

- Garcia, Rolando R. (1989). "Dynamics, radiation, and photochemistry in the mesosphere: Implications for the formation of noctilucent clouds". In: *Journal of Geophysical Research: Atmospheres* 94.D12, pp. 14605–14615. ISSN: 0148-0227. DOI: 10.1029/JD094iD12p14605.
- Garcia, Rolando R., Daniel R. Marsh, D. E. Kinnison, B. A. Boville, and F. Sassi (2007). "Simulation of secular trends in the middle atmosphere, 1950-2003". In: *Journal of Geophysical Research Atmospheres* 112.9. ISSN: 01480227. DOI: 10.1029/2006JD007485.
- Gray, L. J., Juerg Beer, M. Geller, J. D. Haigh, M. Lockwood, K. Matthes, U. Cubasch, D. Fleitmann, G. Harrison, L. Hood, J. Luterbacher, G. A. Meehl, D. Shindell, B. van Geel, and W. White (2010). "SOLAR INFLUENCES ON CLIMATE". In: *Reviews of Geophysics* 48.4, RG4001. ISSN: 8755-1209. DOI: 10.1029/2009RG000282.
- Grygalashvyly, M. and G.R. Sonnemann (2006). "Trends of mesospheric water vapor due to the increase of methane – A model study particularly considering high latitudes". In: *Advances in Space Research* 38.11, pp. 2394–2401. ISSN: 02731177. DOI: 10.1016/j.asr.2006.09.010.
- Gumbel, J., David E. Siskind, G. Witt, K. M. Torkar, and M. Friedrich (2003). "Influences of ice particles on the ion chemistry of the polar summer mesosphere". In: *Journal of Geophysical Research: Atmospheres* 108.D8. ISSN: 0148-0227. DOI: 10.1029/2002JD002413.
- Hale, B. N. and P. L. M. Plummer (1974). "On Nucleation Phenomena I: A Molecular Model". In: *Journal of the Atmospheric Sciences* 31.6, pp. 1615–1621. ISSN: 0022-4928. DOI: 10.1175/1520-0469(1974)031<1615:ONPIAM>2.0.CO;2.
- Hartogh, P., G. R. Sonnemann, M. Grygalashvyly, Li Song, Uwe Berger, and Franz Josef Lübken (2010). "Water vapor measurements at ALOMAR over a solar cycle compared with model calculations by LIMA". In: *Journal of Geophysical Research* 115. ISSN: 0148-0227. DOI: 10.1029/2009jd012364.
- Hegglin, M. I., D. A. Plummer, T. G. Shepherd, J. F. Scinocca, J. Anderson, L. Froidevaux, B. Funke, D. Hurst, A. Rozanov, J. Urban, T. von Clarmann, K. A. Walker, H. J. Wang, S. Tegtmeier, and K. Weigel (2014). "Vertical structure of stratospheric water vapour trends derived from merged satellite data". In: *Nature Geoscience* 7.10, pp. 768–776. ISSN: 1752-0894. DOI: 10.1038/ngeo2236.
- Hervig, Mark E., Uwe Berger, and David E. Siskind (2016a). "Decadal variability in PMCs and implications for changing temperature and water vapor in the upper mesosphere". In: *Journal of Geophysical Research* 121.5, pp. 2383–2392. ISSN: 21562202. DOI: 10.1002/2015JD024439.
- Hervig, Mark E., Michael Gerding, Michael H. Stevens, Robert Stockwell, Scott M. Bailey, James M. Russell, and Gunter Stober (2016b). "Mid-latitude mesospheric clouds and their environment from SOFIE observations". In: *Journal of Atmospheric and Solar-Terrestrial Physics* 149, pp. 1–14. ISSN: 1364-6826. DOI: 10.1016/J.JASTP.2016.09.004.
- Hervig, Mark E., Larry L. Gordley, Lance E. Deaver, David E. Siskind, Michael H. Stevens, James M. Russell, Scott M. Bailey, Linda Megner, and Charles G. Bardeen (2009). "First Satellite Observations of Meteoric Smoke in the Middle Atmosphere". In: *Geophysical Research Letters* 36.18. ISSN: 0094-8276. DOI: 10.1029/2009GL039737.
- Hervig, Mark E., Marty McHugh, and Michael E. Summers (2003). "Water vapor enhancement in the polar summer mesosphere and its relationship to polar mesospheric clouds". In: *Geophysical Research Letters* 30.20. ISSN: 00948276. DOI: 10.1029/2003GL018089.

- Hervig, Mark E. and David E. Siskind (2006). "Decadal and inter-hemispheric variability in polar mesospheric clouds, water vapor, and temperature". In: *Journal of Atmospheric and Solar-Terrestrial Physics* 68.1, pp. 30–41. ISSN: 13646826. DOI: 10.1016/j.jastp.2005.08.010.
- Hervig, Mark E., David E. Siskind, Scott M. Bailey, Aimee W. Merkel, Matthew T. DeLand, and James M. Russell (2019). "The Missing Solar Cycle Response of the Polar Summer Mesosphere". In: *Geophysical Research Letters* 46.16, pp. 10132–10139. ISSN: 0094-8276. DOI: 10.1029/2019GL083485.
- Hervig, Mark E., David E. Siskind, Scott M. Bailey, and James M. Russell (2015). "The influence of PMCs on water vapor and drivers behind PMC variability from SOFIE observations". In: *Journal of Atmospheric and Solar-Terrestrial Physics* 132, pp. 124–134. ISSN: 13646826. DOI: 10.1016/j.jastp.2015.07.010.
- Hesstvedt, Eigil (1961). "Note on the nature of noctilucent clouds". In: *Journal of Geophysical Research* 66.6, p. 1985. ISSN: 0148-0227. DOI: 10.1029/JZ066i006p01985.
- Hunten, Donald M., Richard P. Turco, and Owen B. Toon (1980). "Smoke and Dust Particles of Meteoric Origin in the Mesosphere and Stratosphere". In: *Journal of the Atmospheric Sciences* 37.6, pp. 1342–1357. ISSN: 0022-4928. DOI: 10.1175/1520-0469(1980)037<1342:SADPOM>2.0.CO;2.
- Jesse, O (1885). "Auffallende abenderscheinungen am himmel". In: *Meteorol. Z* 20, pp. 311–312.
- Keckhut, P., William J. Randel, C. Claud, T. Leblanc, W. Steinbrecht, B.M. Funatsu, H. Bencherif, I.S. McDermid, A. Hauchecorne, C. Long, R. Lin, and Gerd Baumgarten (2011). "An evaluation of uncertainties in monitoring middle atmosphere temperatures with the ground-based lidar network in support of space observations". In: *Journal of Atmospheric and Solar-Terrestrial Physics* 73.5-6, pp. 627–642. ISSN: 13646826. DOI: 10.1016/j.jastp.2011.01.003.
- Kiliani, J. (2014). "INAUGURAL-DISSERTATION 3-D Modeling of Noctilucent Cloud Evolution and Relationship to the Ambient Atmosphere". In: ISSN: 1615-8083.
- Kockarts, Gaston (1980). "Nitric oxide cooling in the terrestrial thermosphere". In: *Geophysical Research Letters* 7.2, pp. 137–140. ISSN: 0094-8276. DOI: 10.1029/GL007i002p00137.
- Körner, Ulrich and G. R. Sonnemann (May 2001). "Global three-dimensional modeling of the water vapor concentration of the mesosphere-mesopause region and implications with respect to the noctilucent cloud region". In: *Journal of Geophysical Research: Atmospheres* 106.D9, pp. 9639–9651. ISSN: 0148-0227. DOI: 10.1029/2000JD900744.
- Laštovička, Jan (2013). "Trends in the upper atmosphere and ionosphere: Recent progress". In: *Journal of Geophysical Research: Space Physics* 118.6, pp. 3924–3935. ISSN: 2169-9380. DOI: 10.1002/jgra.50341.
- Latteck, Ralph, Toralf Renkwitz, and Jorge L. Chau (2021). "Two decades of long-term observations of polar mesospheric echoes at 69°N". In: *Journal of Atmospheric and Solar-Terrestrial Physics* 216, p. 105576. ISSN: 13646826. DOI: 10.1016/j.jastp.2021.105576.
- Lean, Judith L., Gary J. Rottman, H. Lee Kyle, Thomas N. Woods, John R. Hickey, and Lawrence C. Puga (1997). "Detection and parameterization of variations in solar mid- and near-ultraviolet radiation (200–400 nm)". In: *Journal of Geophysical Research: Atmospheres* 102.D25, pp. 29939–29956. ISSN: 0148-0227. DOI: 10.1029/97JD02092.
- Leslie, Robt. C. (1885). "Sky Glows". In: *Nature* 32.820, pp. 245–245. ISSN: 0028-0836. DOI: 10.1038/032245a0.

- Lübken, Franz Josef (1997). "Seasonal variation of turbulent energy dissipation rates at high latitudes as determined by in situ measurements of neutral density fluctuations". In: *Journal of Geophysical Research: Atmospheres* 102.D12, pp. 13441–13456. ISSN: 0148-0227. DOI: 10.1029/97JD00853.
- (1999). "Thermal structure of the Arctic summer mesosphere". In: *Journal of Geophysical Research: Atmospheres* 104.D8, pp. 9135–9149.
- Lübken, Franz Josef, Gerd Baumgarten, and Uwe Berger (2021). "Long term trends of mesospheric ice layers: A model study". In: *Journal of Atmospheric and Solar-Terrestrial Physics* 214, p. 105378. ISSN: 13646826. DOI: 10.1016/j.jastp.2020.105378.
- Lübken, Franz Josef, Gerd Baumgarten, Mykhaylo Grygalashvyly, and Ashique Vellalassery (2024). "Absorption of Solar Radiation by Noctilucent Clouds in a Changing Climate". In: *Geophysical Research Letters* 51.8. ISSN: 0094-8276. DOI: 10.1029/2023GL107334.
- Lübken, Franz Josef and Uwe Berger (2011). "Latitudinal and interhemispheric variation of stratospheric effects on mesospheric ice layer trends". In: *Journal of Geophysical Research* 116, D00P03. ISSN: 0148-0227. DOI: 10.1029/2010JD015258.
- Lübken, Franz Josef, Uwe Berger, and Gerd Baumgarten (2009). "Stratospheric and solar cycle effects on long-term variability of mesospheric ice clouds". In: *Journal of Geophysical Research Atmospheres* 114.21. ISSN: 01480227. DOI: 10.1029/2009JD012377.
- (2013). "Temperature trends in the midlatitude summer mesosphere". In: *Journal of Geophysical Research Atmospheres* 118.24, pp. 347–13. ISSN: 21698996. DOI: 10.1002/2013JD020576.
- (2018). "On the Anthropogenic Impact on Long-Term Evolution of Noctilucent Clouds". In: *Geophysical Research Letters* 45.13, pp. 6681–6689. ISSN: 19448007. DOI: 10.1029/2018GL077719.
- Lübken, Franz Josef, J. Höffner, T. P. Viehl, B. Kaifler, and R. J. Morris (2011). "First measurements of thermal tides in the summer mesopause region at Antarctic latitudes". In: *Geophysical Research Letters* 38.24, n/a–n/a. ISSN: 00948276. DOI: 10.1029/2011GL050045.
- Machol, J., M. Snow, D. Woodraska, Thomas N. Woods, R. Viereck, and O. Coddington (2019). "An Improved Lyman-Alpha Composite". In: *Earth and Space Science* 6.12, pp. 2263–2272. ISSN: 23335084. DOI: 10.1029/2019EA000648.
- Marsh, Daniel R., Michael J. Mills, Douglas E. Kinnison, Jean Francois Lamarque, Natalia Calvo, and Lorenzo M. Polvani (2013). "Climate change from 1850 to 2005 simulated in CESM1(WACCM)". In: *Journal of Climate* 26.19, pp. 7372–7391. ISSN: 08948755. DOI: 10.1175/JCLI-D-12-00558.1.
- Mlynczak, Martin G. and Susan Solomon (1993). "A detailed evaluation of the heating efficiency in the middle atmosphere". In: *Journal of Geophysical Research: Atmospheres* 98.D6, pp. 10517–10541. ISSN: 0148-0227. DOI: 10.1029/93JD00315.
- Murphy, D. M. and T. Koop (2005). "Review of the vapour pressures of ice and supercooled water for atmospheric applications". In: *Quarterly Journal of the Royal Meteorological Society* 131.608, pp. 1539–1565. ISSN: 00359009. DOI: 10.1256/qj.04.94.
- Murray, Benjamin J. and Eric J. Jensen (2010). "Homogeneous nucleation of amorphous solid water particles in the upper mesosphere". In: *Journal of Atmospheric and Solar-Terrestrial Physics* 72.1, pp. 51–61. ISSN: 13646826. DOI: 10.1016/j.jastp.2009.10.007.
- Nedoluha, Gerald E., Michael Kiefer, Stefan Lossow, R. Michael Gomez, Niklaus Kämpfer, Martin Lainer, Peter Forkman, Ole Martin Christensen, Jung Jin Oh,

- P. Hartogh, John Anderson, Klaus Bramstedt, Bianca M. Dinelli, Maya Garcia-Comas, Mark E. Hervig, Donal Murtagh, Piera Raspollini, William G. Read, Karen Rosenlof, Gabriele P. Stiller, and Kaley A. Walker (Dec. 2017). "The SPARC water vapor assessment II: intercomparison of satellite and ground-based microwave measurements". In: *Atmospheric Chemistry and Physics* 17.23, pp. 14543–14558. ISSN: 1680-7324. DOI: 10.5194/acp-17-14543-2017.
- Ogibalov, V.P. and V.I. Fomichev (2003). "Parameterization of solar heating by the near IR CO<sub>2</sub> bands in the mesosphere". In: *Advances in Space Research* 32.5, pp. 759–764. ISSN: 02731177. DOI: 10.1016/S0273-1177(03)80069-8.
- Philbrick, C.R., J. Barnett, R. Gerndt, D. Offermann, W.R. Pendleton, P. Schlyter, G. Witt, and J.F. Schmidlin (1984). "Temperature measurements during the CAMP program". In: *Advances in Space Research* 4.4, pp. 153–156. ISSN: 02731177. DOI: 10.1016/0273-1177(84)90278-3.
- Randel, William J., Keith P. Shine, John Austin, John Barnett, Chantal Claud, Nathan P. Gillett, P. Keckhut, Ulrike Langematz, Roger Lin, Craig Long, Carl Mears, Alvin Miller, John Nash, Dian J. Seidel, David W. J. Thompson, Fei Wu, and Shigeo Yoden (2009). "An update of observed stratospheric temperature trends". In: *Journal of Geophysical Research: Atmospheres* 114.D2. ISSN: 0148-0227. DOI: 10.1029/2008JD010421.
- Rapp, Markus, Franz Josef. Lübken, A. Müllemann, G. E. Thomas, and Eric J. Jensen (2002). "Small-scale temperature variations in the vicinity of NLC: Experimental and model results". In: *Journal of Geophysical Research: Atmospheres* 107.D19. ISSN: 0148-0227. DOI: 10.1029/2001JD001241.
- Rapp, Markus and G.E. Thomas (2006). "Modeling the microphysics of mesospheric ice particles: Assessment of current capabilities and basic sensitivities". In: *Journal of Atmospheric and Solar-Terrestrial Physics* 68.7, pp. 715–744. ISSN: 13646826. DOI: 10.1016/j.jastp.2005.10.015.
- Reid, George C. (1975). "Ice Clouds at the Summer Polar Mesopause". In: *Journal of the Atmospheric Sciences* 32.3, pp. 523–535. ISSN: 0022-4928. DOI: 10.1175/1520-0469(1975)032<0523:ICATSP>2.0.CO;2.
- Remsberg, Ellis, Robert Damadeo, Murali Natarajan, and Praful Bhatt (2018). "Observed Responses of Mesospheric Water Vapor to Solar Cycle and Dynamical Forcings". In: *Journal of Geophysical Research: Atmospheres* 123.7, pp. 3830–3843. ISSN: 21698996. DOI: 10.1002/2017JD028029.
- Riahi, Keywan, Shilpa Rao, Volker Krey, Cheolhung Cho, Vadim Chirkov, Guenther Fischer, Georg Kindermann, Nebojsa Nakicenovic, and Peter Rafaj (2011). "RCP 8.5—A scenario of comparatively high greenhouse gas emissions". In: *Climatic Change* 109.1-2, pp. 33–57. ISSN: 0165-0009. DOI: 10.1007/s10584-011-0149-y.
- Roble, Raymond G. and R E Dickinson (1989). *HOW WILL CHANGES IN CARBON DIOXIDE AND METHANE MODIFY THE MEAN STRUCTURE OF THE MESOSPHERE AND THERMOSPHERE ?* Tech. rep. 12, pp. 1441–1444.
- Rosinski, J. and R. H. Snow (1961). "SECONDARY PARTICULATE MATTER FROM METEOR VAPORS". In: *Journal of Meteorology* 18.6, pp. 736–745. ISSN: 0095-9634. DOI: 10.1175/1520-0469(1961)018<0736:SPMFMV>2.0.CO;2.
- Russell, James M., Scott M. Bailey, Larry L. Gordley, David W. Rusch, Mihály Horányi, Mark E. Hervig, Gary E. Thomas, Cora E. Randall, David E. Siskind, Michael H. Stevens, Michael E. Summers, Michael J. Taylor, Christoph R. Englert, Patrick J. Espy, William E. McClintock, and Aimee W. Merkel (2009). "The Aeronomy of Ice in the Mesosphere (AIM) mission: Overview and early science results". In: *Journal of Atmospheric and Solar-Terrestrial Physics* 71.3-4, pp. 289–299. ISSN: 13646826. DOI: 10.1016/j.jastp.2008.08.011.

- Schmidt, Daniela N., Ellen Thomas, Elisabeth Authier, David Saunders, and Andy Ridgwell (2018). "Strategies in times of crisis—insights into the benthic foraminiferal record of the Palaeocene–Eocene Thermal Maximum". In: *Philosophical Transactions of the Royal Society A: Mathematical, Physical and Engineering Sciences* 376.2130, p. 20170328. ISSN: 1364-503X. DOI: 10.1098/rsta.2017.0328.
- Schmidt, Gavin A., Reto Ruedy, James E. Hansen, Igor Aleinov, Nadine Bell, Mike Bauer, Susanne Bauer, Brian Cairns, Vittorio Canuto, Ye Cheng, Anthony Del Genio, Greg Faluvegi, Andrew D. Friend, Tim M. Hall, Yongyun Hu, Max Kelley, Nancy Y. Kiang, Dorothy Koch, Andy A. Lacis, Jean Lerner, Ken K. Lo, Ron L. Miller, Larissa Nazarenko, Valdar Oinas, Jan Perlwitz, Judith Perlwitz, David Rind, Anastasia Romanou, Gary L. Russell, Makiko Sato, Drew T. Shindell, Peter H. Stone, Shan Sun, Nick Tausnev, Duane Thresher, and Mao-Sung Yao (2006). "Present-Day Atmospheric Simulations Using GISS ModelE: Comparison to In Situ, Satellite, and Reanalysis Data". In: *Journal of Climate* 19.2, pp. 153–192. ISSN: 1520-0442. DOI: 10.1175/JCLI3612.1.
- Schröder, Wilfried (1999). "Were Noctilucent Clouds Caused by the Krakatoa Eruption? A Case Study of the Research Problems before 1885." In: *Bulletin of the American Meteorological Society* 80.10, pp. 2081–2086. DOI: 10.1175/1520-0477(1999)080<2081:WNCBCT>2.0.CO;2.
- Seele, Cord and P. Hartogh (1999). "Water vapor of the polar middle atmosphere: Annual variation and summer mesosphere Conditions as observed by ground-based microwave spectroscopy". In: *Geophysical Research Letters* 26.11, pp. 1517–1520. ISSN: 0094-8276. DOI: 10.1029/1999GL900315.
- Shettle, Eric P., Matthew T. DeLand, G. E. Thomas, and J. J. Olivero (2009). "Long term variations in the frequency of polar mesospheric clouds in the Northern Hemisphere from SBUV". In: *Geophysical Research Letters* 36.2. ISSN: 00948276. DOI: 10.1029/2008GL036048.
- Siskind, David E., Michael H. Stevens, Mark E. Hervig, and Cora E. Randall (2013). "Recent observations of high mass density polar mesospheric clouds: A link to space traffic?" In: *Geophysical Research Letters* 40.11, pp. 2813–2817. ISSN: 00948276. DOI: 10.1002/grl.50540.
- Sonnemann, G.R. and M. Grygalashvily (2005). "Solar influence on mesospheric water vapor with impact on NLCs". In: *Journal of Atmospheric and Solar-Terrestrial Physics* 67.1-2, pp. 177–190. ISSN: 13646826. DOI: 10.1016/j.jastp.2004.07.026.
- Strobel, Darrell F. (1978). "Photochemical-radiative damping and instability in the stratosphere, II. Numerical results". In: *Geophysical Research Letters* 5.6, pp. 523–525. ISSN: 0094-8276. DOI: 10.1029/GL005i006p00523.
- Sugiyama, Takuya (1994). "Ion-recombination nucleation and growth of ice particles in noctilucent clouds". In: *Journal of Geophysical Research: Space Physics* 99.A3, pp. 3915–3929. ISSN: 0148-0227. DOI: 10.1029/93JA02822.
- Thomas, G.E. (1996). "Is the polar mesosphere the miner's canary of global change?" In: *Advances in Space Research* 18.3, pp. 149–158. ISSN: 02731177. DOI: 10.1016/0273-1177(95)00855-9. URL: <https://linkinghub.elsevier.com/retrieve/pii/0273117795008559>.
- (2003). "Are noctilucent clouds harbingers of global change in the middle atmosphere?" In: *Advances in Space Research* 32.9, pp. 1737–1746. ISSN: 0273-1177. DOI: 10.1016/S0273-1177(03)90470-4.
- Thomas, G.E., Richard D. McPeters, and Eric J. Jensen (1991). "Satellite observations of polar mesospheric clouds by the solar backscattered ultraviolet spectral radiometer: Evidence of a solar cycle dependence". In: *Journal of Geophysical Research: Atmospheres* 96.D1, pp. 927–939. ISSN: 0148-0227. DOI: 10.1029/90JD02312.

- Thomas, G.E., J J. Olivero, Eric J. Jensen, Wilfried Schröder, and Owen B. Toon (1989). "Relation between increasing methane and the presence of ice clouds at the mesopause". In: *Nature* 338.6215, pp. 490–492. ISSN: 0028-0836. DOI: 10.1038/338490a0.
- Tolman, Richard C. (1949). "The Effect of Droplet Size on Surface Tension". In: *The Journal of Chemical Physics* 17.3, pp. 333–337. ISSN: 0021-9606. DOI: 10.1063/1.1747247.
- Turco, Richard P., R. C. Whitten, and O. B. Toon (1982). "Stratospheric aerosols: Observation and theory". In: *Reviews of Geophysics* 20.2, pp. 233–279. ISSN: 8755-1209. DOI: 10.1029/RG020i002p00233.
- Vellalassery, Ashique, Gerd Baumgarten, M. Grygalashvyly, and Franz Josef Lübken (2023). "Greenhouse gas effects on the solar cycle response of water vapour and noctilucent clouds". In: *Annales Geophysicae* 41.2, pp. 289–300. ISSN: 14320576. DOI: 10.5194/angeo-41-289-2023.
- (2024). "Long-Term Evolution in Noctilucent Clouds' Response to the Solar Cycle: A Model-Based Study". In: *Atmosphere* 15.1. ISSN: 20734433. DOI: 10.3390/atmos15010088.
- Vellalassery, Ashique, Dhanyalekshmi Pillai, Julia Marshall, Christoph Gerbig, Michael Buchwitz, Oliver Schneising, and Aparna Ravi (2021). "Using Tropospheric Monitoring Instrument (TROPOMI) measurements and Weather Research and Forecasting (WRF) CO modelling to understand the contribution of meteorology and emissions to an extreme air pollution event in India". In: *Atmospheric Chemistry and Physics* 21.7, pp. 5393–5414. ISSN: 1680-7324. DOI: 10.5194/acp-21-5393-2021.
- Walcek, Chris J. (2000). "Minor flux adjustment near mixing ratio extremes for simplified yet highly accurate monotonic calculation of tracer advection". In: *Journal of Geophysical Research: Atmospheres* 105.D7, pp. 9335–9348. ISSN: 0148-0227. DOI: 10.1029/1999JD901142.
- Walcek, Chris J. and Nenad M. Aleksic (1998). "A simple but accurate mass conservative, peak-preserving, mixing ratio bounded advection algorithm with FORTRAN code". In: *Atmospheric Environment* 32.22, pp. 3863–3880. ISSN: 13522310. DOI: 10.1016/S1352-2310(98)00099-5.
- Wilms, Henrike (2016). "Microphysics of ice particles in the polar summer mesosphere". PhD thesis. Ludwig-Maximilians-Universität München.
- Woods, Thomas N., W. Kent Tobiska, Gary J. Rottman, and John R. Worden (2000). *Improved solar Lyman  $\alpha$  irradiance modeling from 1947 through 1999 based on UARS observations*. DOI: 10.1029/2000ja000051.
- Yiğit, Erdal and Alexander S. Medvedev (2013). "Extending the Parameterization of Gravity Waves into the Thermosphere and Modeling Their Effects". In: pp. 467–480. DOI: 10.1007/978-94-007-4348-9\_{ }25.
- Yu, Wandu, Jia Yue, Rolando R Garcia, Martin G. Mlynczak, and James M. Russell (2023). "WACCM6 Projections of Polar Mesospheric Cloud Abundance Over the 21st Century". In: *Journal of Geophysical Research: Atmospheres* 128.15. ISSN: 2169-897X. DOI: 10.1029/2023JD038985.
- Zahn, Ulf von, Gerd Baumgarten, Uwe Berger, Jens Fiedler, and P. Hartogh (Dec. 2004). "Noctilucent clouds and the mesospheric water vapour: the past decade". In: *Atmospheric Chemistry and Physics* 4.11/12, pp. 2449–2464. ISSN: 1680-7324. DOI: 10.5194/acp-4-2449-2004. URL: <https://acp.copernicus.org/articles/4/2449/2004/>.
- Zahn, Ulf von and Uwe Berger (2003). "Persistent ice cloud in the midsummer upper mesosphere at high latitudes: Three-dimensional modeling and cloud interactions

- with ambient water vapor". In: *Journal of Geophysical Research: Atmospheres* 108.8. ISSN: 01480227. DOI: 10.1029/2002jd002409.
- Zhu, Yong and Reginald E. Newell (1994). "Atmospheric rivers and bombs". In: *Geophysical Research Letters* 21.18, pp. 1999–2002. ISSN: 0094-8276. DOI: 10.1029/94GL01710.



## Appendix A

# Vellalassery et al., 2023

Ashique Vellalassery et al. (2023). "Greenhouse gas effects on the solar cycle response of water vapour and noctilucent clouds". In: *Annales Geophysicae* 41.2, pp. 289–300. ISSN: 14320576. DOI: 10.5194/angeo-41-289-2023



# Greenhouse gas effects on the solar cycle response of water vapour and noctilucent clouds

Ashique Vellalassery, Gerd Baumgarten, Mykhaylo Grygalashvyly, and Franz-Josef Lübken

Leibniz Institute of Atmospheric Physics at the University of Rostock, Schloßstraße 6, 18225 Kühlungsborn, Germany

**Correspondence:** Ashique Vellalassery (ashique@iap-kborn.de)

Received: 9 February 2023 – Discussion started: 23 February 2023

Revised: 12 June 2023 – Accepted: 13 June 2023 – Published: 24 July 2023

**Abstract.** The responses of water vapour ( $\text{H}_2\text{O}$ ) and noctilucent clouds (NLCs) to the solar cycle are studied using the Leibniz Institute for Middle Atmosphere (LIMA) model and the Mesospheric Ice Microphysics And tranSPort (MIMAS) model. NLCs are sensitive to the solar cycle because their formation depends on background temperature and the  $\text{H}_2\text{O}$  concentration. The solar cycle affects the  $\text{H}_2\text{O}$  concentration in the upper mesosphere mainly in two ways: directly through the photolysis and, at the time and place of NLC formation, indirectly through temperature changes. We found that  $\text{H}_2\text{O}$  concentration correlates positively with the temperature changes due to the solar cycle at altitudes above about 82 km, where NLCs form. The photolysis effect leads to an anti-correlation of  $\text{H}_2\text{O}$  concentration and solar Lyman- $\alpha$  radiation, which gets even more pronounced at altitudes below  $\sim 83$  km when NLCs are present. We studied the  $\text{H}_2\text{O}$  response to Lyman- $\alpha$  variability for the period 1992 to 2018, including the two most recent solar cycles. The amplitude of Lyman- $\alpha$  variation decreased by about 40% in the period 2005 to 2018 compared to the preceding solar cycle, resulting in a lower  $\text{H}_2\text{O}$  response in the late period. We investigated the effect of increasing greenhouse gases (GHGs) on the  $\text{H}_2\text{O}$  response throughout the solar cycle by performing model runs with and without increases in carbon dioxide ( $\text{CO}_2$ ) and methane ( $\text{CH}_4$ ). The increase of methane and carbon dioxide amplifies the response of water vapour to the solar variability. Applying the geometry of satellite observations, we find a missing response when averaging over altitudes of 80 to 85 km, where  $\text{H}_2\text{O}$  has a positive response and a negative response (depending on altitude), which largely cancel each other out. One main finding is that, during NLCs, the solar cycle response of  $\text{H}_2\text{O}$  strongly depends on altitude.

## 1 Introduction

The 11-year solar cycle significantly influences the upper-atmosphere's temperature and water vapour ( $\text{H}_2\text{O}$ ) concentration.  $\text{H}_2\text{O}$  is one of the essential minor constituents in the mesosphere as it is the primary source of chemically active hydrogen radicals, influencing the chemistry of all other chemically active minor constituents (Brasseur and Solomon, 2005; Hartogh et al., 2010).  $\text{H}_2\text{O}$  concentration plays an essential role in the noctilucent cloud's (NLC) formation. NLCs are located at about 83 km altitude, consist of water ice particles, and owe their existence to the cold-summer mesopause region ( $\sim 130$  K) at middle and high latitudes. NLCs, also called polar mesospheric clouds, are formed in an environment where small changes in background  $\text{H}_2\text{O}$  and temperature can lead to significant changes in NLC properties (e.g. Thomas, 1996; DeLand et al., 2006; Shettle et al., 2009; Lübken et al., 2009).

In comparison to the lower atmosphere, little is known about the upper mesosphere–lower thermosphere (MLT, 75–110 km) due to a lack of observations at these altitudes. NLCs have been proposed as indicators of trends in background temperature and  $\text{H}_2\text{O}$  concentrations (Thomas and Olivero, 2001). Studying NLC properties provides insight into phenomena occurring at the altitude of NLCs. The 11-year solar cycle has been considered to cause quasi-decadal oscillation observed in NLCs (DeLand et al., 2003). NLCs are predicted to decrease during solar maximum due to increased heating and photolysis of  $\text{H}_2\text{O}$  (Garcia, 1989). However, some recent studies strongly suggest that the response of NLCs to the solar cycle has been absent from 2002 to the present (Fiedler et al., 2011; DeLand and Thomas, 2015; Hervig et al., 2016; Siskind et al., 2013). Hervig et al. (2019), using satellite observations, found that NLCs had a clear anti-correlation with

the solar cycle before 2002, and that response has been absent in recent years. The leading cause of this absence appears to be the suppression of the solar cycle response of H<sub>2</sub>O. Lyman- $\alpha$  (Ly $\alpha$ ) radiation is the primary cause of H<sub>2</sub>O photolysis and varies by a factor of 2 between solar minimum and maximum (Woods et al., 2000). Understanding the effects of the solar cycle on H<sub>2</sub>O is more complicated at NLC altitudes because of the interaction between NLCs and background H<sub>2</sub>O.

NLC growth leads to dehydration at higher altitudes (83–89 km) as ice particles are formed by consuming background H<sub>2</sub>O, and sublimation of ice particles leads to hydration at lower altitudes as H<sub>2</sub>O is released here (about 78–83 km) (Lübken et al., 2009; Hervig et al., 2003). Investigating the effects of NLCs on the background H<sub>2</sub>O requires an estimate of the H<sub>2</sub>O profile without NLCs. Investigations using satellite observations are limited due to uncertainty in the inferred background H<sub>2</sub>O without NLC and vertical resolutions on the order of a few 100 m. Therefore, using satellite observations to study H<sub>2</sub>O at NLC altitudes could yield misleading results due to biases in the estimated H<sub>2</sub>O profiles without NLC (Hervig et al., 2015). Hervig et al. (2015) suggest that, in future studies, one approach to investigate the effects of NLC on H<sub>2</sub>O would be to use a detailed microphysical NLC model. Therefore, for this study, simulations are performed with and without microphysics using the same background conditions, resulting in an H<sub>2</sub>O profile with and without NLC. This allows us to investigate how NLC formation changes the H<sub>2</sub>O background profile in detail.

We compare the model result to satellite observations published by Hervig et al. (2019) to investigate the mechanism behind the solar cycle response of NLC and H<sub>2</sub>O. We also focus on the missing solar cycle response of H<sub>2</sub>O during recent years. This paper aims to answer a number of questions. How does the formation of NLCs affect the H<sub>2</sub>O profile and the variation of water vapour with the solar cycle? How do the solar-cycle-induced temperature and photolysis changes affect the H<sub>2</sub>O response? Why is the response of water vapour to the solar cycle nearly absent in satellite observations after 2005 (Hervig et al., 2019)? Our study is focused on the core NLC period, i.e. July at  $68 \pm 5^\circ$  N. The following section describes the modelling framework of this study and discusses the various model simulations performed. The third section discusses the mechanisms behind the solar cycle H<sub>2</sub>O response, such as the separation of the solar-cycle-induced temperature and photolysis effects on H<sub>2</sub>O. Sections 4 and 5 explore the possible reasons behind the missing solar cycle response. Concluding remarks and a summary are given in the last section.

## 2 Model description and numerical experiments

### 2.1 Model

The modelling framework used in this study consists mainly of two components: the Leibniz Institute Middle Atmosphere (LIMA) model and the Mesospheric Ice Microphysics And transport (MIMAS) model (see Fig. 1). LIMA is a non-linear, global, 3D Eulerian grid point model reaching from the troposphere to the lower thermosphere which calculates winds and temperature and is well described in a number of papers (Berger, 2008; Lübken et al., 2013). The LIMA model in this study is nudged to reanalysis data from NOAA-CIRES (National Oceanic and Atmospheric Administration-Cooperative Institute for Research in Environmental Sciences 20CR; Compo et al., 2011) up to an altitude of 45 km. The resulting winds and temperatures in the mesosphere and lower thermosphere (MLT) are then used in MIMAS. The MIMAS model run was performed for all years with background wind conditions and gravity wave forcing from a representative year (1976).

MIMAS is a 3D Lagrangian transport model specifically designed for modelling ice particles in the MLT region (Berger and Lübken, 2015). MIMAS calculates NLC parameters from 10 May to 31 August, and it is constrained from middle latitudes to high latitudes ( $37\text{--}90^\circ$  N) with a horizontal grid resolution of  $1^\circ$  in latitude and  $3^\circ$  in longitude and a vertical resolution of 100 m from 77.8 to 94.1 km (163 levels). In this study, the dynamics calculated by LIMA, solar Ly $\alpha$ , and the initial H<sub>2</sub>O distribution are the input for MIMAS, as sketched in Fig. 1. Below the MIMAS lower boundary, two effects determine the mixing ratio of H<sub>2</sub>O in the stratosphere: (i) transport of H<sub>2</sub>O from the troposphere and (ii) oxidation of methane (CH<sub>4</sub>). The oxidation of each CH<sub>4</sub> molecule produces two H<sub>2</sub>O molecules. Methane is nearly completely converted to H<sub>2</sub>O in the mesosphere by photochemical processes (e.g. Lübken et al., 2018). MIMAS assumes that transport from the troposphere is constant. The increase in H<sub>2</sub>O is primarily through (ii), i.e. due to the increase in CH<sub>4</sub> concentration (Lübken et al., 2018). Then, mesospheric H<sub>2</sub>O in MIMAS is transported by background winds, dispersed by turbulent diffusion, and reduced by photolysis. Hence, we parametrize H<sub>2</sub>O as a function of CH<sub>4</sub> following Lübken et al. (2018) (see Sect. 2). MIMAS makes use of 40 million dust particles, which can act as condensation nuclei. Dust particles are formed from meteors evaporating in the atmosphere (for more details, see Berger and von Zahn, 2002; von Zahn and Berger, 2003; Killiani, 2014). These are then coated with ice in H<sub>2</sub>O-supersaturated regions and transported according to three-dimensional and time-dependent background winds, eddy diffusion, and sedimentation. In MIMAS, standard microphysical processes such as the Kelvin effect determine the nucleation and growth of ice particles (Berger and Lübken, 2015; Gadsden and Schröder, 1989). For the comparison with satellites, we used model run

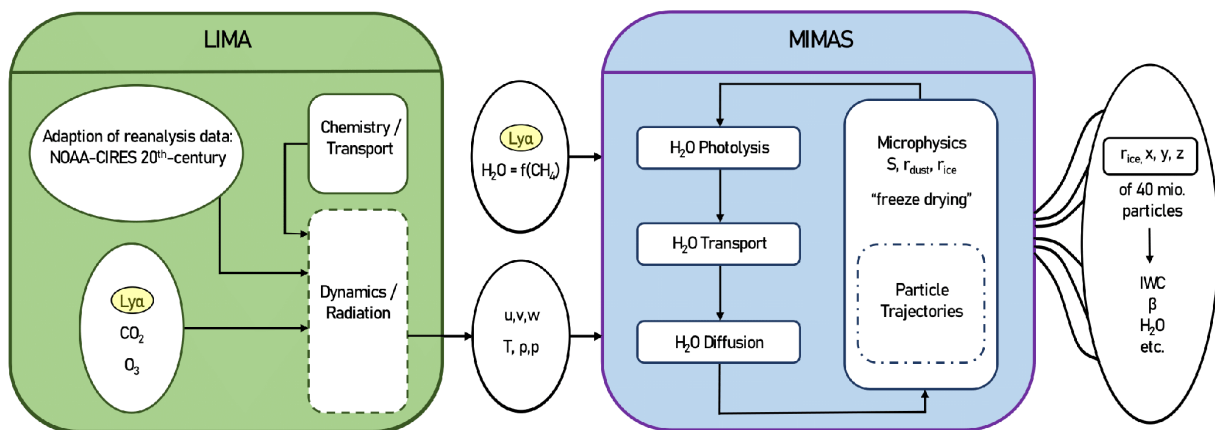


**Figure 1.** Sketch of the LIMA (green) and MIMAS (blue) models (from Lübken et al., 2021).

A, which includes CO<sub>2</sub> and CH<sub>4</sub> variations (Lübken et al., 2018, 2021). We performed MIMAS model simulations with ice formation turned off and on respectively to investigate the effects of ice formation on background H<sub>2</sub>O. In both runs, the background conditions and model inputs are the same. The main outputs of the model are the microphysical properties of the NLC ice particles, such as radius, backscatter value, and the number density of the ice and dust particles. More detailed descriptions of the MIMAS model and its precursors are available in the literature (Berger and von Zahn, 2002; Berger, 2008; Berger and Lübken, 2011; Lübken et al., 2018, 2021).

## 2.2 Model simulations

LIMA and MIMAS use daily Ly $\alpha$  fluxes taken from the LASP Interactive Solar Irradiance Data Center (LISIRD) as a proxy for solar activity from 1961 to 2019 (Machol et al., 2019). Ly $\alpha$  (and other spectral band) variations in LIMA cause atmospheric temperature variations, while Ly $\alpha$  variations in MIMAS cause photolysis of H<sub>2</sub>O. In LIMA, variations of other bands, namely, the Chappius band, Huggins band, Hartley band, Schumann–Runge band, and both Schumann–Runge continuums, are taken into account. The parametrization schemes are discussed in more detail in Berger, 2008 (see Sect. 2.2). Variations of these bands are parameterized based on Ly $\alpha$  values according to Lean et al. (1997). Therefore, it is possible to study the effects of the solar cycle on H<sub>2</sub>O due to temperature changes and photolysis separately by performing model simulations with constant and varying Ly $\alpha$  in MIMAS and LIMA. We conducted four model runs, as described in Table 1. We also performed LIMA model simulations with constant CO<sub>2</sub> for runs E, F, and G to filter out their effects on temperature changes. For these runs, we use a constant CH<sub>4</sub> concentration in MIMAS to avoid its influence on the H<sub>2</sub>O profile.

In LIMA, the mixing ratios of CO<sub>2</sub> (28–150 km) vary as function of time (years), while all other trace gases are kept

constant. An increase in CO<sub>2</sub> leads to a decrease in temperature in the stratosphere mainly due to enhanced cooling by CO<sub>2</sub> (e.g. Roble and Dickinson, 1989; Garcia et al., 2007; Berger and Lübken, 2011; Marsh et al., 2013; Lübken et al., 2013). At NLC altitudes, this cooling leads to an altitude decrease of pressure levels, referred to as the shrinking effect (Lübken et al., 2009). For LIMA, we use the long-term increase of CO<sub>2</sub> concentration according to observations at Mauna Loa (19° N, 155° W).

This study focuses mainly on the recent two solar cycles from 1992 to 2018. Figure 2 shows the time series of Ly $\alpha$ , CO<sub>2</sub>, and CH<sub>4</sub> for 1992–2018. The corresponding values of Ly $\alpha$ , CH<sub>4</sub>, and CO<sub>2</sub> for the years considered for this study are highlighted. We classify 1992–2005 as period 1 (early) and 2005–2018 as period 2 (late). Satellite observations of H<sub>2</sub>O showed a clear anti-correlation with the solar cycle in the early period, which was absent in the late period (Hervig et al., 2019). Certainly, at low and middle latitudes, without NLCs, one can detect only anticorrelation. For example, in H<sub>2</sub>O satellite data averaged over the tropics (30° N–30° S), anti-correlation is observed for the late period (Karagodin-Doyennel et al., 2021). To investigate the missing response reported in Hervig et al. (2019), we first examined the early-period solar minimum (1997) and maximum (2002) in more detail. The solar cycle affects the H<sub>2</sub>O concentration in two main ways: (i) through the photolysis of H<sub>2</sub>O by Ly $\alpha$  and (ii) through the temperature effect. We distinguish these effects by performing model simulations with different background conditions (see Table 1). Namely, in Sect. 3.3, we discuss the individual roles of solar-cycle-induced photolysis and temperature change on the H<sub>2</sub>O–solar-cycle response. Figure 2 shows that the intensity of Ly $\alpha$  radiation during the late period has decreased compared to the early period, and the concentrations of increased greenhouse gases (GHGs) have increased in the late period. The effects of reduced Ly $\alpha$  intensity and increased greenhouse gas (GHG) concentra-

**Table 1.** MIMAS simulations were carried out under different background conditions. The horizontal arrow stands for constant values for the given year; the vertical arrow is for varying parameters. How Ly $\alpha$  affects H<sub>2</sub>O is given for each run in the last column.

Model run	LIMA		MIMAS		Water vapour solar cycle response affected by
	CO <sub>2</sub>	Ly $\alpha$ T effect	CH <sub>4</sub>	Ly $\alpha$ photolysis effect	
A	↓	↓	↓	↓	– Temperature change (Ly $\alpha$ + CO <sub>2</sub> ) – Photo dissociation – Varying CH <sub>4</sub> (H <sub>2</sub> O source)
E	↔ 1997	↓	↔ 1997	↓	– Temperature change – Photo dissociation
F	↔ 1997	↓	↔ 1997	↔ 1997	– Temperature change
G	↔ 1997	↔ 1997	↔ 1997	↓	– Photo dissociation

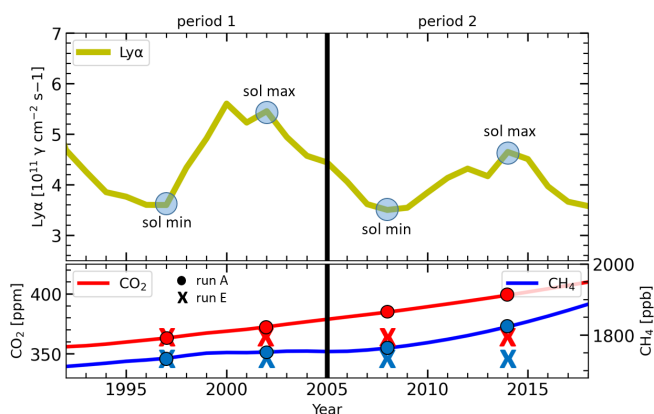


**Figure 2.** Time series of solar Ly $\alpha$ , CO<sub>2</sub>, and CH<sub>4</sub> for 1992–2018. The corresponding Ly $\alpha$ , CO<sub>2</sub>, and CH<sub>4</sub> values for the solar cycle maximum and minimum years used for this study are marked. The CO<sub>2</sub> and CH<sub>4</sub> values for run A are represented with dots, and for run E, they are represented with crosses. The study period is divided into period 1 as early (1992–2005) and period 2 as late (2005–2018).

tion on long-term H<sub>2</sub>O–solar-cycle response are discussed in Sect. 4.

### 3 Results and discussions

#### 3.1 Solar cycle response in ice water content (IWC)

To determine whether the model agrees with satellite observations, we compared the ice water content (IWC) anomaly from the model with the satellite observations (see Fig. 3). IWC anomalies are calculated as follows:

$$\text{IWC}_{\text{anom}} = 100\% \cdot \frac{\overline{\text{IWC}}_{\text{July}} - \overline{\text{IWC}}_{1981-2018}}{\overline{\text{IWC}}_{1981-2018}}, \quad (1)$$

where  $\overline{\text{IWC}}_{\text{July}}$  represent monthly zonal averages at 68° N, and  $\overline{\text{IWC}}_{1981-2018}$  are the averages of  $\overline{\text{IWC}}_{\text{July}}$  over the years 1981–2018. The IWC anomaly for satellite measurements are from the Solar Backscatter Ultraviolet (SBUV), Halogen Occultation Experiment (HALOE), Cloud Imaging and Particle Size (CIPS), and Solar Occultation For Ice Experiment (SOFIE) instruments. The time series of SBUV and HALOE data, as shown in Fig. 3, represent 3 years of sliding-averaged values. For more details on the satellite datasets, see Hervig et al. (2019). For this comparison, we used the MIMAS run A, in which the simulations are performed with increasing concentrations of CO<sub>2</sub> and CH<sub>4</sub>. For the comparison, we applied the same calculation method to our model data as Hervig et al. (2019) did to satellite observations, namely, we used a threshold of 50 g km<sup>-3</sup> for integrated water content because the polar mesospheric cloud (PMC) detection threshold for SBUV is 50 g km<sup>-3</sup> (DeLand and Thomas, 2015, 2019).

We find an anti-correlation between MIMAS IWC anomaly and Ly $\alpha$  flux throughout the entire period (1981–2018), with a weaker response in the late period. In satellite observations, SBUV measurements also show an anti-correlation with Ly $\alpha$  flux until 2005, after which the response becomes weaker in agreement with MIMAS. The magnitude of the solar cycle IWC anomaly in SBUV and HALOE is of the same order as the IWC anomaly in MIMAS. The IWC anomalies of CIPS and SOFIE do not show a clear response to the solar cycle. We notice that the year-to-year IWC variation in CIPS and SOFIE is larger than the IWC modulation during a solar cycle.

IWC anomalies of SBUV and HALOE correlate well with MIMAS IWC anomalies before 2005 and progressively weaken afterwards. Lübken et al. (2009) found a good agreement between NLC parameters calculated by MIMAS and satellite observations. The general agreement between the

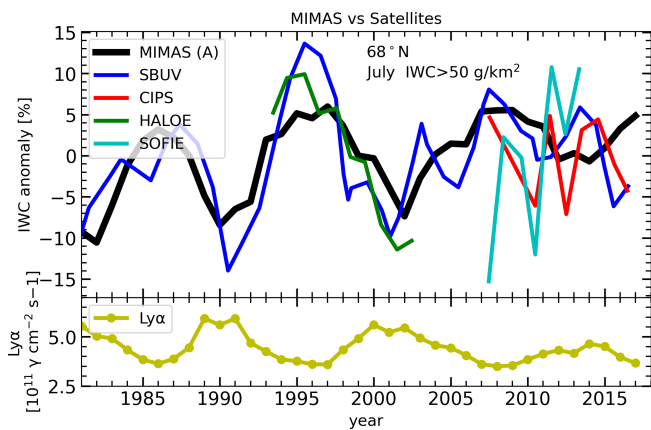


**Figure 3.** Time series of July mean IWC anomalies at  $68^\circ$  N from model and satellites based on Hervig et al. (2019). Anomalies for each dataset are calculated as the difference from their long-term mean. To reduce year-to-year variability, the time series of SBUV and HALOE are smoothed using the sliding-average method of window size 3.  $\text{Ly}\alpha$ -solar-cycle modulation is shown in the bottom panel.

main characteristics and trends of the ice layers in MIMAS and the observations suggests that the microphysical and photochemical processes in MIMAS cover the main processes relevant to NLC formation (Lübken et al., 2009).

### 3.2 Effect of NLC on water vapour ( $\text{H}_2\text{O}$ )

We calculated the zonal mean monthly averaged vertical profiles of  $\text{H}_2\text{O}$  and temperature to investigate the impact of NLC formation on the  $\text{H}_2\text{O}$  profile. Figure 4 shows the vertical  $\text{H}_2\text{O}$  profile averaged for July at  $68^\circ$  N latitude and given at pressure altitudes  $z_p = H_p \ln(p_0/p)$ , where  $p$  is the pressure of the model level,  $p_0$  is the pressure at the surface, and  $H_p = 7$  km is the pressure scale height. This figure illustrates the effect of NLC formation on the background profile of water vapour since the  $\text{H}_2\text{O}$  profile with NLC differs from that without NLC. In the presence of NLC, there is a reduction in the water vapour mixing ratio (dehydration) between 83–90 km, i.e. in the region where the saturation ratio of water vapour is larger than 1. An enhancement in water vapour (hydration) is observed at altitudes between 79–83 km, where the saturation ratio of water vapour is smaller than 1. An environment with a water vapour saturation ratio larger than 1 is supersaturated, meaning ice particles can grow under these conditions, whereas a saturation ratio lower than 1 leads to ice sublimation. The degree of saturation depends on the background atmosphere's  $\text{H}_2\text{O}$  concentration and temperature. Ice particle formation starts at higher altitudes, where the temperature is the lowest, and then it sediments downward. During sedimentation, the ice particles grow by consuming  $\text{H}_2\text{O}$  from the surrounding background, which decreases background  $\text{H}_2\text{O}$  concentration. Then they approach a region with a saturation ratio smaller than 1, where they

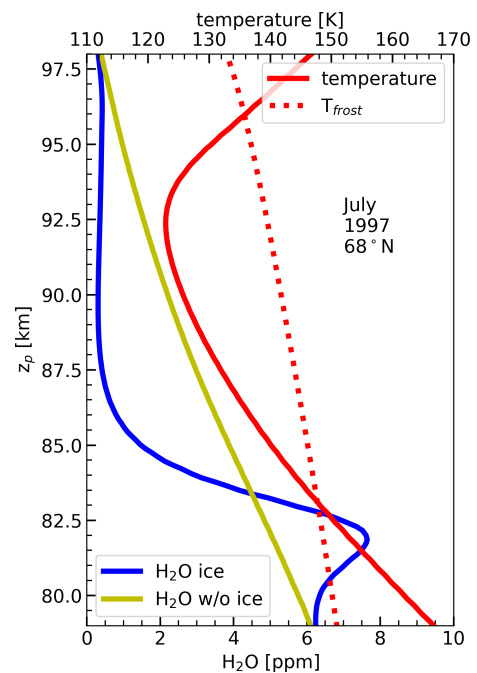


**Figure 4.** Zonally and monthly averaged  $\text{H}_2\text{O}$  and temperature profiles for July at  $68^\circ$  N from MIMAS with and without NLCs. The dotted red line represents frost point temperature. The blue lines show the background  $\text{H}_2\text{O}$  concentration with NLC, and the yellow lines show the  $\text{H}_2\text{O}$  concentration without NLC.

sublimate, releasing the water vapour. This is the so-called freeze-drying effect well discussed in a number of papers (Hervig et al., 2003; Lübken et al., 2009; Bardeen et al., 2010). The results in Fig. 4 illustrate the freeze-drying effect described above and also indicate that the effects of NLC on  $\text{H}_2\text{O}$  are not present below  $\sim 79$  km and above  $\sim 97$  km. This is the novelty of the results in Fig. 4. This is because the photochemical lifetime of water vapour below  $\sim 79$  km becomes larger than dynamical characteristic times, and distributions of water vapour become dynamically determined. Above 97 km, the saturation ratio of water vapour is smaller than 1; consequently, there is no NLC formation and consequently no effect on water vapour.

### 3.3 Effect of solar-cycle-induced temperature and photolysis changes on water vapour ( $\text{H}_2\text{O}$ )

We investigate the temperature change between the solar minimum (1997) and maximum (2002) due to solar irradiance variation and how these changes affect the  $\text{H}_2\text{O}$  profile. Different model runs performed for this study are summarized in Table 1. The differences (solar maximum – solar minimum) for  $\text{H}_2\text{O}$  and temperature profiles are shown in Fig. 5 for three model runs, namely E, F, and G. In run E, the solar-cycle-induced temperature change and photolysis influence  $\text{H}_2\text{O}$  concentration. In run F, only the temperature change caused by the solar cycle affects the  $\text{H}_2\text{O}$  concentra-

tion, while in run G, only the photolysis caused by the solar cycle affects the H<sub>2</sub>O concentration (see Table 1). All of these runs are performed with constant CO<sub>2</sub> and CH<sub>4</sub> concentrations to avoid the effects of increasing GHG concentrations on temperature and H<sub>2</sub>O profiles.

In model run F, Ly $\alpha$  is held constant in MIMAS so the photolysis of H<sub>2</sub>O is constant during the solar cycle. However, Ly $\alpha$  (and other bands) varies in the LIMA model so the background temperature varies with the solar cycle. Therefore, the change in the H<sub>2</sub>O profile during the solar cycle is only due to the influence of the solar cycle on temperature and sequentially on microphysical processes. Figure 5a shows that the temperature increases during solar maximum compared to during solar minimum through the entire altitude range (79–97 km). The difference in temperature amounts to  $\sim 0.5$ – $1.7$  K with maximum values at  $\sim 95$  km. During solar maximum, increased solar irradiance leads to greater absorption of solar radiation in the MLT region by molecular oxygen and water vapour, which heats the background atmosphere. Temperature differences decrease as altitude decreases because the intensity of solar radiation decreases due to atmospheric absorption by molecular oxygen and water vapour. The solar cycle effect in the H<sub>2</sub>O profile with NLC (blue line) differs significantly from that without NLC (yellow line). Without NLC, the H<sub>2</sub>O profile difference is nearly zero at all altitudes, indicating that the temperature changes do not significantly affect the background H<sub>2</sub>O profile in the absence of NLC. With NLC, the H<sub>2</sub>O profile difference is positive in the altitude range of 82–87 km and slightly negative in the range from 79–82 km. The atmosphere is warmer during solar maximum; therefore, the ice formation rate is lower during solar maximum. When the ice formation rate decreases, the amount of water vapour consumed from the background decreases; hence, more H<sub>2</sub>O is left in the background during solar maximum compared to during solar minimum, resulting in a slightly positive response at NLC-forming altitudes above 83 km. Below that altitude, the slightly negative response is due to reduced ice formation in the nucleation region during solar maximum, which decreases H<sub>2</sub>O released at ice sublimation altitudes. The positive difference peak at  $\sim 83$  km is located near the bottom of the H<sub>2</sub>O-saturated zone. Ice formation and sublimation are more sensitive to an increase in background temperature in this zone (where the degree of saturation is close to 1) because, at these altitudes, the background temperature is almost equal to the frost point temperature so an increase in background temperature critically changes the degree of saturation. The change of the background temperature in a region where it is significantly lower than the frost point temperature is not critical for the degree of saturation. Overall, the temperature variation due to the solar cycle causes a positive H<sub>2</sub>O response to the solar cycle at ice formation altitudes and a slightly negative response at ice sublimation altitudes.

In model run G (Fig. 5b), we consider only the effect of solar-cycle-induced Ly $\alpha$  variation on water vapour photolysis.

The background temperature is held constant. Photolysis of H<sub>2</sub>O by Ly $\alpha$  radiation molecules mainly produces atomic hydrogen (H) and hydroxyl (OH) in the upper atmosphere ( $\sim 90\%$ ) and, to a lesser extent, O(<sup>1</sup>D) with molecular hydrogen ( $\sim 10\%$ ). The photolysis rate is higher during solar maximum due to the increased Ly $\alpha$  flux caused by the increased solar activity. Without NLC, the difference in the H<sub>2</sub>O profile is negative at all altitudes (yellow line), indicating that the background H<sub>2</sub>O is reduced during solar maximum due to increased photolysis. Figure 5b shows that the negative response peaks at an altitude of  $\sim 87.5$  km. The solar cycle effect on the photolysis of H<sub>2</sub>O decreases above 87.5 km because the water vapour mixing ratio decreases with increasing altitude. The solar cycle variation of the photolysis effect decreases below 87.5 km because the solar Ly $\alpha$  radiation intensity decreases.

With NLC (blue line), the H<sub>2</sub>O difference between the solar maximum and the solar minimum is essentially negative at ice sublimation altitudes (below  $\sim 83$  km) and negligible at higher altitudes (above  $\sim 85$  km). This is due to the redistribution of the H<sub>2</sub>O profile during NLC formation (freeze drying). During solar maximum, the background H<sub>2</sub>O concentration available for ice formation is reduced due to enhanced photolysis. The lower H<sub>2</sub>O availability during solar maximum results in lower ice formation and, thus, lower H<sub>2</sub>O release during sublimation, leading to lower hydration in the sublimation zone. For this reason, the solar cycle variation of the photolysis effect is more pronounced at sublimation altitudes. Above 85 km, the effect of photolysis, in the case with NLC, is minimal because of the lower availability of H<sub>2</sub>O due to dehydration by NLC.

Figure 5c shows a combination of both effects, namely the solar-cycle-induced temperature change and photolysis effects on H<sub>2</sub>O. Without NLC (yellow line), the H<sub>2</sub>O profile shows a negative response at all altitudes, peaking at  $\sim 87.5$  km similar to run G (Fig. 5b, yellow line). We found that the variation of temperature has an almost negligible effect on the H<sub>2</sub>O in the absence of NLC (see Fig. 5a, yellow line) so the negative response of water vapour without consideration of microphysical processes (yellow line on Fig. 5c) is mainly caused by the photolysis effect. With NLC (Fig. 5c, blue line), the combined effect of temperature and photolysis has a slightly positive response to water vapour in the ice formation zone (83–89 km) and a negative response in the ice sublimation zone (80–83 km). The slightly positive response is caused by the temperature modulation, and the negative response is primarily due to the photolysis modulation throughout the solar cycle.

The study proves that the water vapour response to the solar cycle is affected by the re-distribution of water in the presence of NLC. There may exist regions with positive correlations of water vapour with Ly $\alpha$  when NLC formation occurs. Without NLC, the water vapour always shows a negative correlation with the solar cycle. When comparing the effects of solar cycle modulations of temperatures and photolysis on

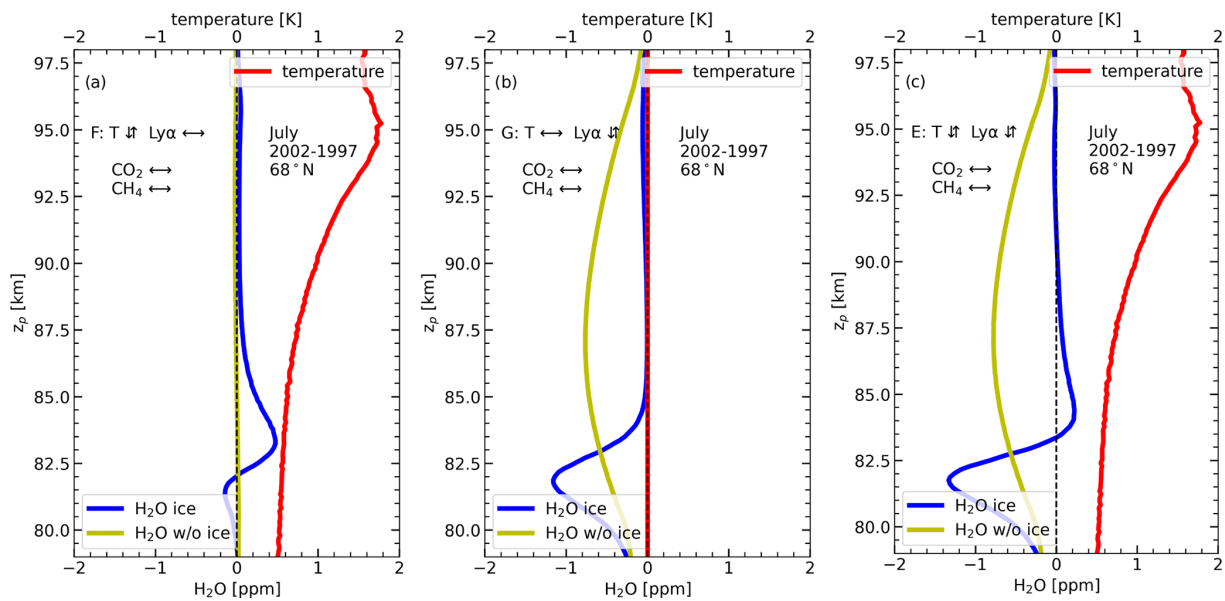


**Figure 5.** The difference in profiles between solar maximum (2002) and minimum (1997) for July mean H<sub>2</sub>O and temperatures. The blue and yellow lines represent NLC and non-NLC conditions. In all cases, CO<sub>2</sub> and CH<sub>4</sub> values are constant, corresponding to 1997. (a) Run F: only temperature change effects on H<sub>2</sub>O. (b) Run G: only photolysis change effect on H<sub>2</sub>O. (c) Run E: both temperature change and photolysis change effects on H<sub>2</sub>O.

H<sub>2</sub>O, the photolysis has a stronger effect on water vapour; however, the variation of temperature induces a positive correlation of solar irradiance and H<sub>2</sub>O.

#### 4 Increasing greenhouse gases and reducing solar cycle

This section examines how the increase in GHGs affects the H<sub>2</sub>O response to the solar cycle. To distinguish the GHG effects, we compared the model results with increasing CO<sub>2</sub> and CH<sub>4</sub> (run A) to the model run with constant CO<sub>2</sub> and CH<sub>4</sub> (run E). It is noted already that an increasing CO<sub>2</sub> concentration leads to a cooling of the middle atmosphere, and an increase in CH<sub>4</sub> concentration leads to an increase in H<sub>2</sub>O concentration (see Sect. 2 for details). In Fig. 2, the concentrations of CO<sub>2</sub> and CH<sub>4</sub> increase during the late period, and at the same time, the peak of the Ly $\alpha$  flux decreases. In order to filter out the effect of reduced Ly $\alpha$  intensity, we calculated the H<sub>2</sub>O response profile per unit of Ly $\alpha$  ( $\Delta\text{H}_2\text{O} / \Delta\text{Ly}\alpha$ ). Figure 6 shows the result for the first (1997–2002, blue line) and the second period (2008–2014, orange line) for model runs E (Fig. 6a) and A (Fig. 6b) respectively. These profiles show positive and negative responses depending on altitude. Under the conditions of constant GHGs (run E), the sensitivity of water vapour to Ly $\alpha$  does not change from the early to the late period (Fig. 6a). As expected, for the case of growing methane and carbon dioxide (run A), the sensitivity of water vapour to Ly $\alpha$  increases during the late period (orange line, Fig. 6b) compared to during the early period (blue line, Fig. 6b). This is because an increase in CO<sub>2</sub> (and conse-

quently, a temperature decrease) leads to an intensification of microphysical processes and, hence, to the increased freeze drying. In addition, increasing methane leads to more water vapour in the upper mesosphere, which also leads to an increased water vapour variation with solar cycle.

To study the effect of a decreasing Ly $\alpha$  amplitude during the late period (2008–2014), we calculated the ratio of water vapour absolute deviations between solar minimum and solar maximum for the early and late periods. The amplitude of Ly $\alpha$  variation is weaker during the late period ( $\sim 1.14 \times 10^{11}$  [phot. cm<sup>-2</sup> s<sup>-1</sup>] per solar cycle) compared to the early period ( $\sim 1.85 \times 10^{11}$  [phot. cm<sup>-2</sup> s<sup>-1</sup>] per solar cycle). The intensity of Ly $\alpha$  during the late-period solar maximum is reduced by  $\sim 40\%$  compared to during the early period. As can be seen from Fig. 7a, the magnitudes of positive and negative H<sub>2</sub>O responses decreased during the late period for model runs with constant GHGs (run E). In Fig. 6a, we found that the H<sub>2</sub>O sensitivity to Ly $\alpha$  flux is the same in the early and late periods for the model run with constant GHGs (run E). Therefore, the reduced response of H<sub>2</sub>O during the late period in model run E (Fig. 7a) is only due to the reduced solar Ly $\alpha$  variation. Comparing the late-period H<sub>2</sub>O response to the solar cycle from model runs with constant GHGs (Fig. 7a, orange line) to that from model runs with increasing GHGs (Fig. 7b, orange line) suggests that both the positive and negative peak responses are enhanced by increasing GHG concentration. Due to the increased solar Ly $\alpha$  flux and greenhouse gases, the NLC and water vapour response are expected to increase during the current solar cycle 25 as the

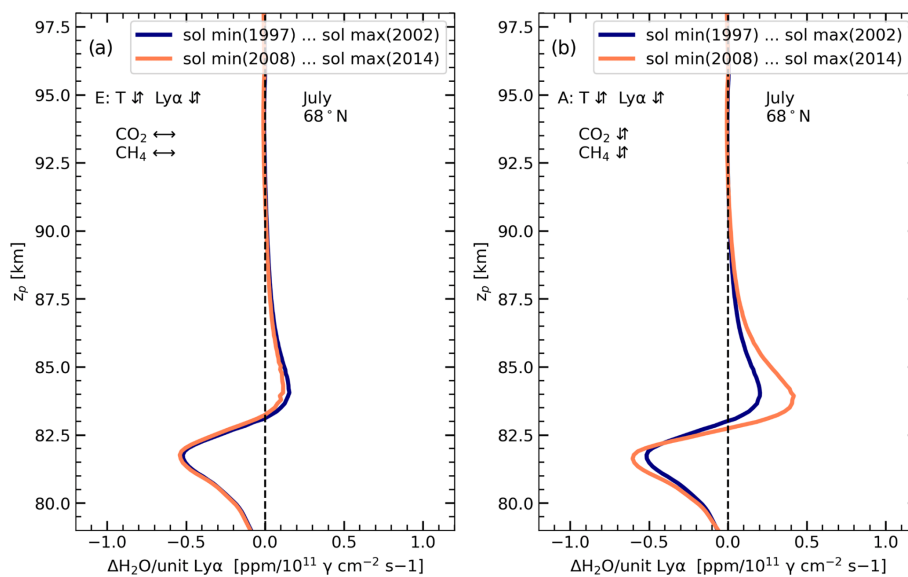


**Figure 6.** H<sub>2</sub>O response per unit Ly $\alpha$  variations in July at 68° N during the years between solar minimum and maximum in the early (1997–2002) and late (2008–2014) periods. **(a)** MIMAS model run E with constant CO<sub>2</sub> and CH<sub>4</sub>. **(b)** MIMAS model run A with varying CO<sub>2</sub> and CH<sub>4</sub>.

Ly $\alpha$  radiance has already exceeded the peak value of the previous solar cycle 24.

## 5 Missing H<sub>2</sub>O–solar-cycle response

A recent study by Hervig et al. (2019) reported a missing response in H<sub>2</sub>O concentration to the solar cycle after 2005. In Fig. 8, we compare our model results of H<sub>2</sub>O anomaly with the satellite observations. The H<sub>2</sub>O response is averaged over the geometric altitudes of 80–85 km at 68° N. For this comparison, we used MIMAS run A, where the increasing concentration of GHG is considered. The satellite observations are shown in Fig. 8 from HALOE, SOFIE, and MLS according to Hervig et al. (2019). HALOE shows a strong negative response to Ly $\alpha$  (−1.7 ppmv per solar cycle) during period 1, but in SOFIE and MLS, the response is almost absent (+0.2 ppmv per solar cycle) during period 2 (Hervig et al., 2019). For MIMAS, no clear H<sub>2</sub>O–solar-cycle anticorrelation is noticed in the early period, but it was slightly positive in the late period, in agreement with SOFIE and MLS satellite observations. To investigate the H<sub>2</sub>O response to Ly $\alpha$  variation in more detail, we analysed the vertical H<sub>2</sub>O response profile at geometric altitudes similar to the satellite observations.

Figure 9 shows the vertical profile of H<sub>2</sub>O response in geometric altitudes for the model run with constant GHGs (run E, Fig. 9a) and growing GHGs (run A, Fig. 9b). The magnitude of the H<sub>2</sub>O response at geometric altitudes (Fig. 9) differs from that at pressure altitudes (Fig. 7). This is because the geometric altitude of constant pressure levels is not constant and varies throughout the solar cycle but also with

time due to increasing GHGs. Therefore, the magnitude of the H<sub>2</sub>O response differs when converted from pressure altitudes to geometric altitudes.

We focus on the 80–85 km geometric altitude range (Fig. 9, shaded region). There are positive and negative H<sub>2</sub>O response zones within this altitude range, similarly to Fig. 7. We calculated the average H<sub>2</sub>O response over the 80–85 km altitude range for MIMAS runs A and E, and this is given in Table 2. For the model run with growing GHGs (run A), the H<sub>2</sub>O response averaged over an altitude range of 80–85 km changed from −0.01 ppm per solar cycle in the early period to 0.10 ppm per solar cycle in the late period (see Table 2). The H<sub>2</sub>O response in the late period becomes slightly positive for run A, consistent with the satellite observations of SOFIE and MLS (see Fig. 8). The vertical profile of the H<sub>2</sub>O–solar-cycle response clearly shows that H<sub>2</sub>O response to the solar cycle is not completely missing in the late period. The missing response in the MIMAS H<sub>2</sub>O, as shown in Fig. 8, occurred when averaging over the 80–85 km altitude range. Figure 9 demonstrates that the H<sub>2</sub>O response shows nearly equal positive and negative responses within the 80–85 km altitude range (shaded region). Therefore, averaging the response in this altitude range becomes nearly zero as the positive and negative responses cancel out each other. When averaging over the altitude range of 80–82 km in the early period, we receive an H<sub>2</sub>O response of −0.71 ppm per solar cycle and an anti-correlation between H<sub>2</sub>O and Ly $\alpha$ . The results clearly show that the small solar cycle response in MIMAS is a consequence of averaging over an altitude range of 80–85 km. It suggests that averaging H<sub>2</sub>O response over an altitude range containing positive and negative responses

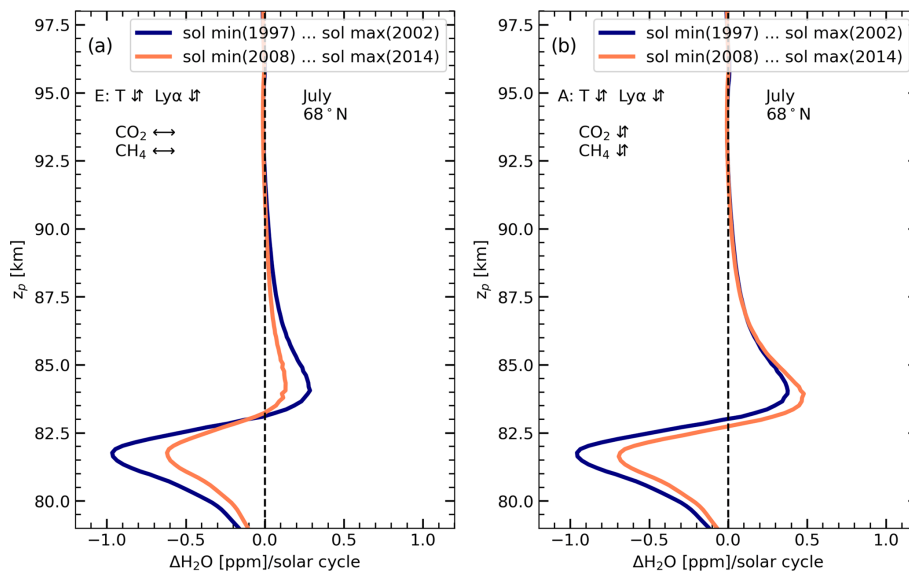


**Figure 7.** H<sub>2</sub>O response to absolute solar cycle Ly $\alpha$  variations in July at 68° N during the years between solar minimum and maximum in the early (1997–2002) and late (2008–2014) periods. **(a)** MIMAS model run E with constant CO<sub>2</sub> and CH<sub>4</sub>. **(b)** MIMAS model run A with varying CO<sub>2</sub> and CH<sub>4</sub>.

**Table 2.** The solar cycle H<sub>2</sub>O response averaged over 80–85 km geometric altitude at 68° N for model runs A and E.

Model run	$\Delta\text{H}_2\text{O}$ (ppm)/solar cycle (80–85km)	
	Early period	Late period
MIMAS with constant CO <sub>2</sub> and CH <sub>4</sub> (run E)	−0.11	−0.06
MIMAS with increasing CO <sub>2</sub> and CH <sub>4</sub> (run A)	−0.01	0.10

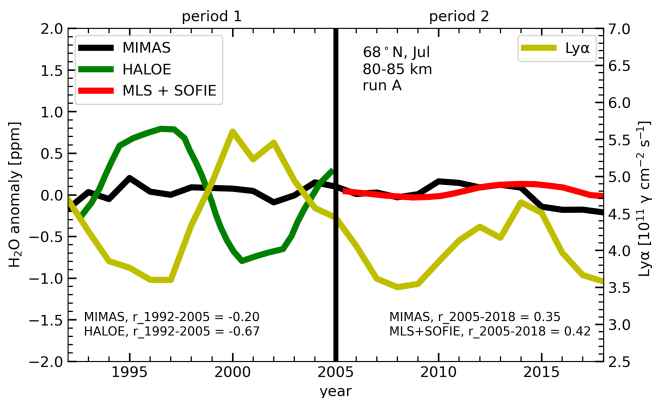


**Figure 8.** Time series of Ly $\alpha$  and H<sub>2</sub>O anomalies as monthly averages for July at 68° N for the altitude range of 80–85 km from MIMAS run A and satellites (HALOE and the composite data (MLS and SOFIE)). Satellite observations are according to Hervig et al. (2019). The H<sub>2</sub>O–Ly $\alpha$  correlation is calculated for the early and late periods (see inset).

may not provide a detailed understanding of the H<sub>2</sub>O–solar-cycle response.

## 6 Conclusions

In this study, we used our ice particle model MIMAS along with the atmospheric dynamics model LIMA to investigate the response of H<sub>2</sub>O to the solar cycle from 1992 to 2018. We investigated how NLC formation affects vertical H<sub>2</sub>O profiles by running model simulations with and without microphysics. NLC formations are shown to redistribute H<sub>2</sub>O profiles by consuming H<sub>2</sub>O from the background at ice-forming altitudes (dehydration) and releasing it at ice-sublimating altitudes (hydration), which is known as the freeze-drying effect. To investigate the missing solar cycle response in satellite observations reported by Hervig et al. (2019), we divided the entire study period into an early period (1992–2005) and a late (2005–2018) period. We first investigated how the Ly $\alpha$  variation affects the H<sub>2</sub>O profile between solar minimum and maximum in the early period. The solar Ly $\alpha$  variation affects the H<sub>2</sub>O concentration at NLC altitudes mainly in two ways: through the effect of temperature change and through the effect of photolysis. To distinguish these two effects, we performed additional model simulations with different background conditions (see Table 1). We found that the modulation of water vapour, which comes through the temperature

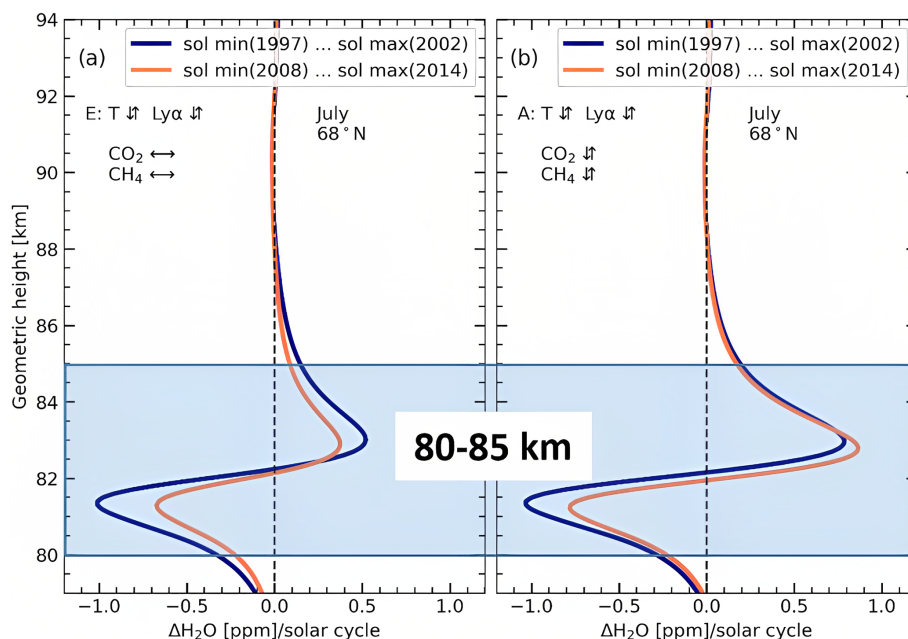


**Figure 9.** H<sub>2</sub>O response to absolute solar cycle Ly $\alpha$  variations in July at 68° N during the years between solar minimum and maximum in the early (1997–2002) and late (2008–2014) periods represented in geometric altitudes. The shaded region represents the altitude range used for calculating an average solar cycle response. (a) MIMAS model run E with constant CO<sub>2</sub> and CH<sub>4</sub>. (b) MIMAS model run A with varying CO<sub>2</sub> and CH<sub>4</sub>.

changes with the solar cycle, causes a slight positive H<sub>2</sub>O response at ice-forming altitudes and a negative response at ice-sublimating altitudes. The solar cycle photolysis effect has only negative responses to the H<sub>2</sub>O profile, and this response dominates at ice sublimation altitudes with NLC conditions. Our results for the case of photolysis effect only are supported by previous simulations, which also suggest that freeze drying significantly reduces the potential effect of Ly $\alpha$  photolysis on H<sub>2</sub>O above 82 km, while the effect is enhanced at 80–82 km, where ice particles sublimate (von Zahn et al., 2004; Lübken et al., 2009).

To the best of our knowledge, we have for the first time identified a positive response of water vapour to Ly $\alpha$  variation in the MLT region, which is due to microphysical processes. It was assumed for a long time that water vapour only anti-correlates with the solar cycle at mesopause altitudes (e.g. Sonnemann and Grygalashvily, 2005, and references therein). We should note that, in the Martian atmosphere where microphysical processes play a crucial role in water vapour distributions through the entire atmosphere in all seasons (e.g. Shaposhnikov et al., 2018), this effect may be important.

We have made a comparison between the model and satellite observations of the H<sub>2</sub>O response to the solar cycle averaged over an altitude range of 80–85 km. The satellite observations from HALOE show a strong anti-correlation with the solar cycle in the early period, but the model shows a very small response in both the early and late periods. The vertical

H<sub>2</sub>O response profiles from MIMAS show that, within the 80–85 km altitude range, the positive and negative responses are almost equal in magnitude and symmetric. Therefore, averaging the response over this altitude range reduces the overall response in the model as positive and negative responses cancel each other out.

We also investigated the role of increasing GHGs in the H<sub>2</sub>O–solar-cycle response. From the early to the late period, there are mainly two factors that affect the long-term H<sub>2</sub>O solar cycle response: increasing CO<sub>2</sub> and CH<sub>4</sub> concentrations and the lower intensity of the solar cycle (see Fig. 2). We found that increasing GHG concentration increased the H<sub>2</sub>O response to Ly $\alpha$ . The Ly $\alpha$  intensity during the late solar maximum decreased by 40 % compared to during the early solar maximum. Therefore, the overall response of H<sub>2</sub>O to the solar cycle is also decreased in the late period. It should be noted that our results have limitations as they use constant dynamics for all years. We are looking forward to a new gravity-wave-resolving model for the investigation of the effects on changing dynamics due to changing GHGs and solar activity.

*Data availability.* The satellite data shown in this paper are reproduced from the paper by Hervig et al. (2019). Lyman- $\alpha$  data are available at <https://doi.org/10.25980/ZR1T-6Y72> (Machol et al., 2023) from LASP. The data utilized in this paper can be downloaded from <https://www.radar-service.eu/radar/en/dataset/>

ArvFyujQbPGYfRqv?token=UEOfafmhOFFfWBRKONmZ  
(<https://doi.org/10.22000/1068>).

*Author contributions.* FJL and GB designed the study. MG carried out LIMA model simulations. AV conducted MIMAS model simulations and wrote the first draft of the paper. AV, GB, MG, and FJL interpreted the results and contributed significantly to the interpretation and improvement of the paper. All authors discussed the results and commented on the work.

*Competing interests.* The contact author has declared that none of the authors has any competing interests.

*Disclaimer.* Publisher's note: Copernicus Publications remains neutral with regard to jurisdiction claims in published maps and institutional affiliations.

*Special issue statement.* This article is part of the special issue "Special issue on the joint 20th International EISCAT Symposium and 15th International Workshop on Layered Phenomena in the Mesopause Region". It is a result of the Joint 20th International EISCAT Symposium 2022 and 15th International Workshop on Layered Phenomena in the Mesopause Region, Eskilstuna, Sweden, 15–19 August 2022.

*Acknowledgements.* We acknowledge the Mauna Loa records for CO<sub>2</sub> and CH<sub>4</sub> from <http://www.esrl.noaa.gov/gmd/ccgg/>, last access: 14 January 2023. This paper is partly supported by the TIMA project of the BMBF research initiative ROMIC.

*Financial support.* This research has been supported by the Bundesministerium für Bildung und Forschung (grant no. 01LG1902A).

The publication of this article was funded by the Open Access Fund of the Leibniz Association.

*Review statement.* This paper was edited by Andrew J. Kavanagh and reviewed by two anonymous referees.

## References

Bardeen, C. G., Toon, O. B., Jensen, E. J., Harvig, M. E., Randall, C. E., Benze, S., Marsh, D. R., and Merkel, A.: Numerical simulations of the three-dimensional distribution of polar mesospheric clouds and comparisons with Cloud Imaging and Particle Size (CIPS) experiment and the Solar Occultation For Ice Experiment (SOFIE) observations, *J. Geophys. Res.*, 115, D10204, <https://doi.org/10.1029/2009JD012451>, 2010.

- Berger, U. and Lübken, F. J.: Mesospheric temperature trends at mid-latitudes in summer, *Geophys. Res. Lett.*, 38, L22804, <https://doi.org/10.1029/2011GL049528>, 2011.
- Berger, U. and Lübken, F. J.: Trends in mesospheric ice layers in the Northern Hemisphere during 1961–2013, *J. Geophys. Res.*, 120, 11277–11298, <https://doi.org/10.1002/2015JD023355>, 2015.
- Berger, U. and von Zahn, U.: Icy particles in the summer mesopause region: Three-dimensional modeling of their environment and two-dimensional modeling of their transport, *J. Geophys. Res.-Space*, 107, SIA 10-1–SIA 10-32, <https://doi.org/10.1029/2001JA000316>, 2002.
- Berger, U.: Modeling of middle atmosphere dynamics with LIMA, *J. Atmos. Sol.-Terr. Phys.*, 70, 1170–1200, <https://doi.org/10.1016/j.jastp.2008.02.004>, 2008.
- Brasseur, G. and Solomon, S.: *Aeronomy of the Middle Atmosphere: Chemistry and Physics of the Stratosphere and Mesosphere*, Atmospheric and Oceanographic Sciences Library, Springer Netherlands, <https://books.google.nl/books?id=HoV1VNFJwVwC> (last access: 5 January 2023), 2005.
- Compo, G. P., Whitaker, J. S., Sardeshmukh, P. D., Matsui, N., Allan, R. J., Yin, X., Gleason, B. E., Vose, R. S., Rutledge, G., Bessemoulin, P., BroNnimann, S., Brunet, M., Crouthamel, R. I., Grant, A. N., Groisman, P. Y., Jones, P. D., Kruk, M. C., Kruger, A. C., Marshall, G. J., Maugeri, M., Mok, H. Y., Nordli, O., Ross, T. F., Trigo, R. M., Wang, X. L., Woodruff, S. D., and Worley, S. J.: The twentieth century reanalysis project, *Q. J. Roy. Meteor. Soc.*, 137, 1–28, <https://doi.org/10.1002/qj.776>, 2011.
- DeLand, M. T. and Thomas, G. E.: Updated PMC trends derived from SBUV data, *J. Geophys. Res.*, 120, 2140–2166, <https://doi.org/10.1002/2014JD022253>, 2015.
- DeLand, M. T. and Thomas, G. E.: Evaluation of Space Traffic Effects in SBUV Polar Mesospheric Cloud Data, *Jo. Geophys. Res.-Atmos.*, 124, 4203–4221, <https://doi.org/10.1029/2018JD029756>, 2019.
- DeLand, M. T., Shettle, E. P., Thomas, G. E., and Olivero, J. J.: Solar backscattered ultraviolet (SBUV) observations of polar mesospheric clouds (PMCs) over two solar cycles, *J. Geophys. Res.-Atmos.*, 108, 8445, <https://doi.org/10.1029/2002jd002398>, 2003.
- DeLand, M. T., Shettle, E. P., Thomas, G. E., and Olivero, J. J.: A quarter-century of satellite polar mesospheric cloud observations, *J. Atmos. Sol.-Terr. Phys.*, 68, 9–29, <https://doi.org/10.1016/J.JASTP.2005.08.003>, 2006.
- Fiedler, J., Baumgarten, G., Berger, U., Hoffmann, P., Käßler, N., and Lübken, F. J.: NLC and the background atmosphere above ALOMAR, *Atmos. Chem. Phys.*, 11, 5701–5717, <https://doi.org/10.5194/acp-11-5701-2011>, 2011.
- Gadsden, M. and Schröder, W.: Noctilucent Clouds, *Journal of the British Astronomical Association*, 99, 210–214, ISBN: 3540506853, 1989.
- Garcia, R. R.: Dynamics, Radiation, and Photochemistry in the Mesosphere' Implications for the Formation of Noctilucent Clouds, *J. Geophys. Res.*, 94, 14605–14615, <https://doi.org/10.1029/JD094iD12p14605>, 1989.
- Garcia, R. R., Marsh, D. R., Kinnison, D. E., Boville, B. A., and Sassi, F.: Simulation of secular trends in the middle atmosphere, 1950–2003, *J. Geophys. Res.-Atmos.*, 112, D09301, <https://doi.org/10.1029/2006JD007485>, 2007.
- Hartogh, P., Sonnemann, G. R., Grygalashvyly, M., Song, L., Berger, U., and Lübken, F.-J.: Water vapor measure-

- ments at ALOMAR over a solar cycle compared with model calculations by LIMA, *J. Geophys. Res.*, 114, D00117, <https://doi.org/10.1029/2009jd012364>, 2010.
- Hervig, M. E., Berger, U., and Siskind, D. E.: Decadal variability in PMCs and implications for changing temperature and water vapor in the upper mesosphere, *J. Geophys. Res.*, 121, 2383–2392, <https://doi.org/10.1002/2015JD024439>, 2016.
- Hervig, M., McHugh, M., and Summers, M. E.: Water vapor enhancement in the polar summer mesosphere and its relationship to polar mesospheric clouds, *Geophys. Res. Lett.*, 30, 2041, <https://doi.org/10.1029/2003GL018089>, 2003.
- Hervig, M. E., Siskind, D. E., Bailey, S. M., and Russell, J. M.: The influence of PMCs on water vapor and drivers behind PMC variability from SOFIE observations, *J. Atmos. Sol.-Terr. Phys.*, 132, 124–134, <https://doi.org/10.1016/j.jastp.2015.07.010>, 2015.
- Hervig, M. E., Siskind, D. E., Bailey, S. M., Merkel, A. W., DeLand, M. T., and Russell, J. M.: The Missing Solar Cycle Response of the Polar Summer Mesosphere, *Geophys. Res. Lett.*, 46, 10132–10139, <https://doi.org/10.1029/2019GL083485>, 2019.
- Karagodin-Doyennel, A., Rozanov, E., Kuchar, A., Ball, W., Arsenovic, P., Remsberg, E., Jöckel, P., Kunze, M., Plummer, D. A., Stenke, A., Marsh, D., Kinnison, D., and Peter, T.: The response of mesospheric H<sub>2</sub>O and CO to solar irradiance variability in models and observations, *Atmos. Chem. Phys.*, 21, 201–216, <https://doi.org/10.5194/acp-21-201-2021>, 2021.
- Kiliani, J.: 3-D Modeling of Noctilucent Cloud Evolution and Relationship to the Ambient Atmosphere, PhD thesis University Rostock, [https://www.iap-kborn.de/fileadmin/user\\_upload/MAIN-abteilung/optik/Forschung/Doktorarbeiten/Kiliani-Diss-2014\\_s.pdf](https://www.iap-kborn.de/fileadmin/user_upload/MAIN-abteilung/optik/Forschung/Doktorarbeiten/Kiliani-Diss-2014_s.pdf) (last access: 13 January 2023), 2014.
- Lean, J. L., Rottman, G. J., Kyle, H. L., Woods, T. N., Hickey, J. R., and Puga, L. C.: Detection and parameterization of variations in solar mid- and near-ultraviolet radiation (200–400 nm), *J. Geophys. Res.*, 102, 29939–29956, <https://doi.org/10.1029/95GL03093>, 1997.
- Lübken, F. J., Berger, U., and Baumgarten, G.: Stratospheric and solar cycle effects on long-term variability of mesospheric ice clouds, *J. Geophys. Res.-Atmos.*, 114, D00106, <https://doi.org/10.1029/2009JD012377>, 2009.
- Lübken, F. J., Berger, U., and Baumgarten, G.: Temperature trends in the midlatitude summer mesosphere, *J. Geophys. Res.-Atmos.*, 118, 13347–13360, <https://doi.org/10.1002/2013JD020576>, 2013.
- Lübken, F. J., Berger, U., and Baumgarten, G.: On the Anthropogenic Impact on Long-Term Evolution of Noctilucent Clouds, *Geophys. Res. Lett.*, 45, 6681–6689, <https://doi.org/10.1029/2018GL077719>, 2018.
- Lübken, F. J., Baumgarten, G., and Berger, U.: Long term trends of mesospheric ice layers: A model study, *J. Atmos. Sol.-Terr. Phys.*, 214, 105378, <https://doi.org/10.1016/j.jastp.2020.105378>, 2021.
- Machol, J., Snow, M., Woodraska, D., Woods, T., Viereck, R., and Coddington, O.: An Improved Lyman-Alpha Composite, *Earth Space Sci.*, 6, 2263–2272, <https://doi.org/10.1029/2019EA000648>, 2019.
- Machol, J., Woodraska, D., and Woods, T.: Composite Solar Lyman-alpha, University of Colorado, Laboratory for Atmospheric and Space Physics [data set], <https://doi.org/10.25980/ZR1T-6Y72>, 2023.
- Marsh, D. R., Mills, M. J., Kinnison, D. E., Lamarque, J. F., Calvo, N., and Polvani, L. M.: Climate change from 1850 to 2005 simulated in CESM1(WACCM), *J. Clim.*, 26, 7372–7391, <https://doi.org/10.1175/JCLI-D-12-00558.1>, 2013.
- Roble, R. G. and Dickinson, R. E.: How will changes in carbon dioxide and methane modify the mean structure of the mesosphere and thermosphere?, *Geophys. Res. Lett.*, 16, 1441–1444, <https://doi.org/10.1029/GL016i012p01441>, 1989.
- Shaposhnikov, D. S., Rodin, A. V., Medvedev, A. S., Fedorova, A. A., Kuroda, T., and Hartogh, P.: Modeling the Hydrological Cycle in the Atmosphere of Mars: Influence of a Bimodal Size Distribution of Aerosol Nucleation Particles, *J. Geophys. Res.-Planet.*, 123, 508–526, <https://doi.org/10.1002/2017JE005384>, 2018.
- Shettle, E. P., DeLand, M. T., Thomas, G. E., and Olivero, J. J.: Long term variations in the frequency of polar mesospheric clouds in the Northern Hemisphere from SBUV, *Geophys. Res. Lett.*, 36, L02803, <https://doi.org/10.1029/2008GL036048>, 2009.
- Siskind, D. E., Stevens, M. H., Hervig, M. E., and Randall, C. E.: Recent observations of high mass density polar mesospheric clouds: A link to space traffic?, *Geophys. Res. Lett.*, 40, 2813–2817, <https://doi.org/10.1002/grl.50540>, 2013.
- Sonnemann, G. R. and Grygalashvyly, M.: Solar influence on mesospheric water vapor with impact on NLCs, *J. Atmos. Sol.-Terr. Phys.*, 67, 177–190, <https://doi.org/10.1016/j.jastp.2004.07.026>, 2005.
- Thomas, G. E. and Olivero, J.: Noctilucent clouds as possible indicators of global change in the mesosphere, *Adv. Space Res.*, 28, 937–946, [https://doi.org/10.1016/S0273-1177\(01\)80021-1](https://doi.org/10.1016/S0273-1177(01)80021-1), 2001.
- Thomas, G. E.: Is the polar mesosphere the miner's canary of global change?, *Adv. Space Res.*, 18, 149–152, 1996.
- von Zahn, U. and Berger, U.: Persistent ice cloud in the midsummer upper mesosphere at high latitudes: Three-dimensional modeling and cloud interactions with ambient water vapor, *J. Geophys. Res.-Atmos.*, 108, 8451, <https://doi.org/10.1029/2002jd002409>, 2003.
- von Zahn, U., Baumgarten, G., Berger, U., Fiedler, J., and Hartogh, P.: Noctilucent clouds and the mesospheric water vapour: the past decade, *Atmos. Chem. Phys.*, 4, 2449–2464, <https://doi.org/10.5194/acp-4-2449-2004>, 2004.
- Woods, T. N., Tobiska, W. K., Rottman, G. J., and Worden, J. R.: Improved solar Lyman  $\alpha$  irradiance modeling from 1947 through 1999 based on UARS observations, *J. Geophys. Res.-Space Phys.*, 105, 27195–27215, <https://doi.org/10.1029/2000ja000051>, 2000.



## Appendix B

# Vellalassery et al., 2024

Ashique Vellalassery et al. (2024). "Long-Term Evolution in Noctilucent Clouds' Response to the Solar Cycle: A Model-Based Study". In: *Atmosphere* 15.1. ISSN: 20734433. DOI: 10.3390/atmos15010088



## Article

# Long-Term Evolution in Noctilucent Clouds' Response to the Solar Cycle: A Model-Based Study

Ashique Vellalassery \*, Gerd Baumgarten, Mykhaylo Grygalashvyly  and Franz-Josef Lübken

Leibniz Institute of Atmospheric Physics, University of Rostock, Schloßstraße 6, D-18225 Kühlungsborn, Germany; baumgarten@iap-kborn.de (G.B.); luebken@iap-kborn.de (F.-J.L.)

\* Correspondence: ashique@iap-kborn.de

**Abstract:** Noctilucent clouds (NLC) are sensitive indicators in the upper mesosphere, reflecting changes in the background atmosphere. Studying NLC responses to the solar cycle is important for understanding solar-induced changes and assessing long-term climate trends in the upper mesosphere. Additionally, it enhances our understanding of how increases in greenhouse gas concentration in the atmosphere impact the Earth's upper mesosphere and climate. This study presents long-term trends in the response of NLC and the background atmosphere to the 11-year solar cycle variations. We utilised model simulations from the Leibniz Institute Middle Atmosphere (LIMA) and the Mesospheric Ice Microphysics and Transport (MIMAS) over 170 years (1849 to 2019), covering 15 solar cycles. Background temperature and water vapour (H<sub>2</sub>O) exhibit an apparent response to the solar cycle, with an enhancement post-1960, followed by an acceleration of greenhouse gas concentrations. NLC properties, such as maximum brightness ( $\beta_{\max}$ ), calculated as the maximum backscatter coefficient, altitude of  $\beta_{\max}$  (referred to as NLC altitude) and ice water content (IWC), show responses to solar cycle variations that increase over time. This increase is primarily due to an increase in background water vapour concentration caused by an increase in methane (CH<sub>4</sub>). The NLC altitude positively responds to the solar cycle mainly due to solar cycle-induced temperature changes. The response of NLC properties to the solar cycle varies with latitude, with most NLC properties showing larger and similar responses at higher latitudes (69° N and 78° N) than mid-latitudes (58° N).

**Keywords:** noctilucent clouds; solar cycle; greenhouse gases; mesosphere; water vapour



**Citation:** Vellalassery, A.; Baumgarten, G.; Grygalashvyly, M.; Lübken, F.-J. Long-Term Evolution in Noctilucent Clouds' Response to the Solar Cycle: A Model-Based Study. *Atmosphere* **2024**, *15*, 88. <https://doi.org/10.3390/atmos15010088>

Academic Editor: Yuichi Otsuka

Received: 22 November 2023

Revised: 25 December 2023

Accepted: 4 January 2024

Published: 9 January 2024



**Copyright:** © 2024 by the authors. Licensee MDPI, Basel, Switzerland. This article is an open access article distributed under the terms and conditions of the Creative Commons Attribution (CC BY) license (<https://creativecommons.org/licenses/by/4.0/>).

## 1. Introduction

Noctilucent clouds (NLC), consisting of tiny ice particles, form about 80–85 km above the Earth's surface and are the highest atmospheric clouds. These clouds typically form in the summer when temperatures in the mesopause region are very low, especially at middle and polar latitudes [1,2]. NLC are rare, having only been observed in modern times since the end of the 19th century [3]. By studying NLC, we can gain insight into changes in the upper mesosphere and their potential implications for climate research [4–9]. The formation of NLC is a complex process that depends on several factors, including background temperature and water vapour [6,10]. When the temperature in the mesosphere falls below the freezing point of water (~150 K), water vapour can condense and form ice particles, which are the building blocks of NLC. In general, the combination of low background temperatures and sufficient water vapour concentrations creates favourable conditions for forming NLC [1,3,4].

The 11-year solar cycle is one of the factors that can influence mesospheric temperature and water vapour and thereby affect the formation and properties of NLC [11,12]. It is important to understand how the solar cycle relates to the characteristics of NLC to study how they behave and affect the upper atmosphere. Numerous studies have been conducted on the relationship between the 11-year solar cycle and the properties of NLC (e.g., [8,13–16]). Satellite observations and model simulations are used to investigate the effects of the solar

cycle on the background atmosphere and their impacts on NLC properties. A positive correlation exists between the solar Lyman-alpha ( $\text{Ly}\alpha$ ) flux and the background temperature at NLC altitudes. Depending on the altitude, the correlation can be positive or negative for water vapour [17]. Studies have shown a clear anti-correlation between the solar cycle  $\text{Ly}\alpha$  and ice water content (IWC) during solar cycles 22 and 23, but it decreases during the recent solar cycle 24 [13,17]. Our previous study [17] found a clear anti-correlation between  $\text{Ly}\alpha$  flux and IWC in the model and satellite observations for solar cycles 22 and 23, which becomes weaker in solar cycle 24. Moreover, the magnitude of the solar cycle-induced IWC variations in Solar Backscatter Ultraviolet (SBUV) and Halogen Occultation Experiment (HALOE) satellite observations is the same as the IWC variations in the MIMAS model. The study showed that the reduced IWC response during solar cycle 24 is due to the reduced variation of  $\text{Ly}\alpha$  during this particular solar cycle.

The observational data available for NLC trends are still quite limited, and little is known about long-term trends and episodic changes in the background atmosphere at NLC altitudes [7,9,11,18]. Therefore, there needs to be detailed studies or sufficient information on the long-term evolution of the solar cycle response of NLC. Model simulations are valuable tools to help us learn more about the changes in the NLC and the surrounding atmosphere [19]. Long-term simulations of NLC by the MIMAS model from 1849 to 2019 are promising for studying solar cycle trends (covering 15 complete solar cycles) in the NLC, as the model uses the solar  $\text{Ly}\alpha$  flux as a proxy for solar irradiance [9,20]. Therefore, by using the MIMAS model, the response of NLC properties to the solar cycle, such as ice particle radius, IWC, the backscatter coefficient at a wavelength of 532 nm ( $\beta$ , from now on referred to NLC brightness) and NLC altitude, can be studied over a longer period, which is not possible with satellite observations due to measurement limitations. There are studies [9,20] using the MIMAS model regarding the long-term trends in NLC and the effects of increasing greenhouse gases ( $\text{CO}_2$  and  $\text{CH}_4$ ) from 1871 to 2008. The results show that some ice parameters' time series significantly modulate with the solar cycle (see Figure 3 in [9]). Since those studies aimed to investigate long-term trends in NLC, the effects of solar cycle variation on NLC were excluded by averaging over half a solar cycle [20].

In this study, we mainly focus on the impact of the 11-year solar cycle variation on the properties of NLC during the period 1855–2019, relying on the model simulations used in previous studies [9,20]. Compared to previous studies, this study includes an analysis of long-term trends in the vertical distribution profiles of the background atmosphere, including temperature and water vapour with and without NLC. In addition, we examine trends in the vertical distributions of NLC properties that have not been explored before, such as the number and radius of ice particles and NLC brightness. This paper aims to address the following questions: (1) How do background temperature and water vapour respond to the solar cycle, and what are the trends in their solar cycle response? (2) What are the long-term trends in the vertical distribution of NLC properties? How do solar cycle modulations influence them? (3) Which NLC properties are influenced by the 11-year solar cycle, and how strongly are they influenced? (4) What influence does the long-term increase in greenhouse gases have on the response of NLC properties to the solar cycle? (5) Is the response of NLC properties to the solar cycle dependent on latitude, and how strong? The following section briefly discusses the models used in this study. Section 3 presents the results and discussion on the trends in the response of the background atmosphere and NLC properties to the solar cycle, as well as the trends in their response to the solar cycle under the influence of increasing greenhouse gases and for different latitudes. The summary of our findings is provided in Section 4.

## 2. Model Description

Here, we only provide a brief description of the model setup, as a comprehensive explanation of our modelling framework has already been discussed in detail in various publications [9,20–23]. The overall model framework combines two models, namely the

Leibniz Institute Middle Atmosphere (LIMA) model and the Mesospheric Ice Microphysics and Transport (MIMAS) model. The basic idea of this modelling framework is to use LIMA to model the background atmosphere under Northern Hemisphere conditions and then use this background information in the MIMAS model to calculate the properties of NLC (see Figure 1 in [20]). LIMA and MIMAS use daily Ly $\alpha$  data from the LASP Interactive Solar Irradiance Data Center (LISIRD) as a representative measure of solar activity from 1961 to 2019 [24]. Before 1961, monthly sunspot numbers approximated Ly $\alpha$  values. In LIMA, variations in Ly $\alpha$  flux account for atmospheric temperature variations, while in MIMAS, changes in Ly $\alpha$  flux cause photolysis of H<sub>2</sub>O.

LIMA is a global model that covers the altitude range from 0 to 150 km and includes key processes such as radiation, chemistry and transport [12,22]. At lower altitudes (0–28 km), LIMA is nudged to the twentieth-century reanalysis data from NOAA-CIRES (National Oceanic and Atmospheric Administration–Cooperative Institute for Research in Environmental Sciences 20CR; [25]). In LIMA, the mixing ratios of ozone (28–65 km) and carbon dioxide (28–150 km) change, whereas all other trace gases are constant. We consider temporal and latitudinal fluctuations in the stratosphere and lower mesosphere for ozone from 1961 to 2008 [12,26]. Before 1961, stratospheric ozone was kept constant (according to 1961). The model's carbon dioxide (CO<sub>2</sub>) concentration is based on a monthly average time series from 1961 to 2019 measured at Mauna Loa (19° N, 155° W). Before 1961, historical CO<sub>2</sub> data from Antarctic ice cores were used [27]. In LIMA, the influence of small-scale internal gravity waves is accounted for by a non-linear spectral gravity wave parameterisation [28].

Climate change and the solar cycle most likely affect the atmospheric circulation pattern in the mesosphere, which might affect the background conditions and gravity waves (for example, [29]). Unfortunately, very little is known about the long-term effects of these changes on the dynamic, thermal and compositional characteristics of the summer mesopause region. Since considering these potential long-term impacts is highly speculative, we decided to use a specific dynamic scenario from the representative year 1976 for the entire period from 1849 to 2019. It is important to note that the conclusions from our study are not influenced by the choice of this specific year. Consequently, this study does not consider any potential influence of mean background winds and wave activity trends on NLC [9,17,20].

MIMAS is a specialised 3D Lagrangian transport model that simulates ice particles in the mesosphere and lower thermosphere (MLT) [9,17,20]. It calculates various NLC parameters from 10 May to 31 August and is restricted to mid and high latitudes (37°–90° N). The model uses a horizontal grid resolution of 1° in latitude and 3° in longitude, with a vertical resolution of 100 m, ranging from 77.8 to 94.1 km (163 levels). Below the lower boundary of MIMAS, two factors determine the mixing ratio of H<sub>2</sub>O in the stratosphere: first, the transport of H<sub>2</sub>O from the troposphere and second, the oxidation of methane (CH<sub>4</sub>), where each CH<sub>4</sub> molecule produces two H<sub>2</sub>O molecules. Through photochemical processes, methane almost entirely converts into H<sub>2</sub>O in the mesosphere [9]. MIMAS assumes a constant transport rate from the troposphere. Therefore, the increase in H<sub>2</sub>O occurs mainly through methane oxidation. Therefore, we parameterise H<sub>2</sub>O as a function of CH<sub>4</sub>, following the approach proposed by [9]. Please note that H<sub>2</sub>O sources and sinks due to chemical reactions are not accounted for in MIMAS, which may lead to uncertainties in the model-calculated H<sub>2</sub>O concentrations. The time series of CH<sub>4</sub> and CO<sub>2</sub> used in the model simulations are shown in Figure 1. MIMAS contains about 40 million dust particles that can serve as condensation nuclei. These dust particles originate from meteors evaporating in the atmosphere (for more information, see [21,30]). Subsequently, these particles are coated with ice in regions where H<sub>2</sub>O is supersaturated and transported by three-dimensional and time-dependent background winds, eddy diffusion and sedimentation. Standard microphysical processes, including the Kelvin effect, determine the nucleation and growth of ice particles in MIMAS [4]. Please keep in mind that there are possible uncertainties

regarding the number of dust particles available for condensation, as the accurate count of dust particles generated from evaporating meteorites is not available.

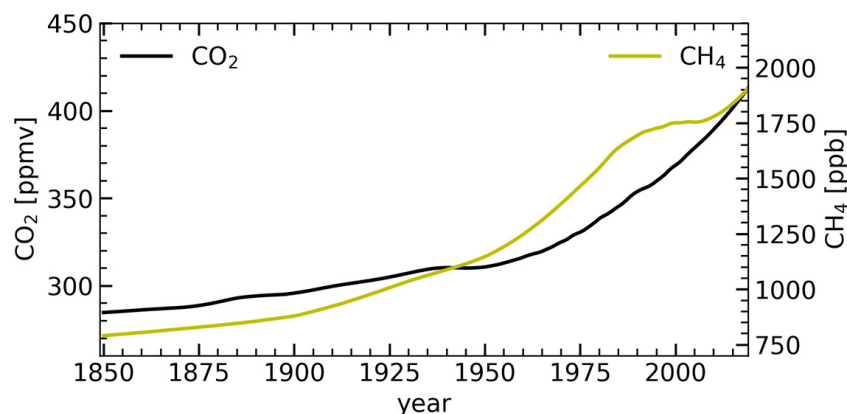


**Figure 1.** Time series of CO<sub>2</sub> and CH<sub>4</sub> concentrations (1849–2019) used in model runs.

This study uses three model runs: A, B and C. In run A, we increase both CO<sub>2</sub> and CH<sub>4</sub> (H<sub>2</sub>O). In run B, only the CO<sub>2</sub> concentration increases, while the CH<sub>4</sub> concentration remains constant. In run C, the CH<sub>4</sub> concentration increases while the CO<sub>2</sub> concentration is constant. In this paper, the following symbols refer to these scenarios: CO<sub>2</sub>↑, CH<sub>4</sub>↑ for run A; CO<sub>2</sub>↑, CH<sub>4</sub>↔ for run B; and CO<sub>2</sub>↔, CH<sub>4</sub>↑ for run C. MIMAS output has a horizontal resolution of 120 longitude bands (0°–360°) and 53 latitude bands (each 1° from 38° N to 90° N). This study focuses on three latitudes in July: 58 ± 3° N (referred to as “mid”), 69 ± 3° N (referred to as “high”) and 78 ± 3° N (referred to as “arctic”).

### 3. Results and Discussion

#### 3.1. Solar Cycle Effects on Background Temperature

We studied the impact of CO<sub>2</sub> increases and solar cycle variations on the vertical distribution of temperatures for 1849–2019. The time series of the temperature profiles (Figure 2) shows that the profiles shift downwards over time.

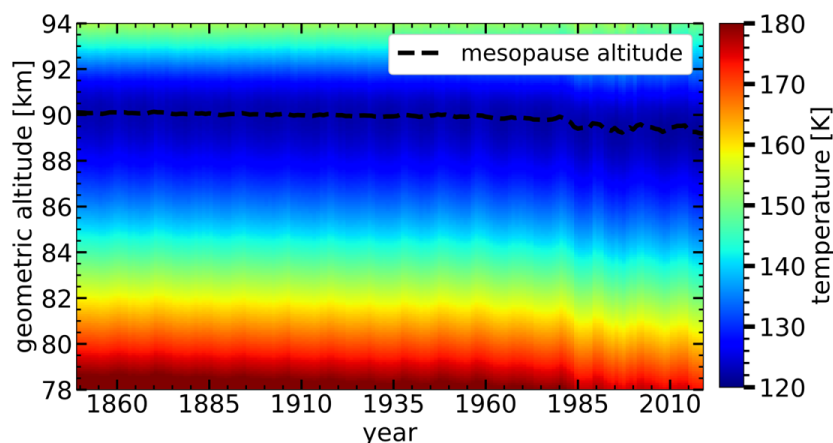


**Figure 2.** Time series of temperature profiles zonally averaged at 69° N latitude for July as a function of geometric altitude.

This shift in profiles is due to atmospheric shrinking resulting from the cooling of the middle atmosphere by increasing CO<sub>2</sub> [9,20]. Reference [9] examined the temperature trends for a fixed geometric altitude and a fixed pressure level (see Figure 1b in [9]). The temperature has decreased by 7 K since 1871 for a fixed altitude of 83 km but not significantly for a fixed pressure level. An increase in CO<sub>2</sub> leads to a decrease in temperature in the stratosphere and lower mesosphere, mainly due to enhanced cooling by

CO<sub>2</sub> [12,23,31–33]. At NLC altitudes, this cooling leads to an altitude decrease in pressure levels because the atmosphere in the lower and middle mesosphere shrinks due to CO<sub>2</sub> cooling, referred to as the “shrinking effect”. The negative temperature lapse rate at NLC altitudes causes the apparent cooling at geometric altitudes. The temperature decline at 83 km altitude accelerated after 1960, with the slope of the temperature trend line for the period 1960–2008 ( $m_1$ ) being ~6 times larger than the slope of the temperature trend line for the period 1871–1960 ( $m_2$ ), due to an accelerated CO<sub>2</sub> increase. Temperature trends calculated by LIMA are consistent with observations near 45° N latitude in summer, with a cooling trend of 3 K/decade from 1979–1997 (see Figure 10 in [34] vs. Figure 1b in [23]).

The time series of the vertical temperature profiles clearly show the influence of the solar cycle on the background temperature at all altitudes and reveal distinct 11-year patterns in the profiles (Figure 2). During solar maximum, the increase in solar irradiance leads to greater absorption of solar radiation in the MLT region by molecular oxygen and water vapour, heating the background atmosphere. The temperature differences of 0.5 K–2 K observed between solar maximum and minimum at NLC altitudes depend on solar cycle intensity and altitude [17]. The temperature difference decreases at lower altitudes as the intensity of solar radiation decreases due to atmospheric absorption [17]. In summary, the results suggest that increasing CO<sub>2</sub> and solar cycle variations significantly impact temperature profiles in the mesosphere and lower thermosphere.

### 3.2. Solar Cycle Effects on Background Water Vapour

The presence of water vapour in the upper atmosphere is mainly responsible for forming NLC. NLC are created when microscopic particles in the atmosphere, such as dust or debris, function as a surface for condensing water vapour. The saturation ratio of air with water vapour is defined as  $S = P_{H_2O}/P_{ice}$ , where  $P_{H_2O}$  is the H<sub>2</sub>O partial pressure ( $C_{H_2O} * P$ ), and  $P_{ice}$  is the saturation vapour pressure over a plane ice surface ( $C_{H_2O}$  is the water vapour mixing ratio). An environment with value  $S > 1$  is supersaturated, meaning ice particles can grow under these conditions, while  $S < 1$  is subsaturated and leads to ice particle sublimation. The formation of NLC involves the removal of water vapour from the background atmosphere, known as the “freeze-drying effect”, and the release of H<sub>2</sub>O at altitudes where NLC sublimates. Regarding trends of water vapour in the middle atmosphere, there is no clear picture, even on decadal time scales [9,18]. There are few studies of water vapour trends in the mid-latitude summer mesopause region. Observations from the Solar Occultation For Ice Experiment (SOFIE) onboard NASA’s Aeronomy of Ice in the Mesosphere (AIM) satellite (Figure 6d in [35]) show that the H<sub>2</sub>O mixing ratio has been around four parts per million volume (ppmv) in recent years, which is in agreement with MIMAS as shown in Figure 1c (run A) in [9]. The recent study by [36] suggests a water vapour trend of about 5% per decade at 52.5° N and 80 km, corresponding to 0.175 ppmv per decade. This trend is consistent with trends calculated in MIMAS, which show a rate of 0.15 ppmv per decade (see Figure 1c in [9]). However, it is unfortunate that no information is available on the centennial evolution of temperatures or water vapour in the upper mesosphere [9].

To investigate the effects of NLC formation on long-term water vapour trends, we conducted model simulations with and without NLC formation while keeping the same background conditions. The time series of the vertical water vapour distribution for MIMAS runs A and C (with and without NLC) are shown in Figure 3. Without NLC, the background H<sub>2</sub>O concentration increases with time at all altitudes in both run A and run C. At higher altitudes, more water vapour became available than at the beginning of the study period. This is due to increasing CH<sub>4</sub>, which leads to more H<sub>2</sub>O molecules forming during the oxidation of CH<sub>4</sub>. The H<sub>2</sub>O enhancement in run A is slightly lower than in run C for a given geometric altitude. This is due to the increasing CO<sub>2</sub> concentration in run A, which causes atmospheric shrinking. Due to the negative H<sub>2</sub>O gradient with altitude, the downward shift in profile leads to a decrease in H<sub>2</sub>O concentration for a given geometric

altitude. Consequently, for a fixed geometric altitude, the increase in H<sub>2</sub>O background due to CH<sub>4</sub> oxidation is somewhat less pronounced in run A than in run C.

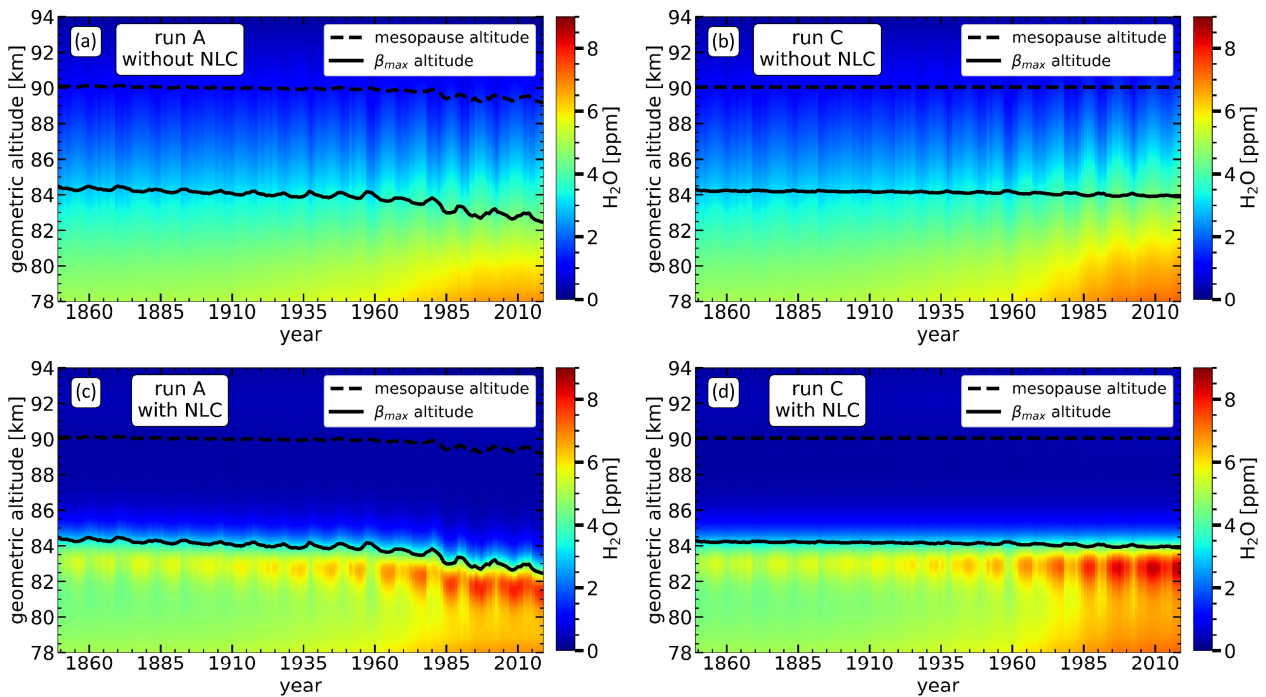


**Figure 3.** Time series of water vapour concentration as a function of geometric altitude zonally (69° N) and monthly (July) averaged for (a) Run A without NLC, (b) Run C without NLC, (c) Run A with NLC and (d) Run C with NLC.

For H<sub>2</sub>O trends without NLC (Figure 3a,b), apparent effects of the solar cycle are observed in the form of maximum and minimum at 11-year intervals. During solar maximum, the water vapour concentration decreases at all altitudes due to an enhancement in photolysis caused by an increase in Ly $\alpha$  flux. For example, during solar cycle 23, the negative response reaches its maximum at approximately 87.5 km altitude [17]. Above this altitude, the impact of photolysis diminishes due to the decreasing mixing ratio of H<sub>2</sub>O, while below this altitude, the decrease is attributed to the decreasing intensity of solar Ly $\alpha$  radiation [17]. Comparing the figures with and without NLC (Figure 3, upper vs. lower plots), the H<sub>2</sub>O profile with NLC differs from that without NLC. At NLC formation altitudes (>~83–85 km), the H<sub>2</sub>O concentration decreases due to the removal of H<sub>2</sub>O during the formation of ice particles, a phenomenon known as the “freeze-drying effect”. As a result, the highest concentrations of H<sub>2</sub>O are found at the altitudes where NLC sublimation occurs, which is approximately 1 km below the  $\beta_{\max}$  altitude (indicated by the solid black line). The enhancement in H<sub>2</sub>O concentration at the sublimation altitudes amplifies the response of H<sub>2</sub>O to the 11-year solar cycle at those altitudes. Moreover, in run A, the background H<sub>2</sub>O profiles exhibit a downward shift over time, attributed to the atmospheric shrinking caused by increasing concentration of CO<sub>2</sub>.

To investigate the long-term effects of increasing greenhouse gases on the solar cycle response of H<sub>2</sub>O, we calculated the H<sub>2</sub>O response profile with NLC for runs A and C. For this, first, we calculated the difference of H<sub>2</sub>O vertical profiles between solar maximum and minimum for two solar cycles, one at the beginning (1902–1906) and one at the end (2008–2014), which was then divided by the actual Ly $\alpha$  change between the solar maximum and minimum of the corresponding solar cycle. It provides us with the vertical profiles of water vapour response to a unit change in Ly $\alpha$  (i.e., absolute change in H<sub>2</sub>O for a unit Ly $\alpha$  change, hereafter called the H<sub>2</sub>O response profile). Figure 4 shows the H<sub>2</sub>O response profiles for runs A and C. In Figure 4a (run A), the H<sub>2</sub>O response profile shows positive and negative values depending on altitude. According to [17], the solar cycle affects the H<sub>2</sub>O

concentration in the upper mesosphere mainly in two ways: directly through the photolysis and, at the time and place of NLC formation, indirectly through temperature changes. The photolysis effect leads to an anti-correlation between the  $\text{H}_2\text{O}$  concentration and the solar  $\text{Ly}\alpha$ , even more pronounced at altitudes below  $\sim 83$  km where NLC ice particles sublimate. Above  $\sim 83$  km, where NLC form, the  $\text{H}_2\text{O}$  concentration correlates positively with solar cycle  $\text{Ly}\alpha$  variations. The reason for this positive response is that during solar maximum, the background atmosphere becomes warmer due to higher solar activity, causing relatively less ice formation compared to solar minimum. The lower ice formation rate leads to less water vapour consumption from the background atmosphere, resulting in a relatively higher  $\text{H}_2\text{O}$  concentration left in the background during solar maximum compared to solar minimum. For run C, there is no positive response of  $\text{H}_2\text{O}$  due to the constant background temperature used for all years. Comparing early and late solar cycles in runs A and C shows that the magnitude of the  $\text{H}_2\text{O}$  response profile has increased significantly in the later solar cycle. This increased response in run A is due to an increase of  $\text{CO}_2$  and  $\text{CH}_4$ , i.e., an increase in  $\text{CO}_2$  leads to cooling of the background atmosphere, which leads to an intensification of the microphysical processes at ice formation altitudes and thus more effect on the magnitude of positive response. In addition, the increase in  $\text{CH}_4$  leads to more water vapour in the upper mesosphere, resulting in a higher background  $\text{H}_2\text{O}$  concentration, which, in turn, leads to a larger effect of photolysis on  $\text{H}_2\text{O}$  at NLC sublimation altitudes. In run C (Figure 4b), the magnitude of the negative response significantly increased during the late solar cycle, mainly due to  $\text{H}_2\text{O}$  enhancement by  $\text{CH}_4$ . Further details on the mechanism of the water vapour response to the solar cycle and the effects of increasing greenhouse gases are better described in [17].

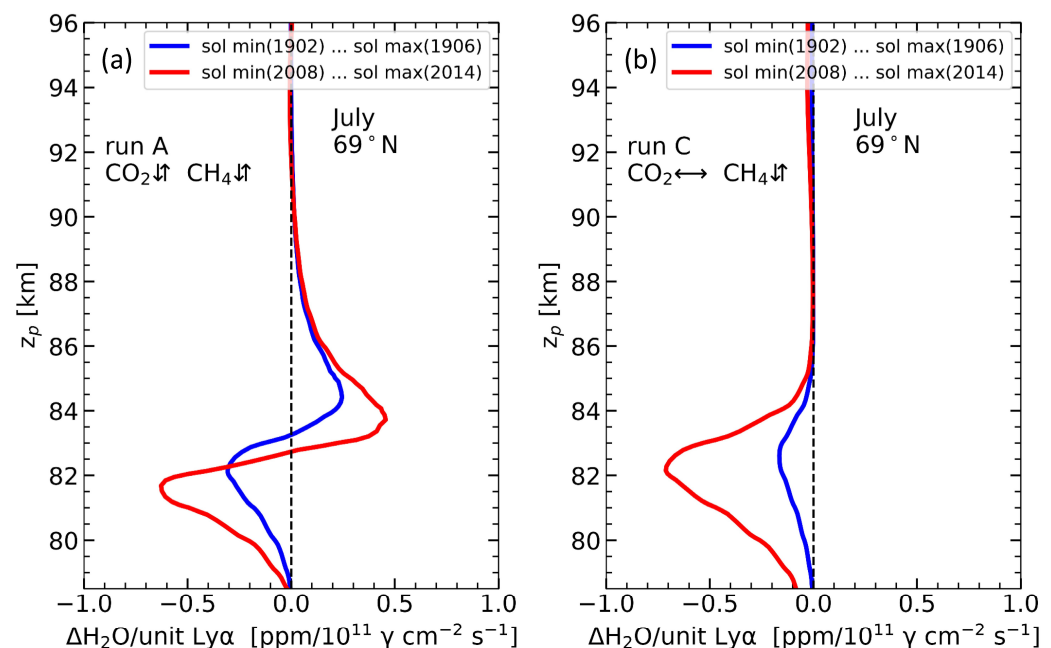


**Figure 4.**  $\text{H}_2\text{O}$  response per unit  $\text{Ly}\alpha$  variations as a function of pressure altitude. (a) MIMAS run A with increasing  $\text{CO}_2$  and  $\text{CH}_4$ ; (b) MIMAS run C with increasing  $\text{CH}_4$  and constant  $\text{CO}_2$ .

### 3.3. Trends in Vertical Profiles of NLC Properties

In this section, we investigate the long-term trends in NLC properties as a function of geometric altitude under different atmospheric greenhouse gas conditions (runs A, B and C). Figure 5 shows the time series of vertical profiles for the number, radius and brightness of ice particles. All these profiles are zonally and monthly averaged at latitudes  $69 \pm 3^\circ$  N.

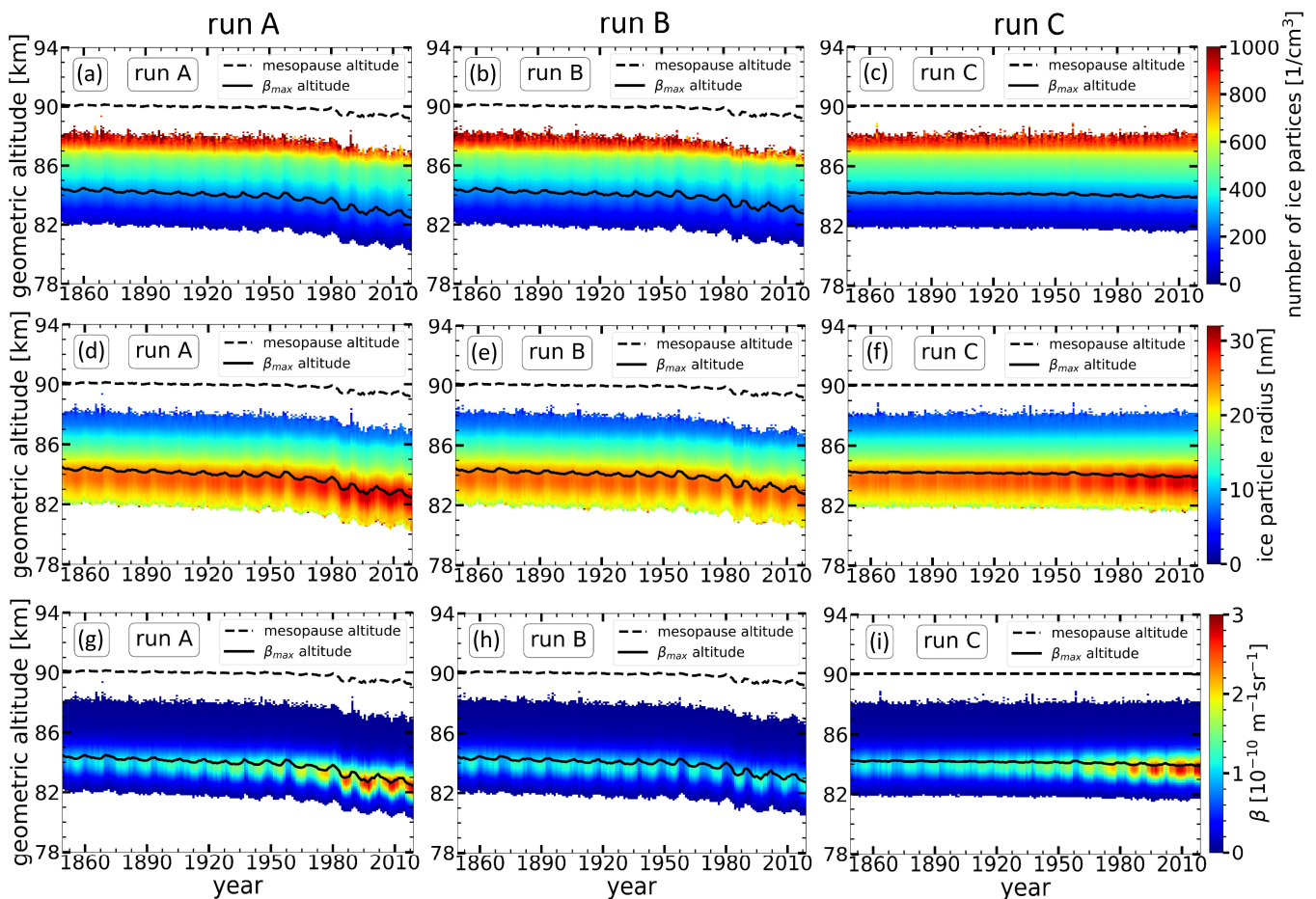


**Figure 5.** Time series of NLC properties (number of ice particles, ice particle radius and brightness) as a function of geometric altitude, averaged monthly (July) and zonally at  $69^\circ$  N. The results are shown for three runs (see insert). (a–c) Number of ice particles, (d–f) ice particle radius and (g–i) NLC brightness. Only NLC above a brightness threshold ( $\beta_{lim} = 0.05$ ) is considered while averaging.

The number of ice particles or the density of ice particles represents the total number of ice particles in a cubic centimetre ( $\text{cm}^{-3}$ ). The trends in the vertical profiles of the number of ice particles show that a significant proportion of the ice particles is located approximately from  $\sim 86$  km to  $\sim 89$  km, and this number density decreases with decreasing altitude. The temperature is lowest at higher altitudes around the mesopause height. Regarding water vapour, its concentration decreases with height and is notably low around mesopause altitudes (see Figure 4). The extremely cold temperature at these altitudes causes these regions to become supersaturated, even though the water vapour concentration is very low. Consequently, the ice particles formed at higher altitudes are smaller in size. These ice particles grow by absorbing more  $\text{H}_2\text{O}$  from the background during sedimentation and reach their maximum size before their sublimation, which occurs between 82 and 85 km altitude. Regardless of the altitude where the maximum number of ice particles is found, the maximum NLC brightness ( $\beta_{max}$ ) (Figure 5d–f) occurs at the altitude corresponding to the maximum particle radius (Figure 5g–i). This is because the increase in the backscatter cross-section is roughly proportional to the radius raised to the power of six ( $r^6$ ). As a result, higher brightness is linked to larger particle radii, resulting in enhanced light scattering at the altitude where the ice particles reach their maximum radius.

The radius of the NLC ice particles shows an increasing trend in runs A (Figure 5d) and C (Figure 5f), while it does not increase significantly in run B (Figure 5e). This is attributed to the increase in  $\text{H}_2\text{O}$  concentration in runs A and C due to the increase in  $\text{CH}_4$ . The increasing availability of water vapour in the background promotes the growth of

ice particles and leads to larger ice particle sizes. The ice particle size in run B does not increase significantly because the H<sub>2</sub>O concentration does not increase due to the constant CH<sub>4</sub> concentration. The temporal evolution of the NLC brightness also shows an apparent increase with time for runs A (Figure 5g) and C (Figure 5i). In contrast, it does not increase in run B (Figure 5h). This indicates that the brightness of NLC also increases due to an increase in H<sub>2</sub>O concentration. It is also noted that the long-term changes in NLC properties are more pronounced at the altitude of the maximum particle radius, especially around the maximum brightness altitude ( $\beta_{\max}$  altitude) indicated by the solid black line.

In Figure 5, we can see the impact of the 11-year solar cycle on the vertical distribution of the NLC properties. During solar minimum, the NLC radius and brightness are larger, while during solar maximum, they are smaller. Less water vapour is available during solar maximum due to increased photolysis and less ice formation growth due to higher temperatures. As a result, smaller ice particles are formed, resulting in less brightness during solar maximum compared to solar minimum years. This effect is visible at all altitudes, with the most significant impact being at the maximum  $\beta_{\max}$  altitude. In runs A and B, the solar cycle influences the lower and upper altitude limits of the NLC layers and the  $\beta_{\max}$  altitude. These parameters respond to the solar cycle by shifting up during the maximum and down during the minimum. In run C, conversely, where there is no temperature change and constant CO<sub>2</sub>, the lower and upper altitude limits of the NLC layers and the  $\beta_{\max}$  altitude show no significant response to the solar cycle. The mechanism behind this is discussed in more detail in the next section.

### 3.4. Greenhouse Gas Effects on NLC Solar Cycle Response

This section analyses the trends in the response of different NLC properties to the 11-year solar cycle. We used MIMAS runs A, B and C to see how the increase in CO<sub>2</sub> and CH<sub>4</sub> affects the solar cycle response of various NLC properties. We only considered the middle of the summer season, i.e., July. We also applied a threshold in NLC brightness ( $\beta_{\text{lim}} = 0.05$ ) to exclude non-NLC events while considering even small NLC events [26]. Figure 6a shows the time series of NLC altitude, herein defined as the  $\beta_{\max}$  altitude. The lower panel of Figure 6a shows the time series of Ly $\alpha$ . The NLC altitude decreases in runs A and B due to CO<sub>2</sub>-induced atmospheric shrinking. In run C, where only H<sub>2</sub>O increases, the NLC altitude remains nearly constant [9,20]. The decrease in NLC altitudes in MIMAS is consistent with long-term radio wave reflectivity altitude observations dating back to 1959 (see Figure 2a in [23]). Figure 6a shows that run A and B show a significant modulation in NLC altitude according to the solar cycle, while run C shows very small modulation. In particular, the NLC altitude positively responds to the solar cycle by an upward shift during solar maximum and a downward shift during solar minimum. This is because the Earth's upper atmosphere heats up during solar maximum due to the Sun's higher energy flux, which causes the background temperature to rise and the mesosphere to expand. The rise in temperature shifts the lower altitude limit of the supersaturated region (where  $S = 1$ ) upwards, which in turn causes an upward shift of the NLC layers. The slight positive response of the NLC altitude in run C is primarily due to the solar cycle-induced photolysis effect on water vapour. The increase in H<sub>2</sub>O photolysis during solar maximum reduces the background H<sub>2</sub>O. As the H<sub>2</sub>O concentration decreases, the saturation ratio ( $S$ ) decreases, which causes a slight upward shift of the lower altitude limit of the supersaturated region (where  $S = 1$ ). Compared to the photolysis effect on H<sub>2</sub>O, the temperature changes have a larger impact on the saturation ratio ([21]) and, thus, on the altitude range of the supersaturated region. For this reason, the NLC altitude response in run C (constant temperature) is very small compared to runs A and B.

To investigate trends in the variation of NLC altitude to the solar cycle, we calculated the response of the NLC altitude to a unit change in Ly $\alpha$  for each solar cycle. To do this, we calculated the absolute difference in NLC altitude between the solar maximum and minimum and divided it by the absolute Ly $\alpha$  difference between the corresponding solar maximum and minimum. Figure 6b presents the time series of the response of NLC altitude

for 15 solar cycles from 1855 to 2019. Before the 19th solar cycle (1954–1964), the response of NLC altitude showed a relatively slow and gradual increase. However, after the 19th solar cycle, there is an acceleration in the response of NLC altitude. After 1960, several properties of NLC, including brightness, radius and IWC, experienced an amplification due to the accelerated increase in greenhouse gas concentrations [9,20]. Therefore, we show linear fit lines for the responses before and after the 19th solar cycle.

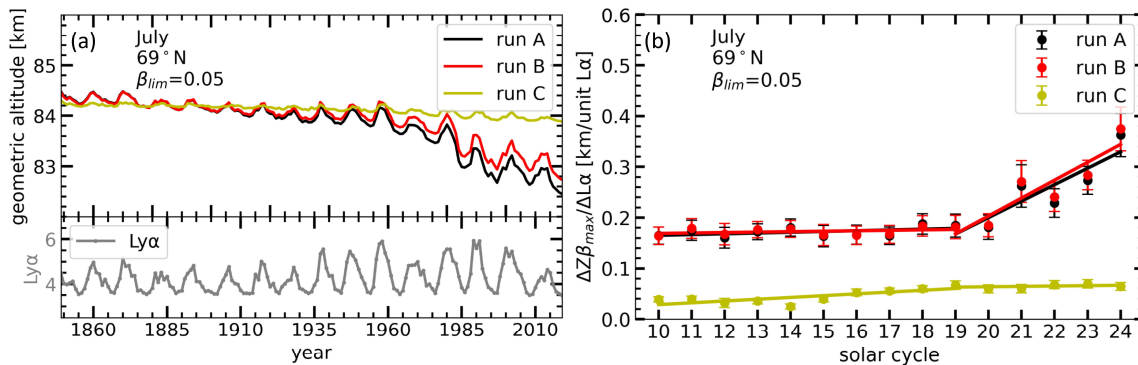


**Figure 6.** (a) Time series of NLC altitudes (averaged for July and zonally at  $69^\circ$  N) from 1849 to 2019. The results from three runs (A, B and C) are shown in the figure (see insert). The lower panel shows the time series of the solar Ly $\alpha$  flux (unit:  $10^{11} \gamma\text{cm}^{-2}\text{s}^{-2}$ ) averaged for July. (b) Response of NLC altitude to the unit change in solar Ly $\alpha$  during solar cycles between 1855 and 2019 (for example, solar cycle 10 corresponds to 1855–1867, while solar cycle 24 represents 2008–2019). The three runs, A, B and C, are shown (see insert) along with linear regression fits. The error bars represent the standard error of the mean for the respective solar cycle years.

We also calculated the solar cycle response of maximum NLC brightness, IWC and NLC occurrence (Figure 7). Figure 7a shows the time series of the solar cycle response of maximum brightness for runs A, B and C. The maximum brightness shows a negative response to the solar cycle variations, and its magnitude increases with time in all runs. However, the magnitude of this increase is more pronounced in runs A and C than in run B. This indicates that an increase in  $\text{H}_2\text{O}$  content is the main factor for the increase in the solar cycle response of NLC brightness. Compared to run C, the higher response in run A can be attributed to the combined effects of  $\text{CO}_2$  increase, temperature changes and  $\text{H}_2\text{O}$  increase. In run A, the negative response of maximum brightness increases from about  $-0.25$  ( $10^{-10} \text{m}^{-1}\text{sr}^{-1}/\text{unit Ly}\alpha$ ) in the 10th solar cycle to  $-0.75$  ( $10^{-10} \text{m}^{-1}\text{sr}^{-1}/\text{unit Ly}\alpha$ ) in the 24th solar cycle.

Figure 7b shows an increasing trend in the magnitude of the response of IWC to the solar cycle in all runs. During the 10th solar cycle, runs A and B have almost identical magnitude of responses to the solar cycle, which are higher than those of run C. In the 22nd solar cycle, the response of IWC to the solar cycle in run C exceeds that of run B. The results suggest that both temperature variations and increasing  $\text{H}_2\text{O}$  contribute to the increase in the response of IWC to the solar cycle. However, the influence of  $\text{H}_2\text{O}$  has a more significant impact on the increased response of IWC than the effects of  $\text{CO}_2$  and temperature. The SBUV satellite has provided the longest dataset of satellite observations for NLC from 1979 to the present, covering latitudes from about  $55^\circ$  N to  $82^\circ$  N in both the Northern and Southern Hemispheres [13]. Our recent study [17] compared the IWC response of MIMAS and SBUV. We found a good agreement in both the anti-correlation pattern and the magnitude of the solar cycle-induced modulation. Moreover, the SOFIE/AIM instrument measured a mean value of IWC  $\sim 59 \text{g}/\text{km}^2$  at mid-latitudes in July 2015, using a threshold value of IWC  $> 40 \text{g}/\text{km}^2$  (see Figure 3 in [35]). This perfectly agrees with the IWC values from MIMAS, namely IWC  $\sim 58\text{--}59 \text{g}/\text{km}^2$  (Figure 3c in [9]), using the same threshold value. This agreement shows the potential of our model to study the response of IWC to the solar cycle [17].

Figure 7c presents the trends in the solar cycle response of the NLC occurrence rate. The occurrence rate of NLC is calculated as follows: For July in each year, the total number of latitude/longitude fields (referred to as “events”,  $N_{max}$ ) is determined by latitude fields (6), longitude fields (120) and time windows of 6 h each ( $31 \text{ days} \times 4 \text{ per day} = 124$ -time steps), resulting in a total number of 89,280 events ( $N_{max}$ ). Whenever an ice layer occurs (applying a given threshold in NLC brightness ( $\beta_{lim} = 0.05$ )) in a given latitude/longitude bin and time segment in MIMAS, we call this an “NLC event”. The NLC occurrence rate is calculated by dividing the number of NLC events by the total number of events ( $N_{max}$ ). The occurrence rate of NLC shows a negative response to the solar cycle. Figure 7c shows that the response of NLC occurrence to the solar cycle is more significant when temperature changes (runs A and B) compared to constant temperature (run C). This suggests that solar cycle temperature variations significantly influence the NLC occurrence rate. This is a consequence of the transition of NLC events to non-NLC events (from super- to sub-saturation), which primarily depends on temperature variation, whereas water vapour is of secondary importance [21]. The response is higher in run B than in run A. In run A, the increase in water vapour leads to an increase in the saturation ratio of events. In run B, where the background H<sub>2</sub>O remains constant, a considerable fraction of events have a low saturation ratio close to one. Therefore, in run B, even a small increase or decrease in temperature during solar maximum or minimum significantly impacts the saturation ratio ( $S$ ), affecting the transition of many NLC events from super- to sub-saturation and, consequently, NLC occurrence.

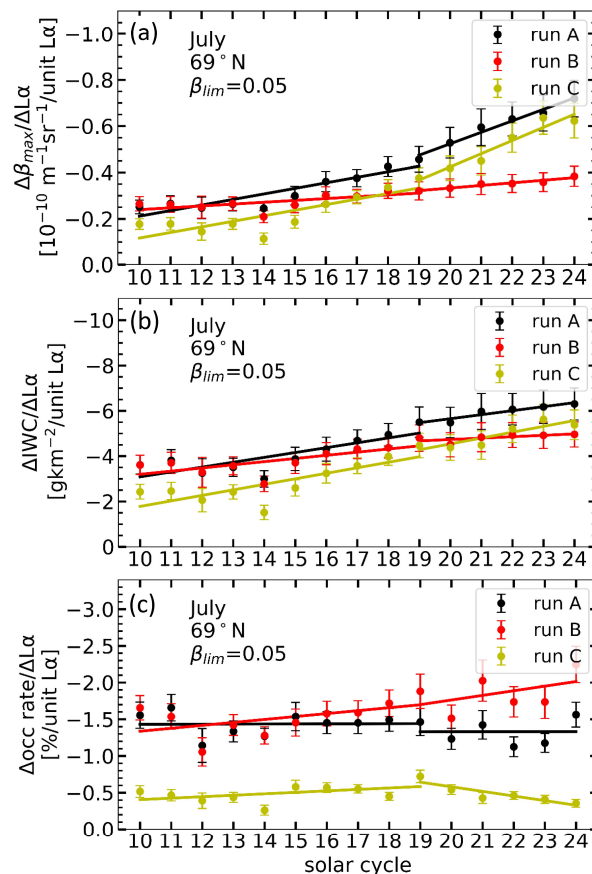


**Figure 7.** NLC properties response to a unit change in solar Lyα at 69° N during solar cycles between 1855 and 2019. Results are shown for three runs, A, B and C (see insert). Error bars indicate the standard error of the mean during respective solar cycle years. The figures are shown for (a) maximum brightness, (b) IWC and (c) NLC occurrence rate, with a threshold value of  $\beta_{lim} = 0.05$  applied.

We find that the response of the NLC occurrence rate after the 19th solar cycle in runs A and C remains roughly constant or decreases slightly. This is because, after the 19th solar cycle, the accelerated increase in carbon dioxide (CO<sub>2</sub>) contributes to the cooling of the upper mesosphere, and the increase in methane (CH<sub>4</sub>) leads to higher concentrations of water vapour. Consequently, more “events” become “NLC events”, and the saturation ratio (S) of these NLC events becomes large. In such cases, the variations in background H<sub>2</sub>O and temperature caused by the solar cycle have little effect on the transition of NLC events from super- to sub-saturation, as the saturation ratio is already very large ( $S \gg 1$ ). For this reason, the response of the occurrence rate of NLC decreases slightly from the 19th solar cycle onwards. It is important to note that the results may vary with a different  $\beta_{lim}$ . For example, the IWC and NLC occurrence rate trends can differ significantly depending on the  $\beta_{lim}$  applied (see Figures 9 and 10 of [20]).

### 3.5. Solar Cycle Response of NLC at Different Latitudes

In this section, we investigate how the response of NLC to the solar cycle varies with latitude. For this study, we used MIMAS run A only and calculated the response of NLC properties at latitudes  $58 \pm 3^\circ$  N (middle),  $69 \pm 3^\circ$  N (high) and  $78 \pm 3^\circ$  N (arctic). Figure 8 shows the time series of the solar cycle response of different NLC properties at middle, high and arctic latitudes. The trends in solar cycle response of NLC altitude, maximum brightness and IWC are larger and similar at high and arctic latitudes compared to those at mid-latitudes. The study on NLC trends by [20] also shows that most NLC parameters behave similarly at high and arctic latitudes.

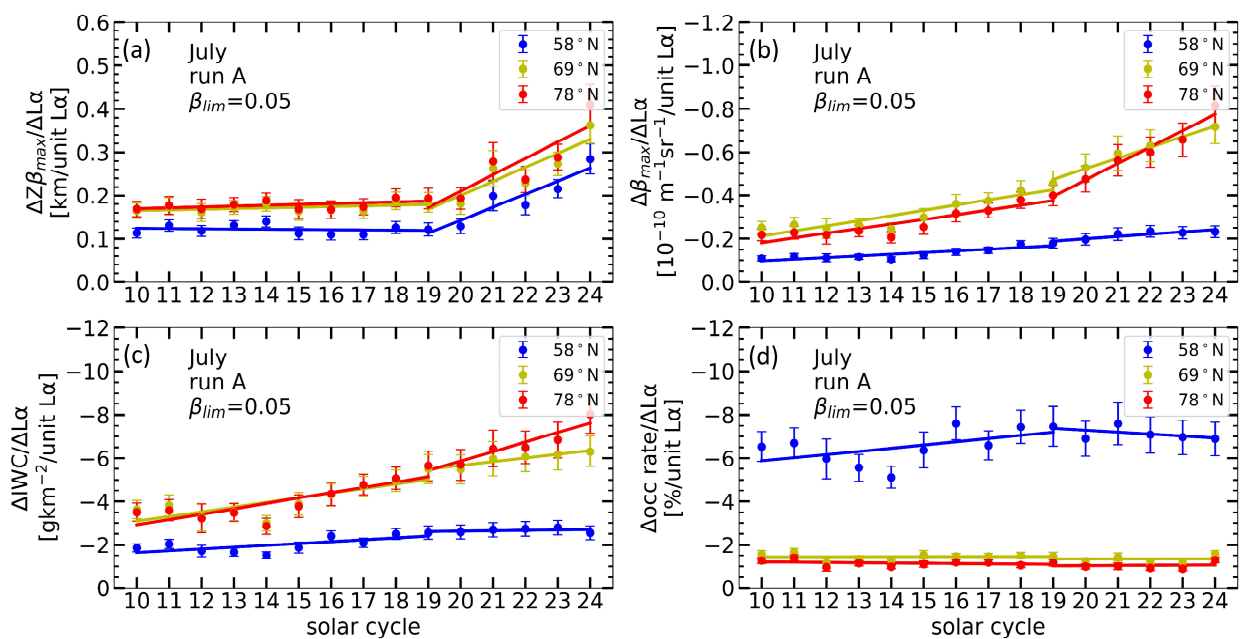


**Figure 8.** NLC properties response to a unit change in solar Ly $\alpha$  during solar cycles between 1855 and 2019. Results are shown for three latitudes (see insert). Error bars indicate the standard error of the mean during respective solar cycle years. The figures are shown for (a) NLC altitude, (b) maximum brightness, (c) IWC and (d) NLC occurrence rate, with a threshold value of  $\beta_{lim} = 0.05$  applied.

In Figure 8a, the NLC altitude positively responds to the solar cycle. As already explained, the primary factor influencing the response of NLC altitude is the temperature change caused by the solar cycle. The temperature response to the solar cycle varies with latitude. During periods of high solar activity, the mesospheric temperature generally increases. This response is usually weaker at mid-latitudes than at higher latitudes, as solar radiation penetrates the mesosphere more directly at higher latitudes, leading to greater warming. In contrast, solar radiation at mid-latitudes has a relatively weaker

influence on the mesosphere temperature. The lower response of NLC altitudes to the solar cycle at mid-latitudes can be attributed to the lower temperature response at mid-latitudes compared to high and arctic latitudes. In Figure 8a, the increase in response (the slope of the regression lines) at mid-latitudes is almost similar to that at high and arctic latitudes. The similarity of the trends in NLC altitude response at all latitudes results from the fact that the temperature trends at NLC altitudes are almost independent of latitude (see Figure 2 in [12] and Figure 7a in [20]).

For maximum brightness and IWC (Figure 8b,c), the response is significantly higher at high and arctic latitudes than at mid-latitudes. As we have already discussed, H<sub>2</sub>O is the main factor influencing the changes in NLC brightness and IWC. At high and arctic latitudes, the extremely low temperatures in the mesopause region in summer and the relatively high water vapour concentrations lead to a larger saturation ratio [37]. Due to these favourable background conditions, more NLC are formed, and NLC brightness and IWC show a significant response to the solar cycle at high and arctic latitudes.

The response of NLC occurrence to the solar cycle is very large at mid-latitudes compared to high and arctic latitudes (Figure 8d). Due to the lower temperatures and relatively high water vapour concentration, the saturation ratio and occurrence rate of NLC are greater at high and arctic latitudes (>80%) than at mid-latitudes (30–60%) (see Figure 10a in [20]). Due to this high saturation ratio of NLC events, the temperature and water vapour changes during the solar cycle need to be more significant to transition from super- to sub-saturation of many NLC events. In mid-latitudes, on the other hand, where NLC occur less frequently due to warmer temperatures (close to frost point temperature) and less water vapour, temperature changes play a critical role in the degree of water vapour saturation. Thus, even slight variations in temperature and water vapour caused by the solar cycle can significantly impact the occurrence of NLC in mid-latitudes. This is why the response of NLC occurrence to the solar cycle is more significant at the mid-latitudes. However, after 1960, this response of occurrence rate at mid-latitudes started to decrease due to accelerated cooling by CO<sub>2</sub> and increasing H<sub>2</sub>O, which increases the saturation ratio of events. Therefore, the effect of the solar cycle started to decrease in the NLC occurrence rate at mid-latitudes after the year 1960. In the future, due to further increases in greenhouse gases, NLC occurrence will increase further, and we expect to see a diminishing solar cycle response of NLC occurrence at all latitudes.

#### 4. Conclusions

Anthropogenic emissions of CO<sub>2</sub> and CH<sub>4</sub> have been increasing over time, with the rate of increase accelerating since 1960. These effects are largely associated with climate change due to their global warming potential. However, in the upper atmosphere, the effects are different. An increase in greenhouse gases leads to a cooling of the upper mesosphere because of an increased escape of infrared photons into space (Luebken et al., 2018). Nevertheless, the implications of this for the upper mesosphere are poorly understood due to difficulties and limitations in measuring atmospheric properties. NLC have been proposed as a key tracer in the summer mesopause region due to their high sensitivity to background atmospheric conditions, including temperature, water vapour concentration and dynamics. Therefore, NLC have been used as the primary indicator of changes in the upper mesosphere and have been the subject of several studies [9,20,38–44]. In this study, the long-term trends in the response of NLC properties and the background atmosphere to the solar cycle are investigated during the period 1849–2019 (see also Supplementary Materials), which covers 15 complete solar cycles (solar cycle 10 to solar cycle 24). We summarise our results by answering the questions raised in the introduction as follows:

- (1) Background temperature and H<sub>2</sub>O show an apparent response to the solar cycle throughout the study period, which intensified after 1960 due to increased greenhouse gas emissions. The temperature response at a given geometric altitude increases due to atmospheric shrinking caused by increased CO<sub>2</sub>. The increase in the response of

- water vapour to the solar cycle is mainly due to the increase in  $\text{CH}_4$ , which leads to the production of more  $\text{H}_2\text{O}$  through oxidation.
- (2) We found solar cycle responses in the vertical distribution profiles of ice particle number, mean radius and NLC brightness. The solar cycle influence is present at all altitudes and peaks at the altitude of maximum NLC brightness. The magnitude of the ice particle radius and brightness response increases with time, mainly due to the increase of  $\text{H}_2\text{O}$ , while the downward shift of the profiles is due to atmospheric shrinking.
  - (3) The properties of NLC, such as maximum brightness, mean radius of ice particles, IWC and occurrence rate, respond to the solar cycle, and these responses increase with time mainly due to an increase in water vapour. The response in NLC altitudes occurs mainly due to solar cycle-induced temperature variation. The upward shift in NLC altitudes is due to the expansion of the atmosphere due to increased heating during solar maximum.
  - (4) The enhancement in response of NLC brightness and ice water content (IWC) to the solar cycle is primarily due to an increase in  $\text{CH}_4$ , which leads to an increase in  $\text{H}_2\text{O}$ . On the other hand, the increase in response of NLC altitude is due to an increase in  $\text{CO}_2$ , which leads to a larger response of the background temperature to the solar cycle.
  - (5) The solar cycle response of NLC properties differs at different latitudes. NLC height, maximum brightness and ice water content are more responsive at high and arctic latitudes and show a similar trend. However, NLC occurrence is less responsive at high and arctic latitudes but much more responsive at mid-latitudes. The saturation ratio of NLC events is higher at high and arctic latitudes, while they are relatively low at mid-latitudes due to higher temperatures and lower water vapour concentrations. Consequently, temperature and water vapour variations during the solar cycle have a greater influence on the occurrence of NLC at mid-latitudes than at high and arctic latitudes.

We found that the increase in greenhouse gas concentrations is primarily responsible for the enhanced response of noctilucent clouds to the solar cycle, illustrating the impact of increasing anthropogenic emissions on temperature and water vapour concentration in the upper atmosphere. Given the important role that the solar cycle plays in the Earth's atmosphere, a detailed understanding of its impact on the upper mesosphere is crucial for improving climate modelling. For example, the response of  $\text{H}_2\text{O}$  to the solar cycle under NLC conditions shows a positive value at NLC-forming altitudes and a negative value at NLC-sublimating altitudes. This information could be taken into account in future developments of atmospheric models, especially for the chemical component, as water vapour plays an important role in the chemistry of the upper mesosphere. In addition, NLC are located at transition altitudes from the atmosphere to space, which are critical for satellites. The changes and enhancements in NLC properties could provide observational evidence of changes in the atmosphere at hard-to-measure altitudes. All these results show that climate change is more pronounced in the upper mesosphere, which can be directly observed from Earth through NLC. Consequently, these results point to the need to reduce greenhouse gas emissions by taking action and implementing appropriate strategies.

**Supplementary Materials:** The following supporting information can be downloaded at: <https://www.mdpi.com/article/10.3390/atmos15010088/s1>, Table S1. A table presenting the definitions of technical terms used in the article; Figure S1. Time series of background temperature and  $\text{H}_2\text{O}$  at the maximum brightness altitude for three different latitudes ( $58^\circ$  N,  $69^\circ$  N, and  $78^\circ$  N) spanning the years 1849 to 2010; Figure S2. Time series of NLC properties (see y-axis label) for three different latitudes ( $58^\circ$  N,  $69^\circ$  N, and  $78^\circ$  N) spanning the years 1849 to 2010.

**Author Contributions:** M.G. conducted LIMA model simulations; A.V. conducted MIMAS model simulations and wrote the first draft of the paper; A.V., G.B., M.G. and F.-J.L. interpreted the results and contributed significantly to the interpretation and improvement of the paper. All authors have read and agreed to the published version of the manuscript.

**Funding:** This research was funded by the TIMA project of the BMBF (Bundesministerium für Bildung und Forschung) research initiative ROMIC (grant no. 01LG1902A).

**Institutional Review Board Statement:** Not applicable.

**Informed Consent Statement:** Not applicable.

**Data Availability Statement:** Lyman- $\alpha$  data are available at <http://lasp.colorado.edu/lisird/lya/> (accessed on 10 November 2023) from LASP. The data utilised in this manuscript can be downloaded from <https://www.radar-service.eu/radar/en/dataset/xqHORiMNGebILWkX?token=WOVCIyZPRkGXIBdpgcnU> (accessed on 10 November 2023).

**Acknowledgments:** We would like to thank Corinna Schütt for her support in working with the LIMA model script. We acknowledge the Mauna Loa records for CO<sub>2</sub> and CH<sub>4</sub> from <http://www.esrl.noaa.gov/gmd/ccgg/>, last access: 16 November 2023.

**Conflicts of Interest:** The contact author has declared that none of the authors have any competing interests.

## References

- Garcia, R.R. Dynamics, Radiation, and Photochemistry in the Mesosphere: Implications for the Formation of Noctilucent Clouds. *J. Geophys. Res. Atmos.* **1989**, *94*, 14605–14615. [CrossRef]
- Berger, U.; von Zahn, U. Three-Dimensional Modeling of the Trajectories of Visible Noctilucent Cloud Particles: An Indication of Particle Nucleation Well below the Mesopause. *J. Geophys. Res. Atmospheres* **2007**, *112*, D16204. [CrossRef]
- Gadsden, M.; Schröder, W. *Noctilucent Clouds; Physics and Chemistry in Space Planetology*; Springer: Berlin/Heidelberg, Germany, 1989; ISBN 978-3-540-50685-0.
- Gadsden, M. A Secular Change in Noctilucent Cloud Occurrence. *J. Atmos. Terr. Phys.* **1990**, *52*, 247–251. [CrossRef]
- Thomas, G.E.; Olivero, J. Noctilucent Clouds as Possible Indicators of Global Change in the Mesosphere. *Adv. Space Res.* **2001**, *28*, 937–946. [CrossRef]
- Thomas, G.E. Is the polar mesosphere the miner’s canary of global change? *Adv. Space Res.* **1996**, *18*, 149–158. [CrossRef]
- Thomas, G.E. Are Noctilucent Clouds Harbingers of Global Change in the Middle Atmosphere? *Adv. Space Res.* **2003**, *32*, 1737–1746. [CrossRef]
- Hervig, M.E.; Berger, U.; Siskind, D.E. Decadal Variability in PMCs and Implications for Changing Temperature and Water Vapor in the Upper Mesosphere. *J. Geophys. Res.* **2016**, *121*, 2383–2392. [CrossRef]
- Lübken, F.J.; Berger, U.; Baumgarten, G. On the Anthropogenic Impact on Long-Term Evolution of Noctilucent Clouds. *Geophys. Res. Lett.* **2018**, *45*, 6681–6689. [CrossRef]
- DeLand, M.T.; Shettle, E.P.; Thomas, G.E.; Olivero, J.J. A Quarter-Century of Satellite Polar Mesospheric Cloud Observations. *J. Atmos. Sol.-Terr. Phys.* **2006**, *68*, 9–29. [CrossRef]
- Von Zahn, U.; Berger, U. Persistent Ice Cloud in the Midsummer Upper Mesosphere at High Latitudes: Three-Dimensional Modeling and Cloud Interactions with Ambient Water Vapor. *J. Geophys. Res. Atmos.* **2003**, *108*. [CrossRef]
- Lübken, F.J.; Berger, U.; Baumgarten, G. Temperature Trends in the Midlatitude Summer Mesosphere. *J. Geophys. Res. Atmos.* **2013**, *118*, 13347–13360. [CrossRef]
- Hervig, M.E.; Siskind, D.E.; Bailey, S.M.; Merkel, A.W.; DeLand, M.T.; Russell, J.M. The Missing Solar Cycle Response of the Polar Summer Mesosphere. *Geophys. Res. Lett.* **2019**, *46*, 10132–10139. [CrossRef]
- DeLand, M.T.; Shettle, E.P.; Thomas, G.E.; Olivero, J.J. Solar Backscattered Ultraviolet (SBUV) Observations of Polar Mesospheric Clouds (PMCs) over Two Solar Cycles. *J. Geophys. Res. Atmos.* **2003**, *108*, 8445. [CrossRef]
- Hervig, M.; Siskind, D. Decadal and Inter-Hemispheric Variability in Polar Mesospheric Clouds, Water Vapor, and Temperature. *J. Atmos. Sol.-Terr. Phys.* **2006**, *68*, 30–41. [CrossRef]
- Siskind, D.E.; Stevens, M.H.; Hervig, M.E.; Randall, C.E. Recent Observations of High Mass Density Polar Mesospheric Clouds: A Link to Space Traffic? *Geophys. Res. Lett.* **2013**, *40*, 2813–2817. [CrossRef]
- Vellalassery, A.; Baumgarten, G.; Grygalashvily, M.; Lübken, F.-J. Greenhouse Gas Effects on the Solar Cycle Response of Water Vapour and Noctilucent Clouds. *Ann. Geophys.* **2023**, *41*, 289–300. [CrossRef]
- Nedoluha, G.E.; Kiefer, M.; Lossow, S.; Michael Gomez, R.; Kämpfer, N.; Lainer, M.; Forkman, P.; Martin Christensen, O.; Jin Oh, J.; Hartogh, P.; et al. The SPARC Water Vapor Assessment II: Intercomparison of Satellite and Ground-Based Microwave Measurements. *Atmos. Chem. Phys.* **2017**, *17*, 14543–14558. [CrossRef]
- Hervig, M.E.; Siskind, D.E.; Bailey, S.M.; Russell, J.M. The Influence of PMCs on Water Vapor and Drivers behind PMC Variability from SOFIE Observations. *J. Atmos. Sol.-Terr. Phys.* **2015**, *132*, 124–134. [CrossRef]
- Lübken, F.J.; Baumgarten, G.; Berger, U. Long Term Trends of Mesospheric Ice Layers: A Model Study. *J. Atmos. Sol.-Terr. Phys.* **2021**, *214*, 105378. [CrossRef]
- Berger, U.; Von Zahn, U. Icy Particles in the Summer Mesopause Region: Three-Dimensional Modeling of Their Environment and Two-Dimensional Modeling of Their Transport. *J. Geophys. Res. Space Phys.* **2002**, *107*, SIA-10. [CrossRef]

22. Berger, U. Modeling of Middle Atmosphere Dynamics with LIMA. *J. Atmos. Sol.-Terr. Phys.* **2008**, *70*, 1170–1200. [[CrossRef](#)]
23. Berger, U.; Lübken, F.J. Mesospheric Temperature Trends at Mid-Latitudes in Summer. *Geophys. Res. Lett.* **2011**, *38*, L22804. [[CrossRef](#)]
24. Machol, J.; Snow, M.; Woodraska, D.; Woods, T.; Viereck, R.; Coddington, O. An Improved Lyman-Alpha Composite. *Earth Space Sci.* **2019**, *6*, 2263–2272. [[CrossRef](#)]
25. Compo, G.P.; Whitaker, J.S.; Sardeshmukh, P.D.; Matsui, N.; Allan, R.J.; Yin, X.; Gleason, B.E.; Vose, R.S.; Rutledge, G.; Bessemoulin, P.; et al. The Twentieth Century Reanalysis Project. *Q. J. R. Meteorol. Soc.* **2011**, *137*, 1–28. [[CrossRef](#)]
26. WMO. *Statement on the Status of the Global Climate in 2011*; World Meteorological Organization: Geneva, Switzerland, 2012; ISBN 978-92-63-11085-5.
27. Etheridge, D.; Barnola, J.; Morgan, V.; Steele, L.; Langenfelds, R.; Francey, R. *Historical CO<sub>2</sub> Records from the Law Dome DE08, DE08-2, and DSS Ice Cores (1006 A.D.-1978 A.D)*; Oak Ridge National Laboratory, U.S. Department of Energy: Oak Ridge, TN, USA, 1998.
28. Yiğit, E.; Medvedev, A.S. Extending the Parameterization of Gravity Waves into the Thermosphere and Modeling Their Effects. In *Climate and Weather of the Sun-Earth System (CAWSES) Highlights from a Priority Program*; Springer: Dordrecht, The Netherlands, 2013; pp. 467–480.
29. Butchart, N. The Brewer-Dobson Circulation. *Rev. Geophys.* **2014**, *52*, 157–184. [[CrossRef](#)]
30. Kiliani, J. 3-D Modeling of Noctilucent Cloud Evolution and Relationship to the Ambient Atmosphere. Ph.D. Thesis, IAP. University of Rostock, Kühlungsborn, Germany, 2014.
31. Roble, R.G.; Dickinson, R.E. How will changes in carbon dioxide and methane modify the mean structure of the mesosphere and thermosphere? *Geophys. Res. Lett.* **1989**, *46*, 1441–1444. [[CrossRef](#)]
32. Garcia, R.R.; Marsh, D.R.; Kinnison, D.E.; Boville, B.A.; Sassi, F. Simulation of Secular Trends in the Middle Atmosphere, 1950–2003. *J. Geophys. Res. Atmos.* **2007**, *112*, D09301. [[CrossRef](#)]
33. Marsh, D.R.; Mills, M.J.; Kinnison, D.E.; Lamarque, J.F.; Calvo, N.; Polvani, L.M. Climate Change from 1850 to 2005 Simulated in CESM1(WACCM). *J. Clim.* **2013**, *26*, 7372–7391. [[CrossRef](#)]
34. Keckhut, P.; Wild, J.D.; Gelman, M.; Miller, A.J.; Hauchecorne, A. Investigations on Long-term Temperature Changes in the Upper Stratosphere Using Lidar Data and NCEP Analyses. *J. Geophys. Res. Atmos.* **2001**, *106*, 7937–7944. [[CrossRef](#)]
35. Hervig, M.E.; Gerding, M.; Stevens, M.H.; Stockwell, R.; Bailey, S.M.; Russell, J.M.; Stober, G. Mid-Latitude Mesospheric Clouds and Their Environment from SOFIE Observations. *J. Atmos. Sol.-Terr. Phys.* **2016**, *149*, 1–14. [[CrossRef](#)]
36. Remsberg, E. Observation and Attribution of Temperature Trends Near the Stratopause From HALOE. *J. Geophys. Res. Atmos.* **2019**, *124*, 6600–6611. [[CrossRef](#)] [[PubMed](#)]
37. Körner, U.; Sonnemann, G.R. Global Three-dimensional Modeling of the Water Vapor Concentration of the Mesosphere-mesopause Region and Implications with Respect to the Noctilucent Cloud Region. *J. Geophys. Res. Atmos.* **2001**, *106*, 9639–9651. [[CrossRef](#)]
38. Hansen, G.; Von Zahn, U. Simultaneous Observations of Noctilucent Clouds and Mesopause Temperatures by Lidar. *J. Geophys. Res. Atmos.* **1994**, *99*, 18989–18999. [[CrossRef](#)]
39. Nussbaumer, V.; Fricke, K.H.; Langer, M.; Singer, W.; Von Zahn, U. First Simultaneous and Common Volume Observations of Noctilucent Clouds and Polar Mesosphere Summer Echoes by Lidar and Radar. *J. Geophys. Res. Atmos.* **1996**, *101*, 19161–19167. [[CrossRef](#)]
40. Von Cossart, G.; Hoffmann, P.; Von Zahn, U.; Keckhut, P.; Hauchecorne, A. Mid-latitude Noctilucent Cloud Observations by Lidar. *Geophys. Res. Lett.* **1996**, *23*, 2919–2922. [[CrossRef](#)]
41. Von Zahn, U.; Von Cossart, G.; Fiedler, J.; Rees, D. Tidal Variations of Noctilucent Clouds Measured at 69° N Latitude by Groundbased Lidar. *Geophys. Res. Lett.* **1998**, *25*, 1289–1292. [[CrossRef](#)]
42. Karlsson, B.; Rapp, M. Latitudinal Dependence of Noctilucent Cloud Growth. *Geophys. Res. Lett.* **2006**, *33*, 2006GL025805. [[CrossRef](#)]
43. Hultgren, K.; Körnich, H.; Gumbel, J.; Gerding, M.; Hoffmann, P.; Lossow, S.; Megner, L. What Caused the Exceptional Mid-Latitudinal Noctilucent Cloud Event in July 2009? *J. Atmos. Sol.-Terr. Phys.* **2011**, *73*, 2125–2131. [[CrossRef](#)]
44. Kaifler, N.; Kaifler, B.; Wilms, H.; Rapp, M.; Stober, G.; Jacobi, C. Mesospheric Temperature during the Extreme Midlatitude Noctilucent Cloud Event on 18/19 July 2016. *J. Geophys. Res. Atmos.* **2018**, *123*, 13775–13789. [[CrossRef](#)]

**Disclaimer/Publisher’s Note:** The statements, opinions and data contained in all publications are solely those of the individual author(s) and contributor(s) and not of MDPI and/or the editor(s). MDPI and/or the editor(s) disclaim responsibility for any injury to people or property resulting from any ideas, methods, instructions or products referred to in the content.



## Appendix C

# Lübken et al., 2024

Franz Josef Lübken et al. (2024). "Absorption of Solar Radiation by Noctilucent Clouds in a Changing Climate". In: *Geophysical Research Letters* 51.8. ISSN: 0094-8276. DOI: 10.1029/2023GL107334

# Geophysical Research Letters®



## RESEARCH LETTER

10.1029/2023GL107334

## Absorption of Solar Radiation by Noctilucent Clouds in a Changing Climate

Franz-Josef Lübken<sup>1</sup> , Gerd Baumgarten<sup>1</sup>, Mykhaylo Grygalashvyly<sup>1</sup>, and Ashique Vellalassery<sup>1</sup> 

<sup>1</sup>Leibniz Institute of Atmospheric Physics, Kühlungsborn, Germany

### Key Points:

- Noctilucent clouds (NLC) are ice clouds in the summer mesopause region at middle and polar latitudes
- The expected methane related increase in water vapor at NLC heights will lead to more and larger ice particles
- Larger ice particles will lead to an enhanced absorption of solar radiation

### Correspondence to:

F.-J. Lübken,  
luebken@iap-kborn.de

### Citation:

Lübken, F.-J., Baumgarten, G., Grygalashvyly, M., & Vellalassery, A. (2024). Absorption of solar radiation by noctilucent clouds in a changing climate. *Geophysical Research Letters*, *51*, e2023GL107334. <https://doi.org/10.1029/2023GL107334>

Received 16 NOV 2023

Accepted 29 MAR 2024

### Author Contributions:

**Conceptualization:** Franz-Josef Lübken, Gerd Baumgarten

**Formal analysis:** Franz-Josef Lübken, Ashique Vellalassery

**Funding acquisition:** Franz-Josef Lübken

**Investigation:** Gerd Baumgarten

**Software:** Gerd Baumgarten,

Mykhaylo Grygalashvyly,

Ashique Vellalassery

**Supervision:** Franz-Josef Lübken

**Validation:** Franz-Josef Lübken,

Mykhaylo Grygalashvyly

**Writing – original draft:** Franz-

Josef Lübken

**Writing – review & editing:** Franz-

Josef Lübken, Gerd Baumgarten,

Mykhaylo Grygalashvyly,

Ashique Vellalassery

**Abstract** The expected increase in climate change related methane emissions will result in an increase in middle atmospheric water vapor abundance. This will in turn amplify the brightness of noctilucent clouds (NLC). To examine how NLC will impact the absorption of solar radiation, we utilized both an atmospheric background model and a microphysical model spanning the period from 1950 to 2100. At a latitude of  $69 \pm 3^\circ\text{N}$ , UV absorption at  $\lambda = 126 \text{ nm}$  is projected to rise from  $\sim 3\%$  to  $\sim 7\%$ . In specific regions, the absorption may spike to approximately 30% by the year 2100. In the visible spectrum, we observe an absorption increase from 0.0030% in 1950 to 0.020% by 2100. Local absorption reach up to 0.35% by the year 2100. These trends are similar at  $79 \pm 3^\circ\text{N}$ , but are smaller at  $58 \pm 3^\circ\text{N}$ . Future average absorptions are comparable to solar cycle fluctuations, but local increases are significantly more pronounced. The ice mass contained in NLC is projected to surge from 677 to 1871 tons between 1950 and 2100.

**Plain Language Summary** Noctilucent clouds (NLC) consist of water ice particles and appear in the summer season in the upper mesosphere at high/middle latitudes where temperatures are very low. Methane is photochemically converted to water vapor in the middle atmosphere. Therefore, the future increase of methane concentration will lead to an increase in water vapor, and to an enhancement of NLC occurrence and brightness. We apply an atmospheric background model and a microphysical ice particle model to study the associated absorption of solar radiation. At  $69^\circ\text{N}$  mean absorptions in the UV will increase from  $\sim 3\%$  to  $\sim 7\%$  from 1950 to 2100, respectively. Locally, the absorption can increase to  $\sim 30\%$  in 2100. In the visible ( $\lambda = 532 \text{ nm}$ ) the corresponding numbers are 0.0030% (1950) to 0.020% (2100), that is, an increase by a factor of  $\sim 7$ , and local maxima up to 0.35% in 2100. Mean absorptions are comparable to variations throughout a solar cycle, but may locally be much larger. Effects on the photochemistry are therefore expected. The total amount of ice mass bound in NLC also increases with time, namely from 677 tons in 1950 to 1871 tons in 2100. NLC will be easier to observe by naked eye, that is, they will be more frequent and brighter.

## 1. Introduction

Noctilucent clouds (NLC) consist of water ice particles and appear in the summer season in the upper mesosphere at high and middle latitudes where temperatures are very low (e.g., Gadsden & Schröder, 1989, and references therein). There is a long standing scientific dispute, if or not NLC are indicators of climate change, where an unequivocal proof by observations is still pending (see, for example, Berger & Lübken, 2015; Fiedler et al., 2017; Pertsev et al., 2014; Russell III et al., 2015; Thomas, 2003). Results on the future development of NLC have recently been published by Yu et al. (2023), but a zero-dimensional model was applied for NLC and no extinctions were calculated. It is generally assumed that the optical thickness of these clouds is on the order of  $10^{-4}$  or less, that is, too small to cause a significant extinction of solar radiation (e.g., Kokhanovsky, 2005). It has been shown in previous studies that the main reason for an increase of extinction by NLC is given by an increase of water vapor which is expected to grow in the middle atmosphere due to enhanced emissions of methane (in the troposphere) which is photochemically converted to water vapor in the middle atmosphere. In this paper, we study the extinction of solar radiation by NLC at various wavelengths in a future climate scenario with increasing methane. We use the atmospheric background model LIMA (Leibniz Institute Middle Atmosphere Model) and a microphysical model of ice particle formation called MIMAS (Mesospheric Ice Microphysics And tranSPort model). Various results on the historical NLC development based on LIMA/MIMAS are described in Lübken et al. (2021), hereafter referred to as LBB21, and references therein.

© 2024. The Authors.

This is an open access article under the terms of the [Creative Commons Attribution-NonCommercial-NoDerivs](https://creativecommons.org/licenses/by-nc-nd/4.0/)

License, which permits use and

distribution in any medium, provided the

original work is properly cited, the use is

non-commercial and no modifications or

adaptations are made.

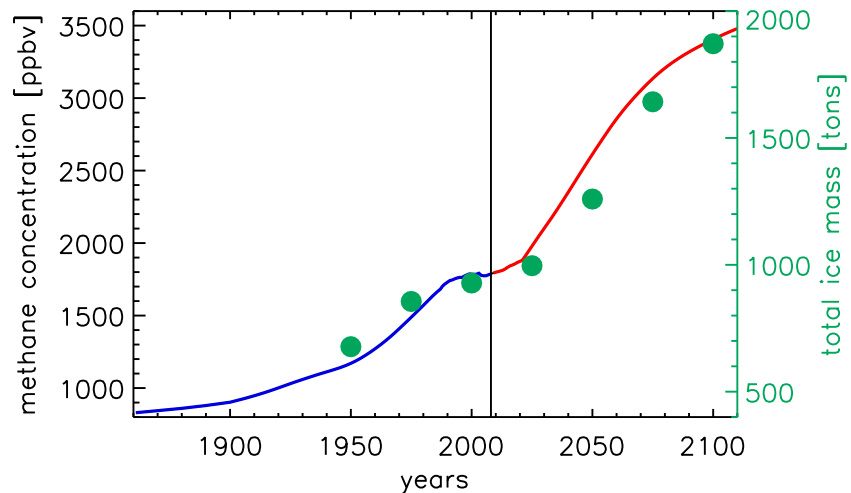


**Figure 1.** Concentration of methane in the troposphere (blue) as used in LIMA/MIMAS, including future projections taken from IPCC (red). Green dots: total ice mass bound in NLC particles (right axis).

## 2. Model

For the background atmosphere we use the global model LIMA which is nudged to the real atmosphere at lower heights. LIMA is a fully non-linear, global, and three-dimensional model extending from the ground to the lower thermosphere (0–150 km), taking into account major processes of radiation, chemistry, and transport (see Berger, 2008; Berger & Lübken, 2011; Berger & von Zahn, 2002, for more details). LIMA has extensively been validated by comparison with observations (see, for example, Hervig et al., 2016; Lübken et al., 2021). Most important, LIMA nicely reproduces the low temperatures being typical for the middle/polar summer mesosphere. For this study we use background conditions from a representative year (1982) for all years, that is, the dynamical forcing of the upper mesosphere/lower thermosphere is kept constant for all years. In MIMAS the formation of ice particles is determined by investigating the fate of a total of 40 million dust/ice particles which results in the full size distribution (i.e., the number of particles within a given size bin) which is then used to calculate extinction coefficients. In some models, only the mean ice particle radius is available, which requires to assume a theoretical size distribution. Since the optical properties vary roughly as  $r^6$  ( $r$  = radius), errors in the assumed distribution can introduce significant errors in extinctions.

In MIMAS the interaction of ice particles with background water vapor is considered, including freeze drying. In this study, we consider an increase of methane only (leading to an increase in water vapor as described in LBB21), that is, keeping temperatures and dynamics constant (note that changing  $H_2O$  causes a very small temperature change which can be neglected in this context). We have shown in previous papers that the increase of optical parameters such as brightness and extinction is nearly entirely given by an increase of  $H_2O$ , whereas a decrease of temperatures (caused by an increase of carbon dioxide) plays a minor role. Note that microphysical effects perhaps play a key role in this behavior (see, for example, Figure 3 in Lübken et al. (2018)). We realize that temperature changes are considered to be more important for NLC in other models, which, however, do not include microphysical processes (see, e.g., Hervig et al., 2015). In previous studies we have presented various comparisons of results from LIMA and MIMAS with ground based and satellite borne observations and found excellent agreement (see, e.g., Lübken et al., 2021; Vellalassery et al., 2023; Schmidt et al., 2018, and references therein). In Figure 1 we show the temporal behavior of methane concentration in the troposphere used in MIMAS. The expected future development is based on IPCC AR4. More specifically, we use the RCP 8.5 scenario as described in Riahi et al. (2011) because here the methane concentration is increasing with time, which is not the case for some other scenarios.

For computational reasons we use LIMA/MIMAS model results from selected years in the period 1950 to 2100. Furthermore, we consider the core of the NLC season only, namely the month of July. As in LBB21, we study three latitude bands, namely  $58 \pm 3^\circ N$ ,  $69 \pm 3^\circ N$ , and  $78 \pm 3^\circ N$ , respectively. In total there are 89,280 columns per year in each latitude band, since there are 6 latitudes, 120 longitudes, 31 days, and 4 time-steps per day. Note

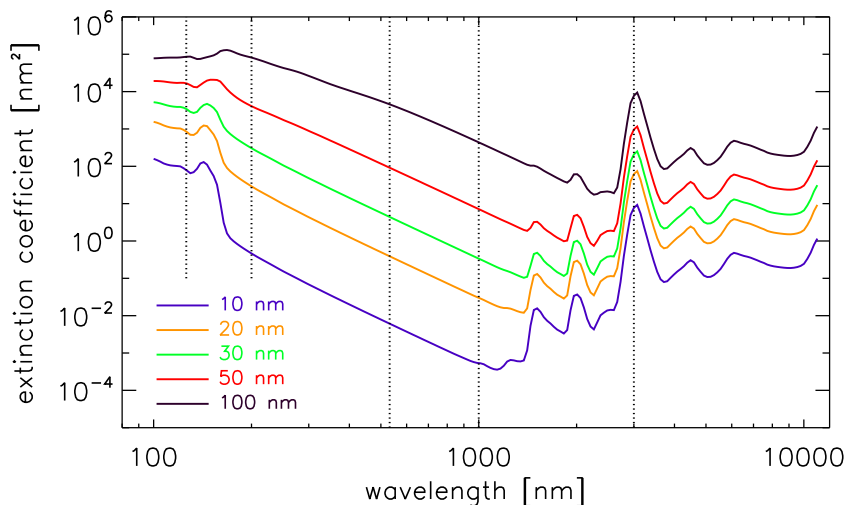


**Figure 2.** Extinction coefficients as a function of wavelength for (mono-dispers) particle radii as given in the insert (in nm, various colors). The vertical lines mark wavelengths where we have calculated extinctions by the NLC layer.

that the ice layer and related optical parameters may vary substantially from column to column. We have considered the large solar zenith angles at high latitudes in summer (we have used  $\chi = 80^\circ$  as a representative value) by increasing the optical depths and related parameters by a factor of 5.76, that is,  $1/\cos \chi$  approximating the Chapman function. Schmidt et al. (2018) have performed a systematic comparison of observations by lidar and from satellites with LIMA/MIMAS. They showed that radii in the model were slightly but systematically too small. We have adopted their results and increased all radii in LIMA/MIMAS by a factor of 1.35 and consequently the optical parameters by a factor of 1.35<sup>6</sup>.

The extinction coefficient (“cross section”)  $\sigma(r, \lambda)$  (units:  $\text{m}^2$ ) is a function of particle radius  $r$  and wavelength  $\lambda$ . It is needed to calculate the optical depth  $d\tau$  for a given wavelength  $\lambda$  traversing a layer at height  $z$  with a geometrical thickness  $dz$ :

$$d\tau(z, r, \lambda) = \sigma(r, \lambda) \cdot dz \cdot dN(z, r, dr) \quad [/\] \quad (1)$$

where  $dN(z, r, dr)$  is the number density of particles at height  $z$  with radius between  $r$  and  $r + dr$ . The total optical depth  $\tau(\lambda)$  is determined by integrating over all radii. The amount of solar light with wavelength  $\lambda$  passing the layer (relative to the incoming intensity) is  $\exp(-\tau)$ , and the relative attenuation is  $a = 100 \cdot (1 - e^{-\tau})$  (in %). For a ground-based lidar the backscatter coefficient  $\beta$  determines the amount of laser light being backscattered. In MIMAS, backscatter coefficients and optical depths are determined for every box, that is, at all altitude layers, at all latitudes/longitudes, and at all time-steps. The effect of several boxes is given by summation over all  $\tau$ .

In Figure 2 we show extinction coefficients as a function of wavelengths for mono-dispers particles with given radii. In a significant part of the spectrum in the visible and infrared (i.e., between roughly 200–1000 nm) the extinction coefficient varies as  $\lambda^{-4}$  for a given radius, and approximately as  $r^6$  for a given wavelength. This implies that (a) the size of the NLC particles is crucial for the total extinction, and (b) the absorption of solar radiation generally decreases rapidly with increasing wavelength. This is no longer true for wavelengths larger than  $\sim 1000$ – $2000$  nm, and for radii smaller than  $\sim 200$  nm. Mie calculations were performed assuming mono-dispers spherical ice particles applying the wavelength dependent refractive index values from Warren and Brandt (2008). We apply the approximation of spherical particle shape, that is, ignoring potential non-sphericity, mainly to avoid further complications and to facilitate comparison with other global scale models. The resonances with a major peak at  $\sim 3000$  nm are due to vibrational excitation of OH.

### 3. Results

In Figure 3 the relative occurrence frequencies of maximum backscatter coefficients ( $\beta_{\max}$ ) from LIMA/MIMAS are presented for a given year (2000) considering all columns in the latitude band  $69 \pm 3^\circ\text{N}$ . Observational results

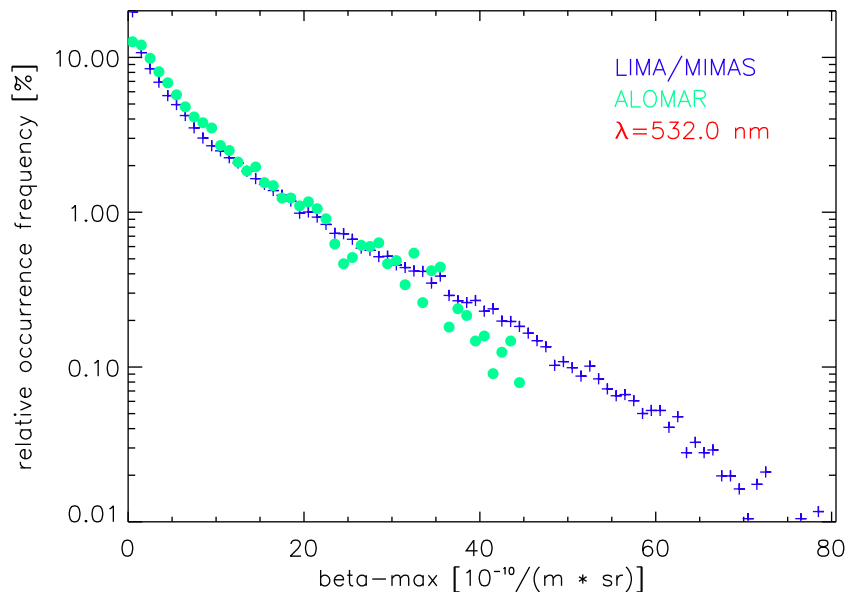


**Figure 3.** Relative frequency of occurrence (in %) of (i) maximum backscatter values ( $\beta_{\max}$ , blue crosses) from LIMA/MIMAS in all columns in a given year (2000) in July in the latitude band  $69 \pm 3^\circ\text{N}$ , and (ii)  $\beta_{\max}$ -values from the ALOMAR RMR lidar at  $69^\circ\text{N}$  during 1–31 July from the years 1997–2020 (green dots). Both data sets are for a wavelength of 532 nm.

of  $\beta_{\max}$  from the ALOMAR Rayleigh-Mie-Raman (RMR) lidar at  $69^\circ\text{N}$  for the years 1997–2020 are shown for comparison (both for the month of July only). A description of the NLC data set obtained from this lidar is presented in Fiedler et al. (2017). Note, that lidar data were averaged over 15 min which eliminates very bright NLC. The idea is to characterize the variability of NLC brightness (expressed as  $\beta_{\max}$ ) from spatial (LIMA/MIMAS) and temporal (ALOMAR) coverage. Note that there are “only” a few thousand NLC events in 24 years measured by the lidar, partly because of constraints due to bad weather and/or other operational limitations. This implies that an occurrence frequency of 0.01% (the lower end of the LIMA/MIMAS distribution in Figure 3) corresponds to less than 1 event(!) in 24 years for the lidar.

As can be seen from Figure 3 the relative distribution of  $\beta_{\max}$ -values from observations and from the model are very similar which supports the idea that particle size and number density distributions in LIMA/MIMAS are rather realistic, which is then also true for extinction coefficients and attenuations.

In Figure 4 we present a frequency distribution of attenuations from various years at  $69 \pm 3^\circ\text{N}$  for a wavelength of  $\lambda = 200$  nm where we have considered boxes only where radii are larger than 2 nm to avoid mixture with dust particles. We have chosen 200 nm since this allows a fairly easy extrapolation to larger wavelengths and the extinction is similar to the maximum around 3000 nm (see Figure 2). From Figure 4 we can identify how often (i.e., in how many columns) a given attenuation appears in a given year, relative to the total number of columns (=89,280). For example, in 2080 and  $\lambda = 200$  nm an attenuation of 2% appears in ~6% of all columns. Or, the chance to have attenuations of 3% (at  $\lambda = 200$  nm) increases by a factor of roughly 300 from 2000 to 2040. As expected, the distributions shown in Figure 4 drop off less rapidly for future years, that is, larger attenuations appear more frequently. Note that nearly all columns are filled with ice particles which is consistent with the observation that PMSE (polar mesosphere summer echoes) are present at polar and arctic latitudes in summer nearly all the time (Latteck et al., 2021). Note that PMSE are much less sensitive to ice particle radii compared to NLC. If we limit the occurrence frequency to larger than 1%, the maximum attenuations are roughly 2%, 2.7%, and 4.2% in 2000, 2040, and 2080, respectively. In the visible ( $\lambda = 500$  nm, for example) these values decrease by a factor of roughly  $(500/200)^4 = 39$ . For comparison, we also show in Figure 4 the frequency distribution for  $\lambda = 126$  nm in the year 2080, again for  $69 \pm 3^\circ\text{N}$ . As can be seen, the distribution extends to much larger attenuations compared to  $\lambda = 200$  nm which demonstrates again that extinctions and attenuations increase rapidly with decreasing wavelengths (see Figure 2).

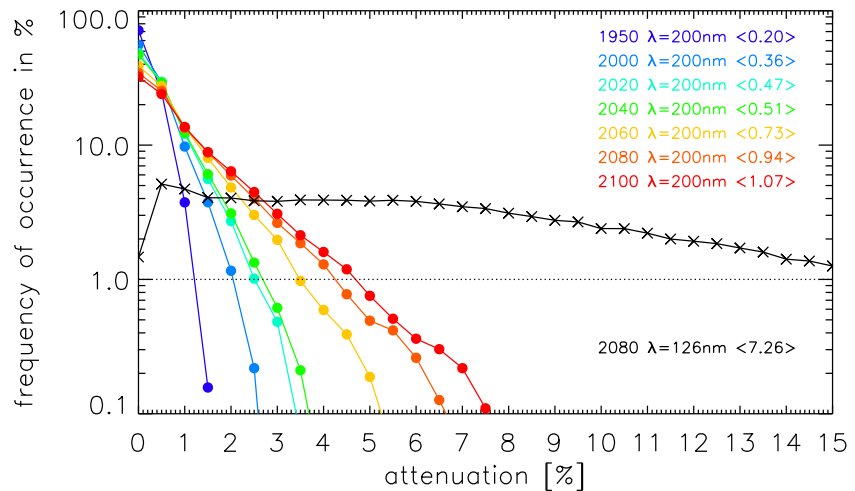


**Figure 4.** The relative occurrence frequency of attenuations at  $69 \pm 3^\circ\text{N}$  from various years (see inset) for a wavelength of  $\lambda = 200 \text{ nm}$  (dots). The values for  $\lambda = 126 \text{ nm}$  (black, crosses, 2080 only) demonstrate that attenuations are increasing rapidly for decreasing wavelengths. The inset also lists the mean attenuations ( $\langle \dots \rangle$ ) in %.

In Figure 5 the long-term evolution of mean optical thickness and attenuation is shown for  $\lambda = 126 \text{ nm}$  at  $69 \pm 3^\circ\text{N}$ . The values are determined as follows: for a given year, extinction coefficients  $\tau_{i,j,k}$  are available at all  $i_{\text{max}} = 124$  time-steps,  $j_{\text{max}} = 6$  latitudes, and  $k_{\text{max}} = 120$  longitudes. First, the mean extinction coefficient  $\bar{\tau}_i$  at each time-step  $i$  is determined, averaging over all latitudes/longitudes but only where NLC are present. Then the mean over all time-steps  $\bar{\tau}$  in a given year is calculated, as well as the standard deviation of the mean and the maximum and minimum values. Thus, the vertical bars and the dashed lines in Figure 5 indicate the temporal variability of the attenuations. Furthermore, the maximum of all values in a given year  $\tau_{i,j,k}$  is shown, called “grand maximum”. As can be seen from Figure 5, mean absorptions at  $\lambda = 126 \text{ nm}$  increase from  $\sim 3\%$  to  $\sim 7\%$  from 1950 to 2100, respectively. The mean variability is on the order of a factor of two. Locally, the absorption can increase up to 30% in the year 2100. In the visible (532 nm, not shown) mean attenuations increase from 0.0030% (1950) to 0.020% (2100), that is, by a factor of  $\sim 7$ . Locally, maximum values can reach up to 0.35% in 2100.

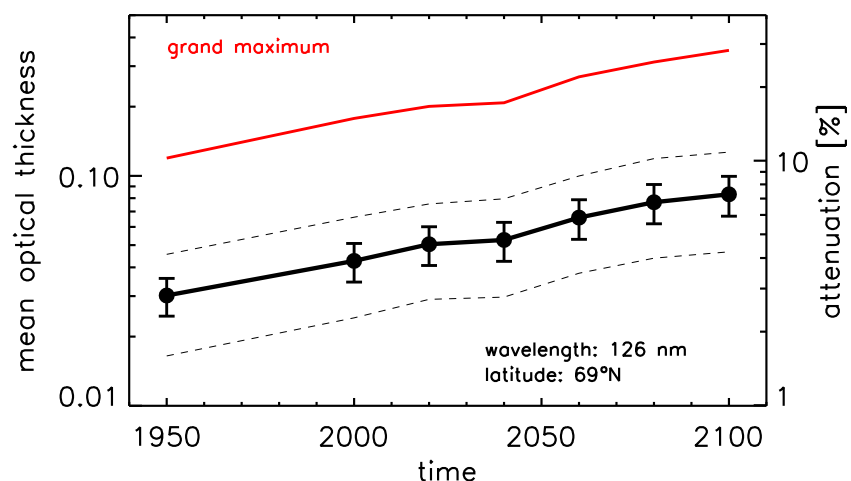


**Figure 5.** For each selected year the mean extinction coefficients (left axis) and attenuations (right axis) are shown at  $69 \pm 3^\circ\text{N}$ . First, we average the extinction coefficients from all columns (only where NLC are present) at a given time-step. Then we take the extinction coefficients from all time-steps and determine the mean (dots), standard deviation (bars), and the maximum and minimum values (dashed lines). Furthermore, the maximum extinction coefficient from all columns (before averaging) is shown (red line, “grand maximum”). See text for more details.

#### 4. Discussion and Conclusion

We have also studied future extinctions etc., at other latitudes and find similar results (compared to  $69 \pm 3^\circ\text{N}$ ) at  $78 \pm 3^\circ\text{N}$ , but significantly smaller values at  $58 \pm 3^\circ\text{N}$  (not shown). The total amount of ice mass bound in NLC also increases with time, namely from 677 tons in 1950 to 1259 and 1871 tons in 2050 and 2100, respectively, where the largest fraction (typically 80%–90%) stems from north of  $60^\circ\text{N}$  (see Figure 1). The increase of ice mass strongly correlates with the concentration of methane (correlation coefficient: 0.98), where each additional ppbv of methane increases the ice mass by approximately 0.5 tons. The ice water content, that is, the ice mass in a given column, increases correspondingly.

Note that the relative increase of extinction and attenuation with time (see Figure 5 for  $\lambda = 126$  nm) is significantly stronger at larger wavelengths ( $\lambda = 532$  nm, for example) where the extinction is roughly proportional to  $r^6$ , whereas the dependence on radius is weaker at 126 nm because the Rayleigh scattering condition  $\lambda/2\pi r \gg 1$  is no longer valid. We have checked the results for consistency. For example: the variation of ice mass ( $\sim r^3$ ) and attenuation ( $\sim r^6$ ) are consistent, since (for the years 2100 and 1950) we have  $(1871 \text{ tons}/677 \text{ tons})^{1/3} \sim 1.40$  and (for  $\lambda = 532$  nm) we get  $(0.02056\%/0.00301\%)^{1/6} \sim 1.38$ , which are surprisingly similar when we consider that we have ignored various factors complicating such a comparison.

In order to judge the importance of the solar radiation absorption by NLC we compare with the variability due to the solar cycle, all of which vary substantially with wavelengths. For example, in the visible the solar cycle variation is roughly 0.1% (see, for example, Figure 3 in Gray et al. (2010)). We have repeated the trend calculations shown in Figure 5 for  $\lambda = 532$  nm and find for the year 2100 mean absorptions of 0.02% and (grand) maximum absorptions of  $\sim 0.35\%$ . The latter implies that in certain areas the maximum absorption by NLC in the visible as expected for 2100 is significantly larger compared to the variation throughout a solar cycle. In the UV ( $\lambda = 126$  nm) the variations are several tens percent, both during a solar cycle and for the maximum absorption by NLC (see Figure 5).

The absorption of solar radiation by NLC will presumably affect photochemical processes at lower heights, in particular those related to odd oxygen. We realize that most of the involved reaction mechanisms are non-linear which means that a sophisticated analysis is required to make quantitative predictions. The same applies for positive feedback mechanisms, which are currently ignored: the absorption of solar UV radiation leads to less dissociation and higher concentrations of water vapor, which leads to more and larger ice particles, which in turn leads to more absorption of solar radiation. In summary, it is likely that the absorption of solar radiation by NLC will affect the photochemistry in the mesosphere and stratosphere. To make more quantitative statements requires sophisticated modeling which is beyond the scope of this paper.

Last but not least, based on our previous studies on the impact of methane on the morphology of NLC, we can expect that for ground based visible observers at middle latitudes, the conditions to observe NLC become more favorable in the future, that is, the occurrence frequency and the brightness of NLC will increase substantially.

#### Data Availability Statement

Data is available at Lübken et al. (2024).

#### References

- Berger, U. (2008). Modeling of middle atmosphere dynamics with LIMA. *Journal of Atmospheric and Solar-Terrestrial Physics*, 70(8–9), 1170–1200. <https://doi.org/10.1016/j.jastp.2008.02.004>
- Berger, U., & Lübken, F.-J. (2011). Mesospheric temperature trends at mid-latitudes in summer. *Geophysical Research Letters*, 38(22). <https://doi.org/10.1029/2011GL049528>
- Berger, U., & Lübken, F.-J. (2015). Trends in mesospheric ice layers in the Northern Hemisphere during 1961–2013. *Journal of Geophysical Research*, 120(11), 277–298. <https://doi.org/10.1002/2015JD023355>
- Berger, U., & von Zahn, U. (2002). Icy particles in the summer mesopause region: Three-dimensional modeling of their environment and two-dimensional modeling of their transport. *Journal of Geophysical Research*, 107(A11). <https://doi.org/10.1029/2001JA000316>
- Fiedler, J., Baumgarten, G., Berger, U., & Lübken, F.-J. (2017). Long-term variations of noctilucent clouds at ALOMAR. *Journal of Atmospheric and Solar-Terrestrial Physics*, 162, 79–89. <https://doi.org/10.1016/j.jastp.2016.08.006>
- Gadsden, M., & Schröder, W. (1989). *Noctilucent clouds*. Springer-Verlag.
- Gray, L. J., Beer, J., Geller, M., Haigh, J. D., Lockwood, M., Matthes, K., et al. (2010). Solar influences on climate. *Review of Geophysics*, 48(4). <https://doi.org/10.1029/2009RG000282>
- Hervig, M. E., Berger, U., & Siskind, D. E. (2016). Decadal variability in PMCs and implications for changing temperature and water vapor in the upper mesosphere. *Journal of Geophysical Research*, 121(5), 2383–2392. <https://doi.org/10.1002/2015JD024439>

#### Acknowledgments

We thank Jens Fieder for providing an update of the lidar data from ALOMAR and Robin Wing for assistance in formulating the abstract. The Mie calculations were performed using information from <http://atol.ucsd.edu/scatlib/index.htm>. This paper was supported by the TIMA project (Grant 01LG1902A) of the BMBF research initiative ROMIC. Open Access funding enabled and organized by Projekt DEAL.

- Hervig, M. E., Siskind, D. E., Bailey, S. M., & Russell III, J. M. (2015). The influence of PMCs on water vapor and drivers behind PMC variability from SOFIE observations. *Journal of Atmospheric and Solar-Terrestrial Physics*, *132*, 124–134. <https://doi.org/10.1016/j.jastp.2015.07.010>
- Kokhanovsky, A. (2005). Microphysical and optical properties of noctilucent clouds. *Earth-Science Reviews*, *71*(1–2), 127–146. <https://doi.org/10.1016/j.earscirev.2005.02.005>
- Latteck, R., Renkowitz, T., & Chau, J. L. (2021). Two decades of long-term observations of polar mesospheric echoes at 69°N. *Journal of Atmospheric and Solar-Terrestrial Physics*, *216*, 105576. <https://doi.org/10.1016/j.jastp.2021.105576>
- Lübken, F.-J., Baumgarten, G., & Berger, U. (2021). Long term trends of mesospheric ice layers: A model study. *Journal of Atmospheric and Solar-Terrestrial Physics*, *214*, 105378. <https://doi.org/10.1016/j.jastp.2020.105378>
- Lübken, F.-J., Baumgarten, G., Vellalassery, A., & Grygalashvyly, M. (2024). Data in ASCII format as shown in figure 1 to 5 in Lübken et al. [Dataset]. *Geophysical Research Letters* <https://doi.org/10.22000/1811>
- Lübken, F.-J., Berger, U., & Baumgarten, G. (2018). On the anthropogenic impact on long-term evolution of noctilucent clouds. *Geophysical Research Letters*, *45*(13), 6681–6689. <https://doi.org/10.1029/2018GL077719>
- Pertsev, N., Dalin, P., Perminov, V., Romejko, V., Dubietis, A., Balčiunas, R., et al. (2014). Noctilucent clouds observed from the ground: Sensitivity to mesospheric parameters and long-term time series. *Earth plan. Space*, *66*(98), 98. <https://doi.org/10.1186/1880-5981-66-98>
- Riahi, K., Rao, S., Krey, V., Cho, C., Chirkov, V., Fischer, G., et al. (2011). Rcp 8.5 - A scenario of comparatively high greenhouse gas emissions. *Climatic Change*, *109*(33), 33–57. <https://doi.org/10.1007/s10584-011-0149-y>
- Russell III, J. M., Rong, P., Hervig, M. E., Siskind, D. E., Stevens, M. H., Bailey, S. M., & Gumbel, J. (2015). Analysis of northern midlatitude noctilucent cloud occurrences using satellite data and modeling. *Journal of Geophysical Research*, *119*(6), 3238–3250. <https://doi.org/10.1002/2013JD021017>
- Schmidt, F., Baumgarten, G., Berger, U., Fiedler, J., & Lübken, F.-J. (2018). Local time dependence of polar mesospheric clouds: A model study. *Atmospheric Chemistry and Physics*, *18*(12), 8893–8908. <https://doi.org/10.5194/acp-18-8893-2018>
- Thomas, G. E. (2003). Are noctilucent clouds harbingers of global change in the middle atmosphere? *Advances in Space Research*, *32*(9), 1737–1746. [https://doi.org/10.1016/s0273-1177\(03\)90470-4](https://doi.org/10.1016/s0273-1177(03)90470-4)
- Vellalassery, A., Baumgarten, G., Grygalashvyly, M., & Lübken, F.-J. (2023). Greenhouse gas effects on the solar cycle response of water vapour and noctilucent clouds. *Annals of Geophysics*, *41*(2), 289–300. <https://doi.org/10.5194/angeo-41-289-2023>
- Warren, S. G., & Brandt, R. E. (2008). Optical constants of ice from the ultraviolet to the microwave: A revised compilation. *Journal of Geophysical Research*, *113*(D14), 2007JD009744. <https://doi.org/10.1029/2007JD009744>
- Yu, W., Yue, J., Garcia, R., Mlynchak, M., & Russell, J., III. (2023). WACCM6 projections of polar mesospheric cloud abundance over the 21st century. *Journal of Geophysical Research*, *128*(15). <https://doi.org/10.1029/2023JD038985>

# Contribution to the Manuscripts

Individual contributions of the PhD candidate to the manuscripts submitted in this cumulative thesis are listed below.

In Vellalassery et al. (2023), The candidate contributed to the concept formulation and performed most of the data analyses, including the simulation of the MIMAS model. The candidate played an important role in discussing the results with the co-authors and concluding. In addition, the candidate developed all figures and drafted the manuscript incorporating suggestions and comments from the co-authors. The candidate also submitted the manuscript and addressed all reviewer comments during the review process.

In Vellalassery et al. (2024), the candidate played a key role in formulating the concept, performed MIMAS model simulations and data analyses and contributed extensively to discussing results and drawing conclusions. The candidate also developed all figures, drafted the manuscript, submitted it, and responded to the reviewers' comments throughout the review process by discussing them with the co-authors.

In Lübken et al. (2024), the candidate carried out the MIMAS model simulations and managed the post-processing of the model data. The candidate also participated in discussing the results and provided feedback on the manuscript during its initial drafting and the review process.



# Curriculum Vitæ

## Personal Information

**Name** Vellalassery, Ashique  
**Date of Birth** 05.01.1996  
**Place of Birth** Kerala, India

## Scientific career

**Since 11/2020** PhD student,  
 Leibniz Institute of Atmospheric Physics at the University of Rostock, Germany  
 Supervisors: Prof. Dr. Franz Josef Lübken, Prof. Dr. Gerd Baumgarten, Dr. Mykhaylo Grygalashvyly

**07/2019–10/2020** Research Assistant,  
 Greenhouse gas Modelling and Applications (GMA) group,  
 Indian Institute of Science Education and Research, Bhopal, India  
 Research work: Advancing the use of space-borne observations to estimate the spatiotemporal distribution of greenhouse gas fluxes over India  
 Supervisor: Dr. Dhanyalekshmi Pillai

**08/2014–05/2019** Bachelor of Science and Master of Science (BSMS), Earth and Environmental Sciences, Indian Institute of Science Education and Research, Bhopal, India  
 Thesis title: On inferring hotspot biomass burning emissions over India using Greenhouse gas satellite observations  
 Supervisor: Dr. Dhanyalekshmi Pillai

## Publications

- Franz Josef Lübken et al. (2024). "Absorption of Solar Radiation by Noctilucent Clouds in a Changing Climate". In: *Geophysical Research Letters* 51.8. ISSN: 0094-8276. DOI: 10.1029/2023GL107334
- Ashique Vellalassery et al. (2024). "Long-Term Evolution in Noctilucent Clouds' Response to the Solar Cycle: A Model-Based Study". In: *Atmosphere* 15.1. ISSN: 20734433. DOI: 10.3390/atmos15010088
- Ashique Vellalassery et al. (2023). "Greenhouse gas effects on the solar cycle response of water vapour and noctilucent clouds". In: *Annales Geophysicae* 41.2, pp. 289–300. ISSN: 14320576. DOI: 10.5194/angeo-41-289-2023
- Ashique Vellalassery et al. (2021). "Using TROPOspheric Monitoring Instrument (TROPOMI) measurements and Weather Research and Forecasting

(WRF) CO modelling to understand the contribution of meteorology and emissions to an extreme air pollution event in India". In: *Atmospheric Chemistry and Physics* 21.7, pp. 5393–5414. ISSN: 1680-7324. DOI: 10.5194/acp-21-5393-2021

## *Acknowledgements*

This work would not have been possible without the support and guidance of many people, to whom I am deeply grateful. First, I would like to thank my thesis supervisors, Prof. Dr. Franz Josef Lübken, Prof. Dr. Gerd Baumgarten, and Dr. Mykhaylo Grygalashvyly. Their mentorship, encouragement, and constant support were crucial during my PhD candidature.

When I started my PhD in the middle of the coronavirus pandemic and at the beginning of a cold winter, I had many difficulties adapting to a new environment that was very different from my home country. Dr. Gerd Baumgarten's continuous support and flexibility were crucial to my journey. Whether for scientific advice or personal needs, Gerd was always available to help. His willingness to accommodate my personal needs, including the ability to work from different locations, was essential in making me feel comfortable and able to focus. He is the coolest, most supportive and helpful supervisor one can get. I am especially grateful to Dr. Mykhaylo Grygalashvyly, whose patient mentorship was invaluable as I moved into new areas of research. Misha's commitment to teaching me the basics of the model I worked with provided a strong foundation for my research. His daily guidance and willingness to support me through any challenges were crucial throughout my research, and he was always there whenever I reached out for help. Prof. Dr. Franz-Josef Lübken's insights and advice, especially during the writing process of the manuscript, were indispensable. His expertise and thoughtful feedback helped to shape my research into a coherent and effective work. He was consistently available and willing to engage in discussions whenever I needed his support. I could not have asked for more supportive supervisors.

I am grateful to all my colleagues and friends at the IAP for their support and positive attitude, which helped me to get through challenging times and enjoy happy moments. I thank the IT department for their dedicated maintenance and support throughout my numerous model simulations and other computational tasks. I would also like to thank the administrative staff of the IAP for their invaluable help in dealing with formalities related to my contract, visa, conferences and various other matters.

I am deeply grateful to all my friends, both here with me and in my home country, for their valuable support, motivation, and the wonderful moments we have shared at gatherings and while travelling. Your encouragement has been the driving force behind my journey, and I am very grateful to you. I am not naming names because I am afraid I might miss someone, but I want you to know that each of you has played an invaluable role in my success.

My gratitude to my parents, Umma and Uppa, and my little brother Aadhi, for their boundless love and support throughout this journey is beyond words. My heartfelt gratitude to all my family members for their constant prayers and belief in my dreams. Their support has been my greatest strength.

Finally, I want to thank Febii, my beautiful girlfriend. We have been together for the past 8 years, and during all this time, she has been my courage, support, motivation, and everything. Thank you for standing by me and bringing happiness into my life during both the hardest challenges and the happiest moments. My gratitude for you is beyond words. Thank you for everything.



## Declaration of Authorship

I, Ashique VELLALASSERY, herewith, declare the following:

- The opportunity for this PhD project was not communicated to me commercially. In particular, I have not engaged any organisation that, for money, seeks supervisors for the drawing up of dissertations or that performs entirely or partially on my behalf the duties incumbent upon me regarding the examinations.
- I hereby declare under oath that I have completed the work submitted here independently and have composed it without outside assistance. Furthermore, I have not used anything other than the resources and sources stated and where I have taken sections from these works in terms of content or text, I have identified this appropriately.

Signed: Ashique Vellalassery

---

Date: 01 July 2024

---